

## Net deployment and contact dynamics of capturing space debris objects

Shan, Minghe

**DOI**

[10.4233/uuid:803af7c5-4a97-48e9-870b-8e2f6fd325d8](https://doi.org/10.4233/uuid:803af7c5-4a97-48e9-870b-8e2f6fd325d8)

**Publication date**

2018

**Document Version**

Final published version

**Citation (APA)**

Shan, M. (2018). *Net deployment and contact dynamics of capturing space debris objects*. [Dissertation (TU Delft), Delft University of Technology]. <https://doi.org/10.4233/uuid:803af7c5-4a97-48e9-870b-8e2f6fd325d8>

**Important note**

To cite this publication, please use the final published version (if applicable).  
Please check the document version above.

**Copyright**

Other than for strictly personal use, it is not permitted to download, forward or distribute the text or part of it, without the consent of the author(s) and/or copyright holder(s), unless the work is under an open content license such as Creative Commons.

**Takedown policy**

Please contact us and provide details if you believe this document breaches copyrights.  
We will remove access to the work immediately and investigate your claim.

**NET DEPLOYMENT AND CONTACT DYNAMICS OF  
CAPTURING SPACE DEBRIS OBJECTS**



# **NET DEPLOYMENT AND CONTACT DYNAMICS OF CAPTURING SPACE DEBRIS OBJECTS**

## **Dissertation**

for the purpose of obtaining the degree of doctor  
at Delft University of Technology  
by the authority of the Rector Magnificus prof.dr.ir. T.H.J.J. van der Hagen  
chair of the Board for Doctorates  
to be defended publicly on  
Friday 22 June 2018 at 15:00 o'clock

by

**Minghe SHAN**

M.Sc. of Aerospace Manufacturing Engineering,  
Harbin Institute of Technology, Harbin, China,  
born in Meihekou, Jilin Province, China.

This dissertation has been approved by the promotors:

promotor: Prof. Dr. E. K. A. Gill

copromotor: Dr. J. Guo

Composition of the doctoral committee:

Rector Magnificus,	chairperson
Prof. Dr. E. K. A. Gill,	Delft University of Technology, promotor
Dr. J. Guo,	Delft University of Technology, copromotor

*Independent members:*

Prof. Dr. A. K. Misra	Mcgill University, Canada
Prof. Dr. Z. H. Zhu	York University, Canada
Prof. Dr. M. Lavagna	Politecnico di Milano, Italy
Prof. Dr. P. P. Jonker	Delft University of Technology
Prof. Dr. P. Visser	Delft University of Technology, reserve member

This research was funded by the China Scholarship Council (CSC), and also supported by the Delft University of Technology.



*Keywords:* space debris, net capturing method, deployment dynamics, contact dynamics, parabolic flight experiment, tumbling targets capturing, net closing mechanism.

*Printed by:* ProefschriftMaken, The Netherlands

*Cover by:* <http://www.oopic.com/>

Copyright © 2018 by Minghe Shan

ISBN 978-94-6295-985-9

An electronic version of this dissertation is available at  
<http://repository.tudelft.nl/>.

To my parents



# CONTENTS

<b>Summary</b>	<b>xi</b>
<b>Samenvatting</b>	<b>xv</b>
<b>1 Introduction</b>	<b>1</b>
1.1 Background and Motivations . . . . .	2
1.2 The State of The Art . . . . .	6
1.2.1 Active Debris Removal . . . . .	6
1.2.2 Dynamic Modeling of Net Capturing . . . . .	7
1.2.3 Capturing of Tumbling Debris . . . . .	9
1.3 Research Questions . . . . .	10
1.4 Methodology . . . . .	11
1.4.1 Dynamics Modeling . . . . .	12
1.4.2 Numerical Simulation . . . . .	12
1.4.3 Cross-verification and Validation . . . . .	12
1.5 Thesis Outline . . . . .	13
<b>2 Space Debris Capturing and Removal Methods</b>	<b>15</b>
2.1 Introduction . . . . .	16
2.2 Classification of Space Debris . . . . .	16
2.3 Capturing Methods . . . . .	17
2.3.1 Stiff-Connection Capturing . . . . .	18
2.3.2 Flexible-Connection Capturing . . . . .	21
2.4 Removal Methods . . . . .	24
2.4.1 Drag Augmentation System . . . . .	24
2.4.2 Electro-Dynamic Tether . . . . .	26
2.4.3 Contact-Based Removal Methods . . . . .	26
2.4.4 Contactless Removal Methods . . . . .	28
2.4.5 Tailored ADR Methods . . . . .	29
2.5 Summary . . . . .	31
<b>3 Deployment Dynamics of a Net</b>	<b>33</b>
3.1 Introduction . . . . .	34
3.2 Characteristics of a Net . . . . .	35
3.2.1 Physical Properties of a Net . . . . .	35
3.2.2 Folding Scheme . . . . .	36
3.2.3 Output and Input Parameters . . . . .	36
3.3 Dynamic Models of a Net . . . . .	39
3.3.1 Mass-Spring Model . . . . .	39
3.3.2 ANCF Model . . . . .	41

3.4	Sensitivity Analysis . . . . .	44
3.4.1	Simulation . . . . .	44
3.4.2	Investigation on Net Characteristics . . . . .	44
3.4.3	Dependency Analysis . . . . .	45
3.5	Verification and Validation . . . . .	47
3.5.1	Cross-Verification . . . . .	47
3.5.2	Validation by Parabolic Flight Experiment . . . . .	52
3.6	Summary . . . . .	61
<b>4</b>	<b>Contact Dynamics of Nets and Targets</b>	<b>63</b>
4.1	Introduction . . . . .	64
4.2	Penalty-Based Method . . . . .	65
4.2.1	Normal Contact Force . . . . .	66
4.2.2	Friction . . . . .	68
4.3	Impulse-Based Method . . . . .	69
4.3.1	Single Contact on One Target . . . . .	70
4.3.2	Multiple Contacts on One Target . . . . .	72
4.4	Modeling of Flexibility . . . . .	74
4.5	Verification and Validation . . . . .	78
4.5.1	Cross-verification . . . . .	78
4.5.2	Validation by Parabolic Flight Experiment . . . . .	83
4.6	Summary . . . . .	89
<b>5</b>	<b>Capturing of Tumbling Targets</b>	<b>91</b>
5.1	Introduction . . . . .	92
5.2	Capturing of Free-Floating Targets . . . . .	93
5.2.1	Free-Floating Cubesat . . . . .	94
5.2.2	Free-Floating Rocket Upper Stage . . . . .	95
5.2.3	Free-Floating Envisat . . . . .	96
5.3	Capturing of Tumbling Targets . . . . .	97
5.3.1	Tumbling Cubesat . . . . .	97
5.3.2	Tumbling Rocket Upper Stage . . . . .	99
5.3.3	Tumbling Envisat . . . . .	100
5.4	Net Closing System . . . . .	101
5.4.1	Introduction of the Net Closing Mechanism . . . . .	101
5.4.2	Targets Capturing with Closing Mechanism . . . . .	104
5.5	Summary . . . . .	106
<b>6</b>	<b>Conclusion</b>	<b>109</b>
6.1	Summary . . . . .	110
6.2	Conclusions and Innovations . . . . .	111
6.3	Recommendations . . . . .	114
	<b>References</b>	<b>115</b>
	<b>Acknowledgements</b>	<b>127</b>
	<b>Curriculum Vitæ</b>	<b>129</b>

---

**List of Publications**

**131**



# SUMMARY

Space debris poses a big threat to operational satellites which form a crucial infrastructure for society. According to the main source of information on space debris, the U.S. Space Surveillance Network (SSN), more than 17 500 objects larger than 10 cm have been catalogued as of February 2017. Among the total number of objects in orbit, only 1875 spacecraft are active, i.e., around 10% of the objects are operating in an environment where 90% of the other objects are space debris. Even more serious, space debris is a threat to astronauts. In March 2009, a five inch space debris object passed particularly close to the International Space Station (ISS). Fortunately, the alarm was cleared 10 minutes later. Moreover, the collision of the satellites Cosmos 2251 and Iridium 33 in 2009 highlighted the threat by space debris, since it signaled a trend that the future space environment will be dominated by fragmentation debris generated via similar collisions, instead of explosions of rocket upper stages, which had formed the majority of space debris objects in the past. To mitigate the risk of collision and stabilize the space environment, active debris removal (ADR) is of great relevance. According to an analysis by NASA, five space debris objects need to be removed each year to stabilize the space environment starting from the year 2020.

The objective of this research is to investigate the net capturing method for active space debris removal. To remove a debris object from its orbit, many capturing and removal methods have been proposed, such as using a robotic arm, a tethered space robot, or a harpoon system. Among the existing ADR methods, net capturing is regarded as one of the most promising capturing methods due to its multiple advantages. For example, it allows a large distance between a chaser satellite and a target, so that close rendezvous and docking are not mandatory. It is furthermore compatible to different sizes, shapes and orbits of space debris. Additionally, it is flexible, lightweight and cost efficient. Even though some research on net capturing has been performed, the dynamics of net deployment and debris capturing and the feasibility and reliability of capturing a tumbling target using a net are not fully understood. Based on the relevance of this problem and a review of the state-of-the-art of the scientific literature, the following research questions were formulated. These research questions are answered in this thesis.

**RQ1. Which levels of non-cooperativeness of space debris exist? Which are their associated capturing and/or removal methods and what is the role the net capturing method plays among all those methods?**

**RQ2. What are the dynamic characteristics of the net capturing method?**

**RQ3. How to reliably capture a tumbling and non-cooperative debris object using the net capturing method?**

To characterize the net capturing method among existing ADR methods and to address the strengths and weaknesses of the net capturing method, matrices with the advantages and drawbacks of the most relevant capturing and removal methods are developed. Space debris objects were divided into three main categories based on their prop-

erties, namely, non-operational satellites, rocket upper stages and fragments from collision or explosion. A tailored associated capturing and removal method for each category of space debris objects is provided to facilitate decision-making through these ADR methods. A comparison of the most relevant ADR methods concludes that net capturing is considered as a promising method among others due to its multiple advantages. It is also found that capturing a tumbling space debris object with unknown physical properties is still facing many technological challenges. Therefore, capturing of tumbling targets using a net needs to be further investigated. The net capture mechanism consists of four flying weights in each corner of a net. The flying weights, named "bullets", are shot by a spring system, named "net gun". These four bullets expand the large net thus wrapping the target that will be transported by the tether connecting the chaser and the net.

This thesis starts with the analysis of the deployment dynamics of a net. The deployment dynamic characteristics of a net folded in a pattern proposed in this research called "inwards-folding scheme" are investigated based on the mass-spring model and the absolute nodal coordinates formulation (ANCF) model. Deployment dynamics of a net based on the ANCF model are, for the first time, modeled, analysed and discussed in-depth. Besides, four critical parameters describing the deployment dynamic characteristics of the net, namely, the maximum area, the deployment time, the travelling distance and the effective period are defined. A sensitivity analysis of the initial input parameters, such as the initial bullet velocity, the shooting angle and the bullet mass with respect to the four critical parameters are performed. Simulations based on the ANCF model are performed and compared with the conventional mass-spring model. The results from both methods show a good agreement on changes of the four critical parameters. Furthermore, the ANCF model is more capable of describing the flexibility of the net with fewer nodes than the conventional mass-spring model. However, it is more computationally expensive.

To investigate the contact dynamics between a net and a target, two contact modeling methods: the penalty-based and the impulse-based method are compared and analyzed. The theoretical solutions of the single contact and the multiple contacts dynamics based on the impulse-based method are derived. To our knowledge, the impulse-based method is, for the first time, being used in a net capturing scenario. Numerical simulations of targets with basic shapes, i.e., a cube, a ball and a cylinder, are performed to cross-verify the two contact models. It is concluded that the impulse-based method is superior to the penalty-based method with respect to the penetration avoidance and computational robustness. Moreover, the modeling of the flexibility of a net is addressed and discussed for the first time. To investigate the influence of the flexibility modeling on the net dynamics, simulations of capturing of a ball- and a cube-shaped target using the mass-spring model and the ANCF model are performed and compared, respectively. However, it is found that the modeling of the flexibility of a net for capturing a space debris object has little influence on net deployment and contact dynamics.

The dynamics of the net deployment and contact with the target have to be experimentally validated. A parabolic flight experiment performed under ESA contract allows to compare the experimental results with the simulations of the net deployment and the capturing phase. In the net deployment phase, simulation results based on both net

modelling methods, the mass-spring model and the ANCF model, are compared with the experimental results. From the analysis of the absolute and the average relative residuals between the simulations and results of the parabolic flight experiment, it is concluded that both models are able to describe the motion of the bullets and the net along the traveling direction with an average relative residual error up to 15%. In the net capturing phase, both contact models, the penalty-based method and the impulse-based method, are validated by the parabolic flight experiment of the capturing of an Envisat mockup. The comparison shows that the average difference between the two models is limited to 7% when comparing with the travelling distance of the net.

With the validated net deployment and contact dynamic models, net capturing of free-floating targets and tumbling targets is investigated for the first time. The net's compatibility to handle different sizes and shapes of targets is demonstrated by simulation results of the capturing of three types of targets varying in size and shape, namely, a 3-unit Cubesat without appendages, the simplified representation of the second upper stage of the Zenit-2 rocket and the Envisat satellite. Simulation results show that for free-floating targets the net is able to capture and surround the targets without pushing them away. For tumbling targets, the net without a closing mechanism is able to capture the targets when their tumbling rates are within a certain range: 0-1.5 rad/s for the Cubesat and 0-0.7 rad/s for the rocket upper stage. Simulations of the tumbling Envisat, which has appendages such as a solar panel and a radar antenna, indicates that the net capturing method is more robust to irregularly shaped targets than regularly shaped targets. Finally, a novel concept of a closing mechanism is designed and its effectiveness is demonstrated to ensure a successful capturing of the targets even with a higher tumbling rate.



# SAMENVATTING

Ruimtepuin vormt een grote bedreiging voor operationele satellieten die een cruciale infrastructuur voor de maatschappij vormen. Volgens de belangrijkste bron op het gebied van ruimtepuin, het Space Surveillance Network (SSN) uit de V.S., zijn er meer dan 17.500 objecten groter dan 10 cm gecatalogiseerd per februari 2017. Van alle objecten in een baan om de aarde, zijn slechts 1875 ruimtevaartuigen actief, 10% van de objecten functioneren dus in een omgeving waar 90% van de andere objecten ruimtepuin zijn. Nog serieuzer is het feit dat ruimtepuin een bedreiging vormt voor astronauten. In Maart 2009 vloog een ruimtepuinobject van 5 inch vlak langs het International Space Station (ISS). Gelukkig was het gevaar 10 minuten later geweken. De botsing tussen de satellieten Cosmos 2251 en Iridium 33 in 2009 benadrukte de dreiging die gevormd wordt door ruimtepuin, aangezien het de trend signaleerde dat de toekomstige ruimtevaartomgeving wordt gedomineerd door fragmentatiepuin. Dit puin is gegeneerd door vergelijkbare botsingen, in tegenstelling tot de explosie van de bovenste trap van raketten, wat voorheen het grootste deel van de ruimtepuinobjecten vormde. Actieve puin verwijdering is zeer relevant om het risico van een botsing te verminderen en de ruimtevaartomgeving te stabiliseren. Volgens een analyse door de NASA, moeten vanaf 2020 per jaar vijf ruimtepuinobjecten verwijderd worden om de ruimtevaartomgeving te stabiliseren.

Het doel van dit onderzoek is om een net-opvang-methode te onderzoeken voor de actieve verwijdering van ruimtepuin (AVR). Om een ruimtepuinobject uit zijn baan te halen zijn er veel verwijdermethodes voorgesteld, zoals het gebruik van een robotarm, een vastgebonden ruimterobot of een harpoensysteem. Onder de bestaande AVR-methodes wordt de net-opvang-methode als de meest kansrijke gezien, vanwege zijn meerder voordelen. De methode staat bijvoorbeeld een grotere afstand tussen de achtervolgingssatelliet en het doelwit, waardoor rendez-vous- en aankoppelmanoeuvres niet vereist zijn. De methode is ook compatibel met verscheidene maten, vormen en banen van ruimtepuin. Verder is de methode flexibel, lichtgewicht en kostenefficient. Hoewel er al enig onderzoek is uitgevoerd naar de net-opvang-methode, worden de dynamica van het ontvouwen van het net en het opvangen van puin alsmede de betrouwbaarheid en haalbaarheid wanneer er een tuimelend doelwit moet worden opgevangen nog niet volledig begrepen. Gebaseerd op de relevantie van dit probleem en een overzicht van de state-of-the-art van de wetenschappelijke literatuur zijn de volgende onderzoeksvragen geformuleerd:

**RQ1. Welke niveaus van niet-samenwerking van ruimtepuin bestaan? Wat zijn hun geassocieerde opvang en/of verwijder methodes en wat is de rol van de net-opvang-methode tussen al deze methodes?**

**RQ2. Wat zijn de dynamische karakteristieken van de net-opvang-methode?**

**RQ3. Hoe kan een tuimelend en niet samenwerkend ruimtepuin-object betrouwbaar opgevangen worden door middel van de net-opvang-methode?**

Om een de net-opvang-methode te karakteriseren tussen bestaande AVR-methoden en om de sterke en zwakke punten van de net-opvang-methode te adresseren worden de voor- en nadelen van de meest relevante opvang- en verwijdermethodes geïdentificeerd en gekarakteriseerd. Ruimtuinobjecten worden op basis van hun eigenschappen verdeeld in drie hoofdcategorieën, namelijk niet-operationele satellieten, de bovenste trappen van een raketten en fragmenten resulterend van een botsing of een ontplofing. Elke categorie wordt voorzien van een passende opvang- en verwijdermethode om de besluitvorming via deze AVR-methoden mogelijk te maken. Uit een vergelijking tussen de meest relevante AVR-methoden is te concluderen dat de net-opvang-methode een veelbelovende methode is, onder andere vanwege de vele voordelen. Het is ook gebleken dat het opvangen van een tuimelend ruimtepuinobject met onbekende fysieke eigenschappen nog steeds voor vele uitdagingen staat. Het opvangen van een tuimelend doelwit door middel van een net moet daarom verder onderzocht worden. De net-opvang-mechanisme bestaat uit vier vliegend gewichten in elke hoek van het net. De vliegende gewichten, genaamd “kogels”, worden afgeschoten door een veersysteem, genaamd “net-pistool”. De vier kogels ontvouwen het grote net en wikkelen het doelwit daarin. Het doelwit wordt vervolgens vervoerd door middel van de ketting die de volgsatelliet met het net verbindt.

Deze scriptie begint met de analyse van de uitvouwdynamica van het net. De karakteristieken van de uitvouwdynamica van een net dat is opgevouwen in een patroon dat wordt voorgesteld in dit onderzoek, genaamd het “Naar-binnen-gevouwen schema”, wordt onderzocht op basis van het massa-veermodel en het absolute nodale coördinaten formulering (ANCF) model. De uitvouwdynamica van het net gebaseerd op het ANCF-model wordt, voor het eerst, gemodelleerd, geanalyseerd en in detail besproken. Verder worden vier kritieke parameters die de karakteristieken van de uitvouwdynamica van het net beschrijven gedefinieerd, namelijk het maximale oppervlak, de uitvouwduur, de reisafstand en de effectieve periode. Een gevoeligheidsanalyse is uitgevoerd met betrekking tot de initiële input parameters, zoals de initiële kogelsnelheid, de schiethoek en de massa van de kogel. Simulaties gebaseerd op het ANCF-model zijn uitgevoerd en vergeleken met het conventionele massa-veermodel. De resultaten van beide methoden komen goed overeen met betrekking tot de veranderingen van de vier kritieke parameters. Het ANCF-model is daarnaast beter in staat om de flexibiliteit van het net te beschrijven met minder knopen dan het massa-veermodel. Het kost echter wel meer rekenkracht.

Om de contactdynamica tussen het net en het doelwit te onderzoeken, zijn twee contactmodelleringsmethoden geanalyseerd en vergeleken: de penalty-gebaseerde en de impuls-gebaseerde methode. De theoretische oplossingen van de enkelvoudige en meervoudige contactdynamica zijn afgeleid. Naar ons weten is de impuls-gebaseerde methode voor het eerst gebruikt bij een net-opvang-scenario. Numerieke simulaties van doelwitten met basale vormen, zoals een kubus, een bal en een cilinder, zijn uitgevoerd om de twee contactmodellen met elkaar te verifiëren. Geconcludeerd wordt dat de impuls-gebaseerde methode superieur is ten opzichte van de penalty-gebaseerde methode met betrekking tot het vermijden van penetraties en de rekenkundige robuustheid. Bovendien wordt de modelering van de flexibiliteit van het net voor de eerste keer geadresseerd en besproken. Om de invloed van de flexibiliteitsmodelering op de netdy-

namica te onderzoeken, zijn er simulaties uitgevoerd met zowel het massa-veermodel en het ANCF-model waarin een balvormig of kubusvormig doelwit wordt opgevangen. Het blijkt echter dat de modelering van de flexibiliteit van het net voor het opvangen van een ruimtetuinoobject weinig invloed heeft op het ontvouwen van het net en de contactdynamica.

De dynamica van het ontvouwen van het net en het contact met het doelwit moeten experimenteel gevalideerd worden. Een experiment uitgevoerd tijdens parabolische vlucht onder een ESA-contract maakt het mogelijk om experimentele resultaten met de simulaties van de net-ontvouwingsfase en de opvangfase. Simulatieresultaten gebaseerd op beide net-modelleringsmethoden, het massa-veermodel en het ANCF-model, voor de net-ontvouwingsfase zijn vergeleken met de experimentele resultaten. Uit de analyse van de absolute en gemiddelde relatieve residuen blijkt dat beide modellen de beweging van de kogels en het net in de reisrichting kunnen beschrijven met een gemiddelde relatieve restfout van maximaal 15%. Voor de net-vangfase zijn beide contactmodellen, de penalty-gebaseerde methode en de impuls gebaseerde methode, gevalideerd door het experiment tijdens de parabolische vlucht waarin een Envisat mock-up wordt opgevangen. De vergelijking laat zien dat het gemiddelde verschil tussen de twee modellen beperkt blijft tot 7% wanneer de reisafstanden van het net vergeleken worden.

Met de gevalideerde net-ontvouwings- en contactdynamicamodellen, is het vangen door middel van een net van vrij-vliegende doelwitten en tuimelende doelwitten voor de eerste keer onderzocht. De compatibiliteit van een net met verschillende maten en vormen van doelwitten is aangetoond door simulatieresultaten van het opvangen van doelwitten van drie types met verschillende maten en vormen, namelijk een 3-unit Cubesat zonder aanhangsels, een versimpelde representatie van de bovenste trap van een Zenit-2 raket en de Envisat satelliet. Bij vrij-vliegende doelwitten laten simulatieresultaten zien dat het net het doelwit kan opvangen en omringen zonder hen weg te duwen. Bij tuimelende doelwitten kan een net zonder sluitmechanisme deze opvangen als de tuimelsnelheden lager zijn dan 1.5 rad/s voor de Cubesat en 0.7 rad/s voor de bovenste trap van de raket. Simulaties van een tuimelende Envisat, die aanhangsels heeft zoals een zonnepaneel en een radarantenne, geven aan dat de net-opvang-methode robuuster is bij onregelmatig gevormde doelwitten dan bij regelmatig gevormde doelwitten. Ten slotte is een nieuw concept voor een sluitmechanisme ontworpen en is de effectiviteit hiervan aangetoond om te zorgen voor het succesvolle opvangen van doelwitten met hogere tuimelsnelheden.



# 1

## INTRODUCTION

## 1.1. BACKGROUND AND MOTIVATIONS

According to the Space Debris Office (SDO) of the European Space Agency (ESA), space debris is defined as "all non-functional, human-made objects, including fragments and elements thereof, in Earth orbit or re-entering into Earth's atmosphere" ([Website, 2017b](#)). The Earth orbit is in a serious predicament caused by millions pieces of space debris. As of January 2017, the number of space debris objects estimated to be in orbit according to statistical models by ESA is around 29 000 objects larger than 10 cm, 750 000 objects from 1 cm to 10 cm; and more than 166 million objects from 1 mm to 1 cm ([Website, 2017b](#)). According to the main source of information on space debris, the U.S. Space Surveillance Network (SSN), more than 17 500 objects larger than 10 cm have been catalogued by radar and other techniques as of February 2017 ([NASA Orbital Debris Program Office, 2017](#)). Figure 1.1 shows a summary of all objects in Earth orbit officially catalogued by the U.S. SSN. "Fragmentation debris" includes satellite breakup debris and anomalous event debris, while "mission-related debris" includes all objects dispensed, separated, or released as part of the planned mission. It is noticed that the total number of space debris is dramatically increasing in the 60 years of space activities and fragmentation debris dominates the environment ([NASA Orbital Debris Program Office, 2017](#)).

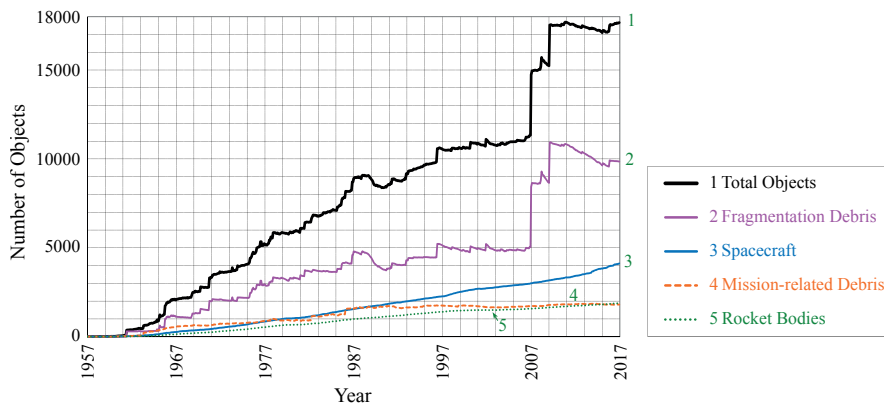


Figure 1.1: Number of objects in Earth orbit by object type ([NASA Orbital Debris Program Office, 2017](#))

Space debris can be produced in various ways, such as hyper-velocity impact with spacecraft, as well as high and low intensity explosion. Ten historical breakups account for nearly one-third catalogued orbital debris ([NASA Orbital Debris Program Office, 2016](#)). Table 1.1 summarises these top ten breakups as of January 4th, 2016. Six out of ten breakup events are due to the accidental explosion of rocket bodies. Fragmentation debris from two recent collisions, the Fengyun-1C anti-satellite test and the collision of Cosmos 2251 and Iridium 33 are responsible for the dramatically increasing number of space debris objects in the last ten years.

Specially, the collision of Cosmos 2251 and Iridium 33 in 2009 highlighted the threat by space debris, since it signaled a trend that the future space environment will be dominated by fragmentation debris generated via similar collisions, instead of explosions ([Liou, 2011](#)). This phenomenon reflects the Kessler Syndrome, stating that space debris

Table 1.1: Top ten breakups, as of January 2016 (NASA Orbital Debris Program Office, 2016)

Rank	Common Name	Year of Breakup	Altitude of Breakup	In Orbit	Assessed Cause of Breakup
1	Fengyun-1C	2007	850	2880	intentional collision
2	Cosmos 2251	2009	790	1141	accidental collision
3	Iridium 33	2009	790	364	accidental collision
4	Cosmos 1275	1981	980	289	battery explosion
5	Nimbus 4 Rocket Body	1970	1075	235	accidental explosion
6	CBERS 1 / SACI 1 Rocket Body	2000	740	210	accidental explosion
7	Cosmos 2227 Rocket Body	1992	830	199	accidental explosion
8	Nimbus 6 Rocket Body	1991	1090	199	accidental explosion
9	NOAA 3 Rocket Body	1973	1515	179	accidental explosion
10	NOAA 5 Rocket Body	1977	1510	174	accidental explosion

might be exponentially produced due to the continuous collision even if all launches into space would be stopped immediately (Kessler and Cour-Palais, 1978). However, the space environment will be in a worse situation since the space activities will continue and other unexpected collisions might continue to occur. Taking the recent two years for example, even though nearly 1000 debris objects have decayed and no serious collision has occurred, with the increasing space activities, more than 600 payloads have been launched and more than 1000 new debris objects have been generated. Table 1.2 shows the comparison of the debris numbers in the recent two years. As of Sep. 25th, 2017, only 1875 out of 4606 on-orbit payloads are active. Comparing it with the total number of objects on orbit, which is about 19 000, around 10% of the objects are operating in an environment where 90% of the other objects are space debris. Even more serious, space debris is a threat to astronauts. In March 2009, a five inch space debris object passed particularly close to the International Space Station (ISS). All the astronauts onboard were ordered to enter the escape capsule. Fortunately, the alarm was cleared 10 minutes later. However, in case the ISS were hit by the object, the astronauts would have had to head back to Earth (Website, 2017c).

Table 1.2: Orbital population as of January 8, 2015 and September 25, 2017 (Website, 2017a)

	2015			2017		
	Payloads	Debris	All	Payloads	Debris	All
<b>On Orbit</b>	3994	13131	17125	4606	14141	18747
<b>Decayed</b>	3049	20192	23241	3233	20961	24194
<b>All</b>	7043	33323	40366	7839	35102	42941

To mitigate the risk of collisions with those space debris objects, space debris removal activities are of great relevance and urgency. These activities include passive and active debris removal. According to (Sorge, 2015), "Active Debris Removal (ADR) involves changing the orbit of a debris object via the actions of another system". By this definition, Passive Debris Removal (PDR) can be defined as the activity of changing the orbit of a debris object without the involvement of another system. One example of the PDR is the Post-Mission Disposal (PMD) by the influence of the space environment, such as the aerodynamic drag and the solar radiation pressure, or by its own disposal system. The solar sail propulsion method was first validated by JAXA in 2010 (Tsuda et al.,

2011). Using the solar radiation force to remove space debris is a method for these non-operational satellites whose propulsion system fails or the propellant is not enough to re-enter, but whose control system for solar sails is still working. The orbit can be lowered by rotating the solar sails at appropriate moments to be expected to solar radiation, i.e., the satellite rotates its solar sails fully facing the sun when moving towards it, and making it parallel to the sun light when moving away from it. According to the analysis by Borja and Tun (2006), it will take no less than 5.8 years to de-orbit a geosynchronous satellite to a recommended altitude 235 km above the Earth surface proposed by the Inter-Agency Debris Coordination Committee. This method, however, depends highly on the solar sails driving capability. In order to overcome this drawback, Lücking et al. (2011) proposed a passive removal method: a combination of exploiting solar radiation pressure, Earth oblateness and aerodynamic drag. Since the solar sail propulsion is considered not applicable for altitudes below 750 km due to the atmospheric density, the solar radiation pressure is used to decrease the altitude from a significantly higher orbit and aerodynamic drag takes over when the debris is in a low altitude.

Besides the space environment based disposal strategies, all space companies and organizations are suggested to follow the 25-year safety standard which means a satellite should either lower its orbit and re-enter, or raise itself to a graveyard orbit within 25 years after the mission ends (NASA, 1995). However, with the PMD measures, including this 25-year rule, five space debris objects still need to be removed each year to stabilize the space environment at current level according to simulations using a NASA's orbital debris evolutionary model, LEGEND (an LEO-to-GEO environment debris model) by Liou (2011). Figure 1.2 shows the Low Earth Orbit (LEO) environment projection in the future 200 years. Three curves are the averages of 100 LEGEND Monte Carlo runs. "Reg Launches" means regular launches continue; "90% PMD" means that the PMD measures were applied with a 90% success rate; "ADR2020/02" means active debris removal starts from the year 2020 and the removal rate is two objects per year; "ADR2020/05" means active debris removal starts from the year 2020 and the removal rate is five objects per year (Liou, 2011).

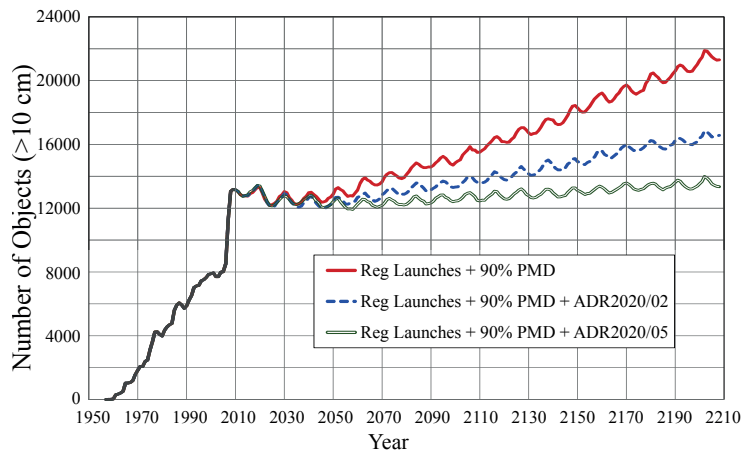


Figure 1.2: LEO environment prediction in 200 years (Liou, 2011)

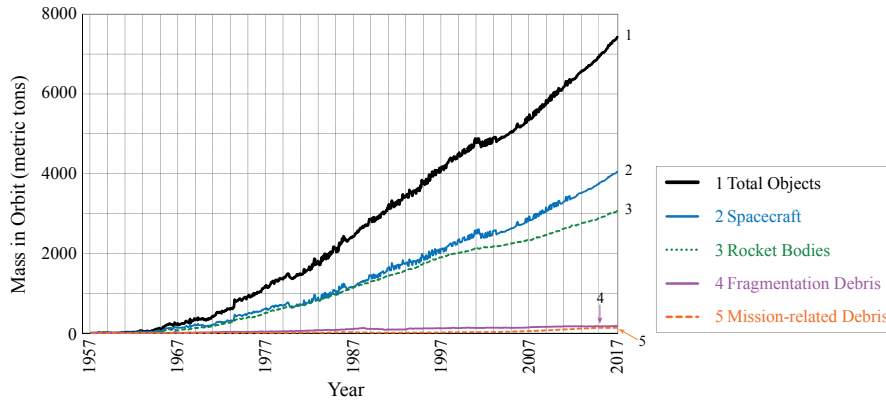


Figure 1.3: Mass of Objects in Earth Orbit by Object Type (NASA Orbital Debris Program Office, 2017)

It is noticed from Fig. 1.2 that five debris objects should be removed every year to stabilize the space environment. However, the debris objects selected to be removed should be the most threatening targets that might generate more space debris by collisions. Liou et al. have defined a selection criterion  $R_i$ , which is expressed as

$$R_i(t) = P_i(t) \times m_i, \quad (1.1)$$

where  $m_i$  is the mass of object  $i$ , and  $dP_i(t)$  is its collision probability at time  $t$  (Liou and Johnson, 2009). Based on this selection criterion, space debris objects in the most crowded orbits with greatest mass should be considered as potential removal targets. As early as 1975, NASA has already investigated the mass distribution of space debris and has performed several experiments on ground. Power or exponential function models are applied to estimate the mass distribution of the space debris (Bess, 1975). In reality, the total mass of all space debris objects in space is over 7000 metric tons until now and there is no sign of slowing down (NASA Orbital Debris Program Office, 2017) (see Fig. 1.3). Figure 1.3 indicates that spacecraft and rocket bodies dominate the mass distribution even though the fragment debris are far more than them in numbers.

Spatial and mass distributions of space debris objects have been discussed by Liou, from whose point of view, in LEO, the altitude close to 800 km is the most crowded orbit, and altitudes close to 600 km, 800 km and 1000 km are the massiest orbit since most of space debris objects with mass over 50 kg are located in those regions (Liou et al., 2010). The debris objects in an inclination region of 82.5-83.5° and altitudes between 900 to 1050 km are considered as regions of typical ADR targets (Liou, 2011). Liou also provided a top 500 priority list with the highest mass and collision possibility for removal, as shown in Fig. 1.4.

Bonnal et al. (2013) indicate that debris objects whose inclination ranging from 82.83-82.99°, and altitudes close to 1000 km should be given a priority following the criteria of debris object's re-entry criticality, nature and nationality. A list of 22 of the most critical ADR targets has been presented by Wiedemann et al. (2012), with Envisat being the most threatening target. Other threatening debris objects are rocket upper stages, e.g., SL-16 R/Bs (Zenith-2 upper stage, cylindrical with a diameter of 3.9 m, a length of 10.4 m, and

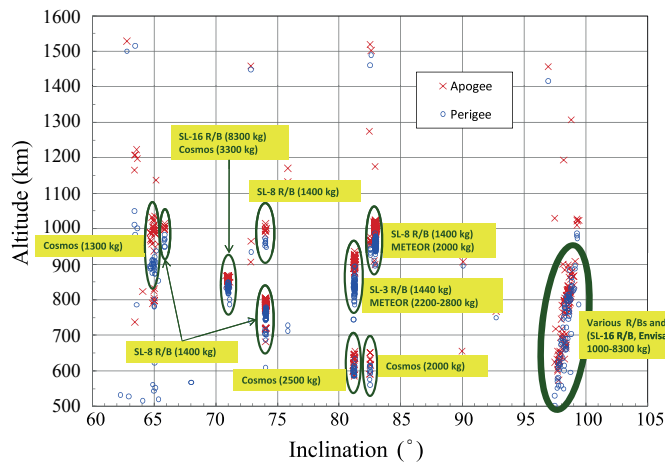


Figure 1.4: Top 500 spent spacecraft and rocket bodies (Liou, 2011)

a mass of about 8230 kg). Since five of them are at a similar inclination, similar Right Ascension of the Ascending Node (RAAN) and similar altitude, they could be removed by a single ADR mission with several kits for cost efficiency according to Van der Pas et al. (2014). Table 1.3 provides four typical potential targets in the priority list by Wiedemann et al. (2012).

Table 1.3: Four typical targets in the priority list by Wiedemann, et al. (Wiedemann et al., 2012)

Name	Type	Owner	Inclination [°]	Apogee [km]	Perigee [km]	Mass [kg]	RAAN [°]
ENVISAT	Satellite	ESA	98.5	767.0	766.0	8111.00	16.2
SL-16R/B	Upper stage	CIS	98.3	814.0	801.0	8225.97	307.3
ALOS(DAICHI)	Satellite	JPN	98.1	693.0	693.0	4000.00	15.3
H-2AR/B	Upper stage	JPN	98.5	840.0	737.0	4000.00	33.6

## 1.2. THE STATE OF THE ART

### 1.2.1. ACTIVE DEBRIS REMOVAL

According to (Sorge, 2015), "Active Debris Removal (ADR) involves changing the orbit of a debris object via the actions of another system". By this definition, other PMD methods, such as the 25-year self-deorbiting safety standard is not considered as an ADR method. In last two decades, many enabling ADR techniques, such as robotic arms (Reintsema et al., 2010), harpoons (Reed et al., 2012), contact-less removal methods (Phipps et al., 1996), net capturing (Bischof et al., 2004), etc. have been proposed, discussed and analyzed. Robotic arm technology has been applied in many on-orbit servicing missions, such as the ETS-7 of JAXA (Kasai et al., 1999), the Canadarm2 (Kauderer, 2008), the Orbital express of DARPA (Whelan et al., 2000) and others (Flores-Abad et al., 2014). However, the targets in these missions were cooperative. For example, four markers were installed on the target satellite for rendezvous in the ETS-7 mission (Kasai

et al., 1999). On the contrary, a typical space debris object will not provide any information to the chaser satellite. Moreover, sometimes the targets may even be tumbling. Therefore, it is more challenging to apply robotic arms in space debris removal missions as compared to on-orbit servicing missions. In the harpoon method, a harpoon mechanism with barbs on its tip can be shot from the chaser satellite and penetrate itself into a large space debris object. The chaser satellite will pull the debris object to re-enter or to a graveyard orbit afterwards (Reed et al., 2012). However, the harpoon method has a risk of generating new fragments and risk of breakup. Furthermore, it is difficult to control the composite with the connecting tether. Contact-less removal methods include the usage of methods such as the usage of an artificial atmosphere, laser or ion beam. The principle of all these methods is to decrease the velocity of space debris objects by ejecting some medium objects in their trajectories thus lowering their altitudes. However, it would always take a long time to remove a target and it is not appropriate to remove a target in Medium Earth Orbit (MEO) or Geostationary Earth Orbit (GEO) using contact-less removal methods. Net capturing is regarded as one of the most promising capturing methods due to its multiple advantages, e.g., it allows a large distance between chaser satellite and target, so that close rendezvous and docking are not mandatory. It is compatible to different sizes, shapes and orbits of space debris objects. Additionally, it is flexible, lightweight and cost efficient. However, it also suffers the difficulty of the post-capture control with the connecting tether during de-orbiting. Although many enabling ADR methods have been proposed, investigated and discussed, their strengths and weaknesses have never been summarized and compared. Moreover, the attempt of tailoring associated capturing and removal methods to different types of debris objects has not yet made. An extended discussion on the existing ADR methods and their properties is included Chapter 2. By comparing the existing ADR methods, net capturing will be the focus throughout this thesis due to its multiple advantages on simplicity and its compatibility to different sizes and shapes of targets. Even though some researches on net capturing have been performed, the feasibility of the net capturing method is not yet fully understood and it needs to be further investigated. For example, net modeling methods and net contact dynamics need to be further investigated and experimentally validated; research on the net capturing of some typical tumbling targets remains open, ect. Following subsections introduce the state-of-art and research gaps related to the net capturing method, including the net modeling, net deployment dynamics and net contact dynamics.

### 1.2.2. DYNAMIC MODELING OF NET CAPTURING

#### NET MODELING

Modeling of a net is an indispensable step to investigate the dynamic characteristics of net capturing system in a simulator. Various dynamic models of a net have been discussed, such as lumped-mass model (Benvenuto et al., 2014), Absolute Nodal Coordinate Formulation (ANCF) (Liu et al., 2014), elastic continuum model (Mankala and Agrawal, 2005) and cubic B-spline model (Gao et al., 2012) (see Fig. 1.5). In a lumped-mass model, a tether is usually assumed to be formed by several small segments. Since a net is comprised of small square meshes, the interaction knot where the cables connected is usually simplified as a mass point, and the tethers connecting these knots are

regarded as spring-damping elements. As early as 1988, [Carter and Greene \(1988\)](#) have proposed a bead model to simulate a tether between a mother satellite and a daughter satellite. The tether is assumed to be comprising of several beads connected by springs and dashpots. [Sidorenko and Celletti \(2010\)](#) have investigated the periodic motions of a tether satellite system using the lumped-mass model. [Benvenuto et al. \(2014\)](#) have developed a net capturing simulator based on this model (see Fig. 1.5 (a)). ANCF for net modeling has been proposed by [Liu et al. \(2014\)](#) (see Fig. 1.5 (b)). In ANCF, absolute displacements and global slopes are applied as nodal coordinates. The mass matrix of the system is constant and symmetric. However, this model is not studied sufficiently, and the dynamic characters of the net are not further investigated based on this model. [Mankala and Agrawal \(2005\)](#) have developed dynamic characteristics of a tether under three conditions based on the elastic continuum model: (a) unchangeable tether length on ground (2) changeable tether length on ground (3) changeable tether length in orbit. Hamilton's principle and Newton's law are applied to establish the dynamic equations for those three conditions, respectively. The models derived from these equations are cross-verified by comparing two sets of the simulation results. ([Koh and Rong, 2004](#)) have investigated the dynamic characteristics of a large displacement cable motion using the elastic continuum model and have validated the model via experiments. Fig. 1.5 (c) shows a differential segment of the cable in a 3D illustration. Model complexity and poor computational performance are fatal disadvantages using an elastic continuum model. Therefore, it takes efforts to integrate tethers into a net based on the continuum model. Cubic B-spline model has been applied to simulate the dynamics a fishing net, where the number of physical nodes is usually over 3 millions ([Gao et al., 2012](#)), to make the bridle and surface go smoothly and continuously ([Bessonneau and Marichal, 1998](#)). This model simplifies the geometry of the fishing net by interpolating the curves between several mass points to realize the real-time visualisation simulation. Fig. 1.5 (d) shows the simulation of a fishing net based on the Cubic B-spline model. In fact, the idea of net capturing method for ADR originally comes from the concept of fishing net used in marine fishery.

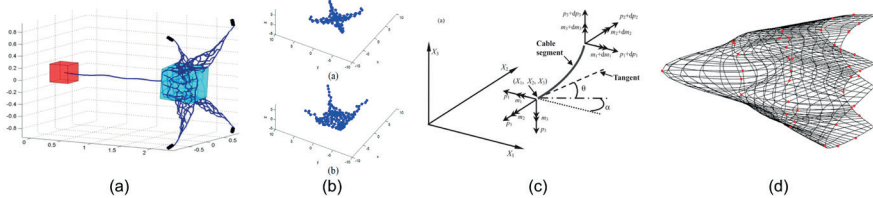


Figure 1.5: Modeling of a net using (a) Mass-spring model ([Benvenuto et al., 2014](#)). (b) ANCF ([Liu et al., 2014](#)). (c) Continuum model ([Koh and Rong, 2004](#)). (d) Cubic B-spline model ([Gao et al., 2012](#)).

### CONTACT DYNAMICS MODELING

[Gilardi and Sharf \(2002\)](#) have divided the contact dynamics models into two main categories: discrete models such as Possion's model and Newton's model, and continuous models such as spring-dashpot model, Hertz's model and nonlinear damping model. The discrete models assume that the impact process is instantaneous and the kinetic

variables have discontinuous changes while no displacements occur during the impact (Wang and Mason, 1992). On the contrary, the continuous models assume that the impact process is not instantaneous and the deformation of the contacting bodies is continuous. Therefore, the normal contact force is the function of the deformation of the contacting bodies. Benvenuto et al. have developed a net simulator based on a lumped-mass model. They assumed the contact between the net and the target a contact of mass spheres with the surface of the target and explored the contact dynamics based on the linear Hertz's model (Benvenuto et al., 2015) and the nonlinear damping model (Benvenuto et al., 2016), respectively. Apart from the sphere-plane contact, Botta et al. (2016b) have investigated the sphere-sphere contact based on a Kelvin-Voigt contact model. They also investigated the different expressions for damping coefficient in the nonlinear damping model, concluding that Zhang and Sharf's expression of damping is more precise (Botta et al., 2016a). However, the above mentioned simulators are both using the continuous model, which has a shortage in selecting the contact stiffness. A large contact stiffness is needed to keep the penetration sufficiently small that will generate large forces leading to a stiff equation system and it has to be decided by experiment. Moreover, a contact stiffness suitable for one situation may not necessarily be adequate for another due to the different materials of the contacting bodies. Additionally, the fictitious penetration between the net and the target cannot be avoided. Gołębowski et al. (2015b) have developed a simulator based on Cosserat rod theory and simulated the net contacting with a target using a predictor-corrector algorithm with which the penetration can be predicted and corrected at every step of the simulation. However, the predictor-corrector algorithm performed at every step of the simulation brings complexity to the simulator. Therefore, there is a need to develop a robust, simple and fast contact modeling algorithm for net capturing.

### 1.2.3. CAPTURING OF TUMBLING DEBRIS

#### DE-TUMBLING

A space debris object may be tumbling due to the residual angular momentum which significantly complicates its capturing. According to the research results by JAXA, tumbling rates below  $3^\circ/\text{s}$  can be captured by a robotic arm easily; tumbling rates above  $30^\circ/\text{s}$  will hardly be treated by a robotic arm; tumbling rates between  $3-30^\circ/\text{s}$  can be de-tumbled using brush contact (Nishida and Kawamoto, 2011). A brush contactor, as the end-effector of robotic arms, is able to release the residual angular momentum of the target by soft and static tapping on the target's surface (Fig. 1.6). The impact influence on the chaser satellite can be released using a joint virtual depth control method (Nishida and Kawamoto, 2011). Aghili (2008) has proposed an optimal control method for intercepting and de-tumbling a target with unknown inertia parameters by a robotic arm. An Ion-Beam Shepherd (see Section 2.4.4), which is an ADR method by emitting a high-velocity ion-beam onto a target to modify its orbit, can also be used for de-tumbling a target (Cano et al., 2014).

#### ATTITUDE SYNCHRONIZATION AND TUMBLING COMPATIBILITY

As previously discussed, for robotic arm capturing, it is not necessary to de-tumble a target when its tumbling rate is relatively small. However, attitude synchronization to

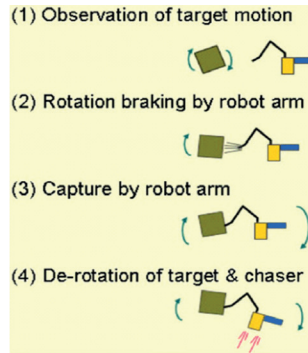


Figure 1.6: Brush contactor (Nishida et al., 2009).

ensure that the capturing point is always directed to the service satellite, is indispensable. Attitude synchronization contains two aspects, one is relative position tracking and the other is attitude reorientation. To keep the capturing motion stable and efficient, it is wise to keep a constant relative distance and attitude between the service satellite and the target coincidentally. An et al. (2013) have developed a compound control method consisting of a nonlinear feedback controller and a sliding mode controller to perform the attitude synchronization of docking to a tumbling target without knowing the bounded external disturbances. Subbarao and Welsh (2008) have developed a translation and attitude controller separately to execute the attitude synchronization. Attitude synchronization and de-tumbling must be performed when necessary before capturing so that the target is stable relative to the chaser using robotic arm capturing method. In this respect, robotic arm capturing is costly and complicated to perform. The net capturing method can overcome this defect due to its compatibility with tumbling space debris with no need of attitude synchronization and de-tumbling before capturing according to Retat and Bischof (2012). However, the acceptable tumbling range of a target using a net is not yet fully understandable. Moreover, a target is non-cooperative and its physical information of the target, like the orientation of the tumbling axis and the tumbling rate is not prior known. A net might be twined by a tumbling target with high angular velocity thus leading to a failed capturing. Therefore, an acceptable tumbling limitation suitable for net capturing needs to be investigated.

### 1.3. RESEARCH QUESTIONS

To fill the remaining research gaps discussed above, this thesis intends to investigate the dynamics of the net capturing method and the feasibility and reliability of a tumbling target capturing using this method. Three specific Research Questions (RQs) for this research are as follows:

**RQ1. Which levels of non-cooperativeness of space debris exist? Which are their associated capturing and/or removal methods and what is the role the net capturing method plays among all those methods?**

The space debris removal mission is similar to the on-orbit servicing mission. How-

ever, in most on-orbit servicing missions, the target to be served is cooperative, i.e., it is either equipped with reflectors for rendezvous or with a docking system for capturing. Moreover, the geometry information, such as the center of mass and the inertia of the target, or the dynamic characteristics of the target is prior known as well. On the contrary, space debris can vary widely in those characteristics. Typical space debris objects are non-operational satellites, rocket upper stages and fragments from explosions or collisions. They are non-cooperative targets and will not provide any information to a chaser satellite which renders ADR missions are more complex than the on-orbit servicing missions. Many kinds of capturing and removal methods have been proposed and investigated by researchers till now. Since the non-cooperative levels of each debris are different based on their characteristics, the most appropriate capturing and removal method for each debris is expected to be different. As a result, the non-cooperative levels of debris and the tailored associated capturing and removal methods need to be developed. Moreover, since the net capturing method will be the focus of this research due to its multiple advantages, there is a need to be aware of the role the net capturing method plays among all those methods.

### **RQ2. What are the dynamic characteristics of the net capturing method?**

This research question aims at investigating the net deployment dynamics and the contact dynamics between the net and the target. The chaser satellite is approaching to a target before shooting its net. Important information such as the distance between the chaser satellite and the target, how long the net can reach to the target and how big a net can deploy should be prior known. The net deployment dynamics needs to be investigated in a simulator. A proper net modeling method needs to be chosen and the net modeling method needs to be investigated and verified. During the capturing process, the contact between the net and the space debris target might push the target away or change its status if inappropriate contact is made. Therefore, understanding the contact dynamics and ensuring a successful capture is crucial.

### **RQ3. How to reliably capture a tumbling and non-cooperative debris object using the net capturing method?**

Space debris might be tumbling due to their residual angular momentum. Therefore, research on how to treat these tumbling targets is crucial. For a space debris object with a low tumbling rate, capturing might be performed directly. However, for a space debris object with a high tumbling rate, the net might be twined by a high tumbling angular velocity thus leading to a failed capturing or de-orbiting. Therefore, there is a need to investigate the acceptable range of the tumbling rate of a target using the net capturing method. Moreover, necessary measures shall be taken to ensure that the capturing of a target tumbling at high rates is successful.

## **1.4. METHODOLOGY**

This section briefly introduces the methods used in this thesis, such as modeling establishment, numerical simulations, and verification and validation in answering the research questions formulated above.

### 1.4.1. DYNAMICS MODELING

Dynamics modeling of the net capturing system consists of two segments: the net deployment dynamics and the net contact dynamics. In the net deployment dynamics part, two models are used to perform a sensitivity analysis of the initial input parameters on the output parameters, one is the mass-spring (MS) model and other one is the absolute nodal coordinates formulation (ANCF). The mass-spring model approximates a flexible cable as a series of mass points connected by mass-less spring-damper elements. While the ANCF model uses the absolute positions and the gradients of the positions to act as the element nodal coordinates so as to describe the flexibility of a cable system. In the contact dynamics part, two contact modeling methods, the penalty-based and the impulse-based method are used to investigate the dynamics between the net and targets. In the penalty-based method, contact force is expressed as continuous functions of the penetrations between contacting bodies. However, the impulse-based method calculates the impulse applied on the contacting bodies, thus calculating the velocity changes of them.

### 1.4.2. NUMERICAL SIMULATION

To investigate the dynamics of the net capturing system, simulation needs to be performed based on the aforementioned models. The computation of those models can only be achieved by using numerical integration methods. The simulator is developed in Matlab throughout this thesis. All the simulations are performed by a processor of Intel Core i5-4670 CPU with 8 Gigabytes (GB) installed memory. The system equations established in this thesis are either differential algebraic equations (DAEs) or the ordinary differential equations (ODEs). Some DAEs are converted to ODEs then solved by the 4th order of Runge-Kutta method (RK4) that is a single-step and explicit integration algorithm which indicates no use of the data calculated in the previous steps. RK4 is particularly easy to implement and may be widely used in different problems. However, the step-size of RK4 or even all the explicit algorithms should not be too small or too large. A small step-size might increase the steps of the integration, the round-off errors etc., while a large step-size might affect the stability of the equation and the accuracy. Step-size control method has been described in ([Montenbruck and Gill, 2012](#)).

### 1.4.3. CROSS-VERIFICATION AND VALIDATION

As previously mentioned, several models are investigated in this thesis, including the mass-spring model and the ANCF model in the net deployment dynamics, plus the penalty-based and the impulse-based method in the net contact dynamics. Among those models, the ANCF model and the impulse-based model, to the author's knowledge, are for the first time deeply investigated in this thesis. These models have to be verified and validated. The cross-verification is made by comparison of the simulation results obtained by two models, while the validation is made by comparing simulation with a parabolic flight experiment that is performed under an ESA contract. Trajectory of four bullets are collected and compared since the bullets are able to describe the general configuration of the net to some extent. To further quantitatively analyze the difference of the pair of data, the differences of these four bullets trajectories are obtained by taking the absolute value of the subtraction of the data, then reported using boxplot.

## 1.5. THESIS OUTLINE

This thesis consists of six chapters, and is structured as described in the sequel.

Following the current chapter with its description of the problem statement and the research questions, Chapter 2 presents an overview of enabling techniques for active debris removal. This chapter divides space debris into three main categories and provides typical exemplary targets for each category. Furthermore, methods for space debris capturing and removal are reviewed and the advantages and drawbacks of the most relevant methods are identified and analyzed as well. Finally, a tailored associated capturing and removal method for each category of space debris is provided. Based on the comparison, net capturing is considered as a promising method among others. An extensive study on dynamics of the net capturing method is, therefore, performed in the following chapters.

Chapter 3 investigates the deployment dynamics for the net capturing method. Two modeling methods of a net are established, one is based on a mass-spring model, the other is based on the absolute nodal coordinates formulation (ANCF). A sensitivity analysis of the initial input parameters on the output parameters is performed based on both models. Both models are cross-verified by each other, and validated by a parabolic flight experiment. The absolute and the relative residuals differing from the simulations and the parabolic flight experiment results are determined.

Chapter 4 investigates the contact dynamics for the net capturing method. In this chapter, two contact modeling methods: the penalty-based method and the impulse-based method are introduced, compared and analyzed. Numerical simulations of an Envisat mock-up capturing based on both methods are performed. The simulation results are then compared with the parabolic flight experiment results to evaluate the effectiveness of both models. In addition, strengths and weaknesses of these two contact dynamic models are identified and compared.

Chapter 5 focuses on the free-floating and tumbling space debris objects capturing using a net. Using the mass-spring model for the net and the impulse-based model for the contact dynamics, the capturing of three targets is investigated to demonstrate net's compatibility to the targets with different sizes and shapes, one is a 3-unit Cubesat without appendages, one is the second upper stage of the Zenit-2 rocket and another one is the Envisat satellite. Simulation results provide a threshold of the tumbling rate of a target that a free-throwing net is capable to capture. Since a highly tumbling target is possible to slip out of a net, a closing mechanism is designed and applied on the net to ensure that the target is encompassed in the net.

Chapter 6 summarizes the findings of this research and answers the research questions in a summarized way. The challenges and strengths of the net capturing method are identified based on those findings. Furthermore, it draws conclusions from this thesis work. The main research contributions and innovations from this thesis are addressed and highlighted as well. Finally, it provides recommendations for future studies and gives an outlook to the relevance of the net capturing method for ADR.



# 2

## SPACE DEBRIS CAPTURING AND REMOVAL METHODS

---

Parts of this chapter have been published in M. Shan, J. Guo, E. Gill, *Review and Comparison of Active Space Debris Capturing and Removal Methods*, *Progress in Aerospace Sciences* **80**, 18-32 (2016).

## 2.1. INTRODUCTION

Operations of satellites in the Earth's orbit are in a serious predicament caused by millions of space debris objects. Operational satellites, vital for mankind's infrastructure, are threatened to be destroyed by collisions with those space debris objects. In this context, all space companies and organizations are suggested to follow the 25-year safety standard which means a satellite should either lower its orbit and re-enter (for debris in LEO and MEO), or raise itself to a graveyard orbit within 25 years after the mission ends (for debris in GEO) (NASA, 1995). Even if this rule was followed, which is not enforced up to now, around 5-10 space debris objects still need to be removed each year to stabilize the space environment according to a prediction model by Liou (2011). In this respect, ADR missions are of great relevance and urgency. The ADR missions have some similarities with the on-orbit servicing missions. However, in most on-orbit servicing missions, the target to be served is always cooperative, e.g., some physical fixtures exist on the target to help the rendezvous and/or docking process. The geometry information, such as the center of mass or the inertia of the target is known as well. In contrast to the on-orbit servicing missions, space debris can vary widely in characteristics, e.g., non-operational satellites, rocket upper stages, and fragments from explosions or collisions. These are all non-cooperative targets and would not provide any information to the chaser satellite or their operators which makes ADR more complicated. Many kinds of capturing and removal methods have been proposed in the past and investigated by researchers till now. Since the level of non-cooperativeness of each debris object can be different based on their characteristics, the most appropriate capturing and removal method can be different for each debris object. As a result, the non-cooperative levels of debris objects and the tailored associated capturing and removal methods need to be investigated and developed. To gain the knowledge of non-cooperativeness of space debris and associated appropriate ADR method, this chapter provides a classification of space debris objects, a review of existing active space debris capturing and removal methods as well as the tailored associated ADR methods for different categories of space debris.

## 2.2. CLASSIFICATION OF SPACE DEBRIS

In the past 60 years of space activities, more than 5250 launches resulted in more than 42 000 tracked objects in the Earth orbit, of which 18 753 objects remain in space that comprise objects larger than 10 cm in LEO and 30 cm - 1 m in GEO as of September 2017. Among those remaining objects, only 1880 payloads are active in space, i.e., around 10% are operational satellites working in an environment where 90% of the populations are space debris objects. These space debris objects can be categorized into three main groups: non-operational satellites, rocket upper stages and fragments from explosions and collisions. Among those tracked space debris objects, 22% of them are non-operational satellites, 17% of them are rocket upper stages, and the rest are fragments from explosions or collisions and other mission-related objects (Website, 2017c). However, not all of them are endangering the operational satellites. In terms of the spatial and mass distribution of space debris objects, the most threatening space debris objects are the ones located in the most crowded orbital region with large masses (Liou, 2011). A list of 22 of the most critical ADR targets has been provided in (Van der Pas et al., 2014),

Table 2.1: Classification of space debris objects (Website, 2017c; Liou, 2011; Van der Pas et al., 2014)

Category	Representatives	Percentage
<b>Non-operational Satellites</b>	Envisat, ALOS, Cosmos and Meteror	22%
<b>Rocket Upper Stages</b>	Zenit 2, H-2A, Ariane and CZ-series	17%
<b>Fragments</b>	Fragments from the Collision of Iridium 33 and Cosmos 2251, Rocket body fragments from explosions	61%

with ESA's Envisat being the most threatening target. The next non-operational satellite on the list is the Japanese ALOS. The other threatening debris objects on the list are mostly rocket upper stages of the Russian Zenith-2. Liou (2011) also provided a top 500 list of non-operational satellites and rocket upper stages with the highest masses and collision probabilities. Typical representatives of non-operational satellites on this list are: Envisat, Cosmos and Meteror-series of satellites. A large amount of other threatening objects on this list are spent rocket bodies. They include, for example, Zenith 2nd stages, Ariane upper stages and ChangZheng (CZ)-series rocket bodies, etc. (Liou, 2011). Even worse than satellites, rocket upper stages have a risk to explode. NASA summarized the top ten space breakups list as of January 2016, six of which are due to the accidental explosion of rocket bodies (NASA Orbital Debris Program Office, 2016). These accidental explosions account for 2904 catalogued fragments in total or 15% of the entire catalogued man-made objects. Another way of generating fragments is the accidental collision in space. The most significant satellite collision is the collision of Cosmos 2251 and Iridium 33 spacecraft, which is the first ever accidental hyper-velocity impact of intact objects in February 2009. A total of 2296 fragments were generated from this collision (NASA Orbital Debris Program Office, 2016). Table 2.1 lists the classification of space debris objects. Representatives and percentage for each category are given as well. In this thesis, we focus on those debris objects that can be tracked by U.S. SSN, i.e., those objects whose size is larger than 10 cm.

## 2.3. CAPTURING METHODS

A space mission for active space debris capturing and removal consists of the following phases: launch and early orbit phase, far-range rendezvous phase, close-range rendezvous phase, capturing phase and removal phase. These phases can be performed either autonomously and/or remotely controlled by ground-based mission operations. The capturing phase plays a crucial role in the entire mission process. Conceptually, many methods for space debris capturing have been proposed. According to the mechanical flexibility of their connections of the chaser satellite to the target, space debris capturing methods can be divided into two main categories: stiff-connection capturing and flexible-connection capturing. Stiff-connection capturing methods include the robotic arm capturing and the tentacles capturing. Flexible-connection capturing methods include the net capturing, the tether-gripper capturing and the harpoon capturing. The end-effectors in the flexible-connection capturing methods, such as the net,

the gripper and the harpoon are connected with the chaser satellite by a tether. Capturing methods in both categories will have physical contacts with the target by their end-effectors.

## 2

### 2.3.1. STIFF-CONNECTION CAPTURING

Stiff-connection capturing methods refer to the space debris capturing methods which have stiff links between the chaser satellite and the space debris object. The link in a stiff-connection capturing method can either be a robotic arm or tentacle.

#### SINGLE ARM CAPTURING

Robotic arm technology has been applied in many on-orbit servicing missions, such as the ETS-7 of JAXA (Kasai et al., 1999), the Canadarm2 (Kauderer, 2008), the Orbital express of DARPA (Whelan et al., 2000) and others (Flores-Abad et al., 2014). However, it is more challenging to apply robotic arms in space debris removal missions as compared to on-orbit servicing missions. To verify the process of capturing a non-cooperative space debris object, DLR has been developing robotic arm technologies in a mission named Deutsche Orbital Servicing Mission (DEOS). The client satellite to be captured represents a non-cooperative and tumbling target which does not provide any information for rendezvous and capturing. The entire process from far-range rendezvous to de-orbiting is, however, to be performed in this mission (Reintsema et al., 2010). In order to simulate the contact behaviors during capturing and docking in space systems, DLR has developed a simulator called European Proximity Operations Simulator (EPOS). EPOS is a ground-based hardware-in-the-loop facility to test, e.g., the dynamic behavior while docking (Zebenay et al., 2012). This testing facility is able to simulate the docking and capturing processes from 25-0 m. Two KUKA robots represent the service and the client satellite respectively. One of them slides on a pair of rails performing the approaching motion, while the base of the other one is fixed (Boge et al., 2010). Zebenay (2014) has investigated the contact dynamics of inserting a probe into the nozzle cone of an apogee kick motor using a hybrid docking simulator primarily in one dimension. The hybrid docking simulator combines a hardware passive compliance between the probe and the kick motor with virtual contact dynamic model. This technology supports non-operational satellite or spend rocket upper stage capturing (Zebenay, 2014). DARPA developed the Front-End Robotics Enabling Near-Term Demonstration (FREND) program to demonstrate the robotics technology and perform unaided capturing. The FREND arm has been designed, assembled and tested. It shows a higher stiffness and accuracy than the robotic arms for the Mars Exploration Rovers, Phoenix Lander, Space Station and Space Shuttle (Debus and Dougherty, 2009). Fig. 2.1 displays these three concepts for single robotic arm capturing.

#### MULTIPLE ARMS CAPTURING

The Advanced Tele-robotic Actuation System (ATLAS), a program from UK (Ellery, 1999), consists of two robotic arms tele-robotically controlled from ground (Fig. 2.2). Multiple arms can be used in robotic assembling of a space structure, robotic refueling and space debris removal (Yoshida, 2009). (Yoshida et al., 1991) have investigated the kinematics and dynamics of dual arm on a free-flying robot, concluding that the second arm is able

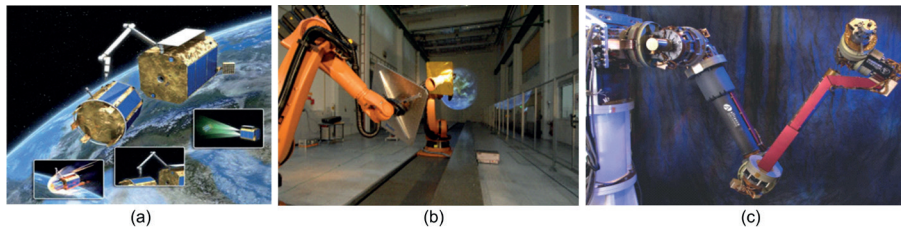


Figure 2.1: Single arm capturing methods. (a) DEOS (Reintsema et al., 2010). (b) EPOS (Boge et al., 2010). (c) FRENED (Debus and Dougherty, 2009).

to stabilize the satellite. Moreover, the second arm also makes the system flexible since it accomplishes a difficult task by cooperating with the first one.



Figure 2.2: Multiple arms capturing (ATLAS) (Ellery, 1999).

A mechanical end-effector installed at the end of a robotic arm is directly involved in the capturing motion and contacting with the target. The success of the space debris removal mission depends highly on the reliability and stability of an end-effector. Therefore, the mechanical end-effector plays an crucial role in either single or multiple robotic arms capturing. There are several concepts of mechanical effector for capturing a space debris object, such as a probe for the nozzle cone of an apogee kick motor, a Payload Attach Fitting (PAF) adaptor, a two-finger mechanism, an articulated hand, and a universal gripper. Five mechanical effectors are shown in Fig. 2.3. The principle of a probe capturing (Fig. 2.3 (a)) is to expand the top part of the probe to the inside surface of a nozzle cone after inserting the probe into the cone, thus capturing the target. DLR has engaged in the Experimental Servicing Satellite (ESS) study which is supposed to inspect, approach, catch, dock and repair a non-operational satellite (Landzettel et al., 1994). The visual servoing during capturing using the probe effector was tested on two robotic arms: one carried a mockup of a nozzle cone of an apogee kick motor, the other carried the probe mechanism and captured the mockup (Hirzinger et al., 2004).

The PAF (Fig. 2.3 (b)) refers to a V-flange in the rear of satellites as a mechanical interface with the launch adaptor. The V-flange grasping requires an open contact, i.e.,

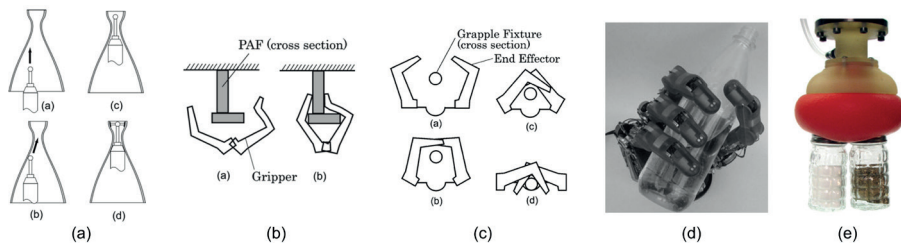


Figure 2.3: Mechanical end-effectors. (a) Probe (Yoshida and Nakanishi, 2003). (b) PAF adaptor (Yoshida et al., 2004). (c) Two-finger mechanism (Yoshida et al., 2004). (d) Articulated hand (Hirzinger et al., 2004). (e) Universal gripper (Amend et al., 2012).

the fingers do not cross each other and they keep open after capturing (Yoshida et al., 2004). However, open contact has the risk of pushing a target away during capturing.

The configuration of the two-finger capturing mechanism (Fig. 2.3 (c)) is similar to the docking system of ETS-7. This mechanism forms a closed space before contact with the grapple fixture. In this respect, the contact is called closed contact to distinguish with the open contact. Closed contact would not push the target away after the closed space is formed. However, the grapple fixture should be a ring which seldom exists on satellite at a perfect position for capturing.

The dexterous hand (Fig. 2.3 (d)) for an on-orbit service mission is developed by DLR as well. This articulated hand mimics the powerful human hand in certain aspects. It is controlled by a tele-manipulation set-up and human operator (Hirzinger et al., 2004). However, since the grasping motion is completed by a collaboration between fingers and palm, the model of grasping motion is strongly coupled.

The universal gripper (Fig. 2.3 (e)) is able to treat complex-shaped objects using the deformation of granular material. The gripper is able to capture or release an object by vacuum-hardening or inflating the granular material encased in a membrane (Amend et al., 2012). Several experiments have been executed to test its reliability. However, this gripper is not adaptive to capture a free-flying object since a force closure needs to be formed during capturing when using this gripper.

### TENTACLES CAPTURING

The tentacles capturing method uses a tentacles-shaped mechanism that can be coordinately used to capture a space debris object. Many types of tentacles have been proposed and designed (Fig. 2.4). In ESA's e.Deorbit project (Fig. 2.4 (a)), capturing using tentacles can be performed either with or without a robotic arm. With a robotic arm used, tentacles embrace the space debris object with a clamping mechanism after holding a point on the target by the robotic arm. Finally, a velocity increment by the chaser will de-orbit the combined object (Biesbroek, 2012). However, a trade-off shows that tentacle capturing with a robotic arm leads to a higher cost, mass, volume, hazardousness and complexity of design compared to the one without a robotic arm (Forshaw, 2014). The simulation of the target grabbing without a robotic arm has been performed successfully, but the GNC requirements are more stringent due to high precision requirements (Forshaw, 2014). Tentacles capturing without a robotic arm follows the "capturing

before touching" strategy, i.e., the tentacles should ideally embrace the target before performing physical contact. In this way, the bouncing of the chaser satellite is avoided and the attitude control system is allowed to stand by during capturing. The clamping mechanism is then locked and the connection of the composite (chaser and target) essentially turns stiff after capturing (Wormnes et al., 2013).

Aviospace is working on the project CADET (Fig. 2.4 (b)) which performs space debris object capturing using tentacles. The tentacles are in a closed configuration made by belts to soften the contact between tentacles and target. Finite element models have been established to simulate the capturing process and assess the dynamic behavior during the chaser-target mating process. Several concepts of the ground-based tests have been proposed, and the detailed design has been in progress (Chiesa and Alberto, 2014).

Another type of tentacles is inspired by biology, i.e., linked to the morphology and function of snakes, elephant trunks or octopus arms, respectively. Two examples are provided in this chapter. Yoshida and Nakanishi (2001) have proposed a concept of Target Collaborativize (TAKO) Flyer (Fig. 2.4 (c)) which contains a main service satellite and a TAKO Gripper. Since most of non-operational satellites are tumbling and failed to provide information to the chaser satellite, the TAKO Flyer is designed for collaborativizing the target by capturing the target and stabilizing its tumbling motion through several thrusters' operations. Those thrusters are installed on the TAKO Gripper. The grapple fixtures and optical markers on the TAKO Gripper render the target cooperative to the main chaser satellite. The TAKO Gripper is comprised of several fingers actuated by gas pressure in the pneumatic bellows. However, the performance of this concept still needs to be verified (Yoshida and Nakanishi, 2001). McMahan et al. (2006) have designed a continuum manipulator named OctArm (Fig. 2.4 (d)). OctArm version V contains three sections connected by endplates. Each section is constructed with air muscle actuators, and it is capable of two-axis bending and extension with nine degrees of freedom.

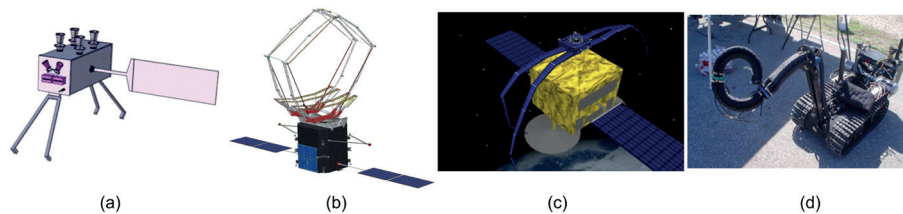


Figure 2.4: Tentacles capturing. (a) e.Deorbit (Biesbroek, 2012). (b) CADET (Chiesa and Alberto, 2014). (c) TAKO (Yoshida and Nakanishi, 2001). (d) OctArm (McMahan et al., 2006).

### 2.3.2. FLEXIBLE-CONNECTION CAPTURING

For the robotic arm and the tentacles capturing, the connection between the chaser satellite and the target is stiff after capturing. This makes the composite controllable and stable after capturing. However, the mass, the cost and the complexity of the system may dramatically be increased. To overcome this drawback, flexible-connection capturing methods in which the end-effector and the chaser satellite are connected by a tether,

are proposed. The tether concept used in space was first proposed in 1960s with an idea of space elevators which is inspired by Eiffel Tower (Artsutanov, 1960). Kruijff (2011) has deeply discussed the tether applications in space, tether dynamics, tether deployer system, collision risk, and missions of the Young Engineering's Satellite (YES) and the YES2. With the development of space technology, many space concepts and/or missions have been proposed or implemented using tethered system, such as cargo transfers between spacecraft, upper atmospheric research, geomagnetic field investigation and space debris collection (Chen et al., 2013).

### NET CAPTURING

Four different concepts of net capturing for ADR are provided in Fig. 2.5. The Robotic Geostationary Orbit Restorer (ROGER) (Fig. 2.5 (a)) is sponsored by ESA, and its objective is to transport a target in GEO into a graveyard orbit, i.e., an orbit a few hundred kilometers higher than the operational altitude regime, with either a net or a gripper mechanism. The net capture mechanism consists of four flying weights in each corner of a net. The flying weights, named "bullets", are shot by a spring system, named "net gun". These four bullets help expand the large net thus wrapping the target that will be transported by the tether connecting the chaser and the net (Bischof et al., 2004). ESA also issued the e.Deorbit project (Fig. 2.5 (b)), in which the net capturing method is one of several concepts for ADR (Biesbroek, 2012). The principle of net capturing in this project is similar to the ROGER. Parabolic flight experiments have been performed by GMV and ESA to validate the net deployment and capturing simulations (Lorenzo et al., 2015). At Politecnico di Milano, a project named Debris Collecting Net (D-CoNe) (Fig. 2.5 (c)) has been performed (Lavagna et al., 2012). University of Colorado at Boulder has proposed a net concept called REsearch and Development for the Capture and Removal of Orbital Clutter (REDCROC) (Fig. 2.5 (d)). The REDCROC system is comprised of structures of inflatable booms and nets configured aside. The net capturing mechanism in REDCROC project works together with the Gossamer Orbit Lowering Device (GOLD), a removal method which will be introduced in removal methods in this chapter. Thus, no propulsion system is needed using this capturing mechanism (Zinner et al., 2001).

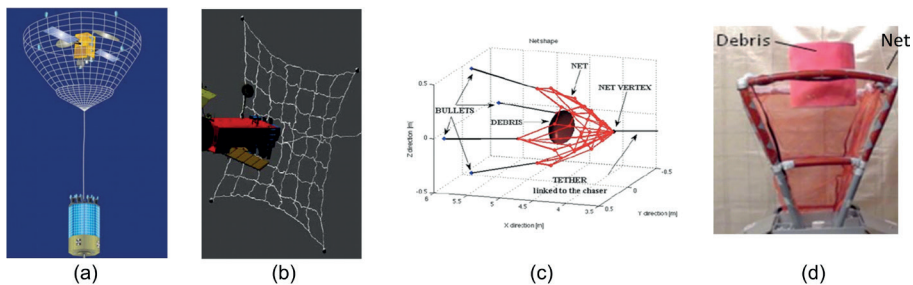


Figure 2.5: Net capturing. (a) ROGER (Bischof et al., 2004). (b) e.Deorbit (Biesbroek, 2012). (c) D-CoNe (Lavagna et al., 2012). (d) REDCROC (Zinner et al., 2001).

### TETHER-GRIPPER MECHANISM

The tether-gripper is the other mechanism introduced in the ROGER besides the net concept (Fig. 2.6 (a)). The principle of the tether-gripper mechanism is similar to the net capturing mechanism, except for the end-effector which is a 3-finger gripper for capturing a target (Bischof et al., 2004). The 3-finger gripper is designed to be able to catch a specific part of the target precisely and stably which leads to the requirements for the tether-gripper mechanism being more stringent and more complicated than the net capturing in operation. Huang proposed a tethered system named Tethered Space Robot (TSR) (Fig. 2.6 (b)) (Huang et al., 2013) and he has deeply investigated the tethered gripper robot for ADR in various areas, including visual servoing technology (Cai et al., 2014), coordinated orbit and attitude control (Wang et al., 2014b) (Huang et al., 2015a), post-capture control (Huang et al., 2014) (Huang et al., 2015b), and composite de-tumbling (Wang et al., 2014a) (Wang et al., 2015). When the chaser satellite travels with the target to re-enter using the tethered system, there is a risk of collision between the chaser satellite and the target if improper movement is performed. Parameters, such as physical properties of the tether, inertia of the target, tether tension force and initial conditions would affect the re-entry. Based on the research by Aslanov and Yudin (2013), the tether has to be tension all the time to ensure a safe transportation during re-entry, and the force vector of the chaser satellite needs to align to the tether direction.

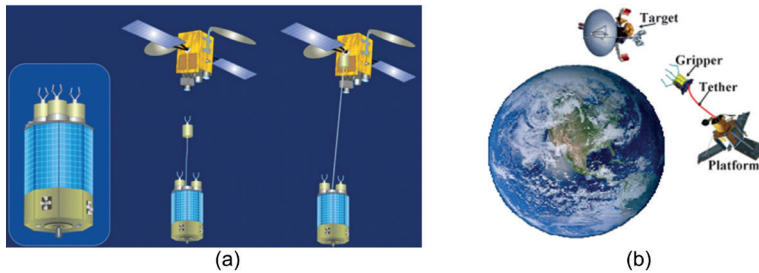


Figure 2.6: Tether gripper concepts. (a) ROGER (Bischof et al., 2004). (b) TSR (Huang et al., 2013).

### HARPOON MECHANISM

A harpoon mechanism with barbs on its tip can be shot from the chaser satellite and penetrate itself into a large space debris object. The chaser satellite will pull the debris to re-enter or to a graveyard orbit. It is considered as an attractive capturing method because of its compatibility with different shaped targets, stand-off distance allowed and no grappling point needed. Since penetrating happens in this case, the risk of generating new space debris is high. Moreover, the risk when treating a target with high tumbling rate is not clear. A Grappling System (GS) has been proposed by Astrium (Fig. 2.7 (a)). Some experiments and tests have been operated on ground (Reed et al., 2012). Tiny fragments were generated through penetrating in these experiments. Different sizes of fragments were generated at different shooting angles to a flat aluminum plate. Since the fragments will stay inside the target, it is believed that the debris generating is not a fatal issue (Reed et al., 2012). Harpoon capturing method is also one of the concepts from e.Deorbit (Fig. 2.7 (b)). Based on the trade-off results with net method by ESA, harpoon

mechanism attracted more attention due to the cost efficiency and higher Technology Readiness Level (TRL) (Billot et al., 2014). Even though the net method has a better system performance and less physical constraints, the harpoon method has been suggested by ESA due to its easiness to be tested on ground (Robin et al., 2015).

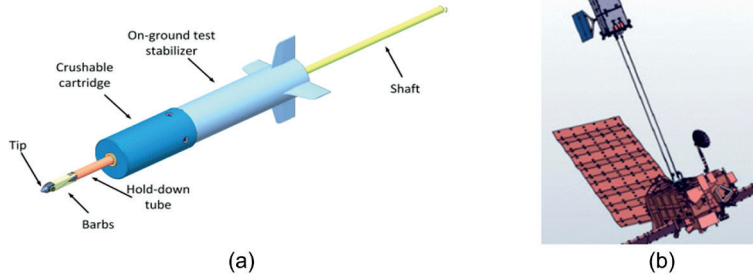


Figure 2.7: Harpoon mechanism. (a) GS (Reed et al., 2012). (b) e.Deorbit (Robin et al., 2015).

Based on the detailed information about each capturing method for ADR, it is found that advantages and drawbacks exist in any of those options. There is no single capturing method, which can deal with all types of space debris objects. A comparison of these methods is provided in Table 2.2 which lists the most relevant and investigated capturing techniques for space debris removal missions along with their advantages and drawbacks.

## 2.4. REMOVAL METHODS

Capturing methods involve building a connection between a chaser satellite and a target, while removal methods involve changing the orbit of a target by a chaser satellite. Therefore, removal methods are fundamentally different from capturing methods. In some cases, removal is performed after capturing. However, in most cases, removal methods avoid capturing at all. The most relevant and promising removal methods are Drag Augmentation System (DAS), Electro-Dynamic Tether (EDT), contact-based and contactless removal methods.

### 2.4.1. DRAG AUGMENTATION SYSTEM

Increasing the area-to-mass ratio of a space debris object is a way of increasing influence of atmosphere drag. The idea of the DAS is to eject some substances with small density but large volume from the chaser satellite onto the surface of the target and stick onto it. The substances on the target increase the area-to-mass ratio thus increasing the influence of atmosphere drag. Drag augmentation method allows a large distance between the chaser satellite and the target. Therefore, no close-range rendezvous or docking is required using this method. Moreover, it reduces the requirements for the chaser satellite since the reentry process is performed by the atmosphere drag influence on a target instead of the chaser satellite. In addition, it is compatible with different sizes of space debris objects. Due to the distribution of atmospheric density in altitude, the targets to be removed using this method should be orbiting in LEO. Three methods to remove

Table 2.2: Overview of relevant capturing techniques

Capturing Methods	Advantages	Drawbacks	Examples	Institute/Sources
Single Robotic Arm	1.Stiff composite 2.Easy to test on ground; 3.Higher TRL	1.Higher probability of collision; 2.Grappling point required; 3.Rendezvous and docking needed.	DEOS	DLR
			EPOS	DLR
			FREND	DARPA
Multiple Arms	1.Stiff composite 2.Easy to test on ground; 3.Flexible capturing	1.Complex control system; 2.Higher mass and cost; 3.Rendezvous needed.	ATLAS	UK
Tentacles	1.Stiff composite; 2.Easy to test on ground; 3.Higher Technology Readiness Level(TRL)	1.Complicated rendezvous phase; 2.Possible to be bounced; 3.Accurate relative positioning and velocity needed.	e.Deorbit	ESA
			CADET	Aviospace
			TAKO	Japan
			OctArm	USA
Net Capturing	1.Allows a large capturing distance; 2.Reduced requirements on precision; 3.Compatible for different size of debris.	1.Hard to control;  2.Risk of critical oscillations;  3.Hard to test on ground.	ROGER	ESA
			e.Deorbit	ESA
			D-CoNe	Italy
			REDCROC	USA
Tether Gripper	1.Allows a large capturing distance; 2.Short capture operation time; 3.Lower mass and cost.	1.Difficult to test on ground; 2.Grappling point required; 3.Lower reliability.	ROGER	ESA
			TSR	China
Harpoon	1.No grappling point required; 2.Allows a stand-off distance to target; 3.Compatible with different target types (rocket body or satellite).	1.Risk of generating fragments; 2.Risk of breakup  3.Flexible connection, difficult to predict the movement of a target.	GS	Astrium
			e.Deorbit	ESA

space debris based on this concept are introduced as follows (Fig. 2.8).

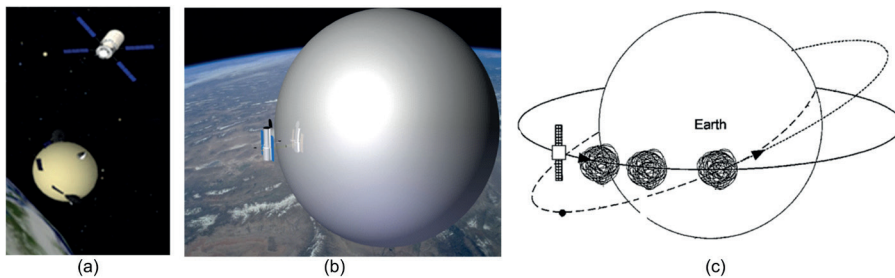


Figure 2.8: Drag augmentation system

### FOAM METHOD

After a chaser satellite rendezvousing with a space debris object and flying around it, foam is ejected from the ejection device installed on the chaser satellite onto the target and sticks on it. Then the foam covers the whole target and turns it into a foam ball. The area-to-mass ratio is increased due to the small density and large volume of the foam (Andrenucci et al., 2011). However, the foam should be stiff enough so that the foam ball will not be destroyed by other small pieces of space debris and new space debris will not

be generated. The optimum foam material is still under discussion (Andrenucci et al., 2011).

### INFLATED METHOD

In this method, an inflated ball replaces the foam ball as a drag augmentation system. The Gossamer Orbit Lowering Device (GOLD) (Nock et al., 2010) is a typical concept of this method. A large, lightweight, and inflatable envelop, which can reduce object ballistic coefficients by up to two orders of magnitude during re-entry, can be either attached onboard or on a space debris object. Based on a risk analysis, GOLD offers lower risks in terms of large debris generation and disabling other operational satellite compared with propulsive de-orbit methods (Nock et al., 2010). However, the fatal disadvantage is that the mission would fail once the inflated ball is destroyed by other small pieces of space debris.

### FIBER-BASED METHOD

Fiber-based removal methods use fibers to expand a space debris object. The working principle of the fiber-based removal method is the same as the above discussed methods. The fibers are extruded by a heat source and wound around a target to expand it thus increasing the area-to-mass ratio (Wright, 2013).

#### 2.4.2. ELECTRO-DYNAMIC TETHER

The EDT removal method was originally used in orbit transfer and orbit maneuvering (Williams, 2005). It is a method taking advantage of the geomagnetic field to reenter (Fig. 2.9). In this aspect, a propulsion system is not mandatory onboard during re-entry. When performing space debris removal using EDT, a space robot firstly captures a target using a robotic arm or a harpoon and installs an extendable electro-dynamic tether on it. The Lorentz force generated from the interaction between the electric current flowing in the conductive tether and the geomagnetic field is exploited to decrease the space debris object (Estes et al., 2000). An EDT package is comprised of a bare conductive tether and two filed emitter array cathodes. One collects electrons and the other emit electrons in which way current is generated (Nishida et al., 2009). The space robot can slide to another space debris object after installing the EDT on one object. However, capturing is indispensable in this method, which indicates robotic arm technology or other capturing method has to be applied in this concept. The Electro-dynamic tether is prone to libration instability due to the complex space environment, such as periodic changes of the geomagnetic field, lunisolar gravitational attractions and the Earth's oblateness. The material for the tether is still under discussion since it should survive the extreme space environment during the entire de-orbiting period (Dong et al., 2014). Two practical drawbacks for this concept are: it cannot treat targets beyond LEO due to the insufficient intensity of the Earth's magnetic field; the other is that the Lorentz force depends largely on the current going through the tether. Therefore the thrust is not large enough to realize a required orbit transfer when the current is low (Tragesser and San, 2003).

#### 2.4.3. CONTACT-BASED REMOVAL METHODS

The above introduced removal methods are space environment based methods. On the other hand, non-space environment based methods can be divided into two main cat-

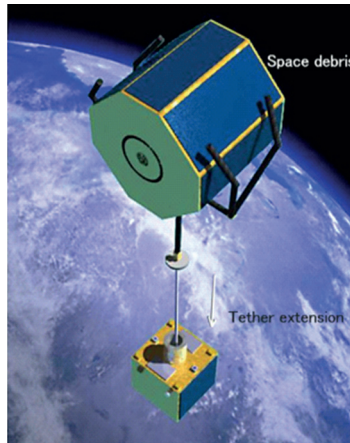


Figure 2.9: Electro-Dynamic Tether (Williams, 2005).

egories: contact-based removal methods and contactless removal methods. Contact-based removal method is a concept that takes advantage of a direct interaction between the chaser satellite and the target during the removal process. The slingshot method and the adhesive method are two typical removal approaches in this category (Fig. 2.10).

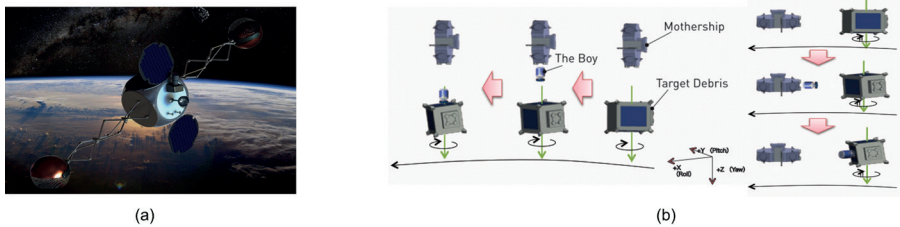


Figure 2.10: Contact-based removal methods. (a) Slingshot method (Missel and Mortari, 2013). (b) Adhesive method (Okada, 2014).

### SLINGSHOT METHOD

The University of Texas has developed a satellite called "Sling-Sat Space Sweeper" (4S), which is designed for saving energy for ADR since it is designed to remove multiple targets in one launch. The satellite can capture a space debris object and eject it towards the Earth. Then it slides to another space debris object applying the momentum generated from the ejection (Missel and Mortari, 2013). The 4S satellite is composed of two collectors connected by two deployable masts, which are tri-scissors in this case. When slinging a space debris object, the sling-sat undergoes four configurations which are: capture, spin-up, expulsion and return. A contact takes place when one of the collectors is plastically capturing a target. Missel and Mortari (2013) have derived the mathematical models based on angular momentum conservation for these four configurations by considering the sling-sat as a 2-mass system. To further improve this model, a mathe-

mathematical model of a 5-mass system has been established (Missel and Mortari, 2011).

### ADHESIVE METHOD

The adhesive method is proposed by Astro Scale in Singapore and is a multiple targets removal method as well. A de-orbiting kit (called 'Boy') equipped with a propulsion system can be released from a carrier (called 'Mothership'). The boy adheres onto a tumbling space debris then removes it from its original orbit. Six boys are loaded on the mothership. The mothership sails to a different space debris object and releases one boy each time, so that multiple targets can be de-orbited in one mission. On the front part of the boy, a plate with silicon adhesive compound is installed through a universal joint which contains 20 degrees allowance to passively adjust the adhesive plate onto a flat surface of a target. Using this method, a target whose tumbling rate is below 1-2 °/s can be successfully captured. The boy is able to approach the tumbling target in two ways: along its tumbling axis or orthogonal to the tumbling axis. No matter which way is selected, attitude synchronization is an indispensable step before adhering onto a target (Okada, 2014). Jet Propulsion Laboratory (JPL) has also developed a gecko-inspired adhesive grappling tool that uses microscopic angled hairs to stick to the surface of a target. The adhesion is based on van der Waals forces and can be turned ON and OFF by controlling the loading direction (Aaron, 2015). The gripper's functionality has been demonstrated by zero gravity experiments and air bearing floor experiments (Jiang et al., 2015).

#### 2.4.4. CONTACTLESS REMOVAL METHODS

Comparing to contact-based removal methods, no direct contact between the chaser satellite and the target is involved in contactless removal methods. The most relevant contactless removal methods (Fig. 2.11) are: an artificial atmosphere influence method, a laser system and an ion beam shepherd. The general principle of all these methods is to decrease the velocity of the space debris object by ejecting some substances in their trajectories thus lowering their altitudes. However, it always takes a long time to remove a target.

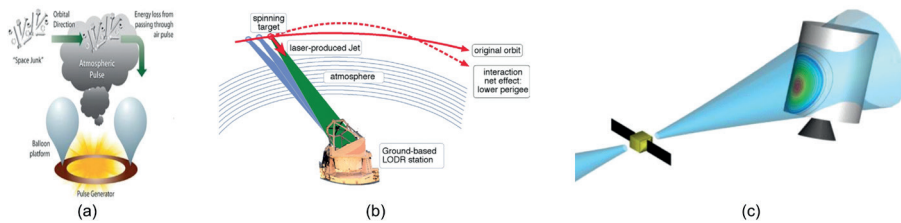


Figure 2.11: Contactless removal methods. (a) Artificial atmosphere influence . (b) Laser system . (c) Ion beam shepherd.

#### ARTIFICIAL ATMOSPHERE INFLUENCE

The principle of the artificial atmosphere influence method is to propel atmospheric particles in the path of a debris object. As a result, the velocity of the debris is decreased

and its altitude is lowered. Types of atmosphere particles can be gaseous plumes or a vortex whose ejecting direction is orthogonal to the path of the debris (Gregory and Mergen, 2014). Kofford (2011) designed an artificial atmosphere delivery system composed by an ignition device and combustible propellant. Another analogous concept is to create a transient gaseous cloud which has sufficient density in front of a debris to help it re-enter (Dunn, 2014). The Artificial atmosphere influence is a green removal method since the gaseous plume does not harm operational satellites and it will eventually fall back to the atmosphere. This technique is considered as one of the most promising removal methods due to these strengths (Kaushik et al., 2014).

#### LASER SYSTEM

The laser system is available for removal of both large and small space debris objects. A pulsed laser beam shoots onto a space debris to decrease its velocity and lower its altitude. However, the risk of new debris generation is significant using a laser system. As early as 1996, Phipps stated that a space debris object can be removed by a 20 kW, 530 nm, Earth-based, repetitively pulsed laser. The system is called 'ORION' which consists of an Earth-based laser system to generate a powerful laser beam and a high-resolution detection system to chase targets with a diameter of 1 cm below 500 km. According to Phipps et al. (1996), this system is able to remove all space debris whose size is larger than 1 cm and whose mass is less than 500 kg below 1000 km altitude in 4 years. An updated system called Laser Orbital Debris Removal (LODR) at either pole would be able to de-orbit the Envisat satellite by 40 km every 8 weeks. This laser system can be located at ground-based equator, ground-based polar region or on board (Phipps, 2014).

#### ION BEAM SHEPHERD

Ion Beam Shepherd (IBS) is a concept of ejecting a highly collimated neutral plasma beam onto a debris object thus lowering its altitude. Bombardelli and Pelaez (2011) have optimized the system by minimizing the mass of a shepherd. A distance between a chaser satellite and a target stays at 10-20 meters. As a result, a second propulsion system is needed to keep this distance. Merino et al. (2013) have developed a simulator called Ion Beam Interaction Simulator (IBIS) to analyze, test and validate the conceptual design of the IBS. In addition, it is able to evaluate the performance of the system, optimize the designed parameters and make de-orbiting strategies. They also analyzed the requirements of the propulsion system, identified the plasma beam characterization and investigated the momentum transmission to the space debris during the interaction between the plasma and target (Merino et al., 2011). Besides the space debris in LEO region, Kitamura et al. (2014) suggested using IBS to re-orbit space debris in GEO. Through their numerical analysis and some experimental facilitation, they concluded that six debris objects in GEO can be removed during 170 days using a 2500 kg shepherd.

To clarify the characteristics of removal methods and draw a comparison between them, their respective examples, original sources, advantages and drawbacks are summarized in Table 2.3.

#### 2.4.5. TAILORED ADR METHODS

Various space debris capturing and removal methods have been proposed and investigated so far. The most appropriate capturing and removal method for each debris object

Table 2.3: Overview of relevant removal techniques

Removal Methods	Advantages	Drawbacks	Examples	Sources
<b>Drag Augmentation System</b>	1.Allows a large distance; 2.Compatible with different sizes of debris.	1.Risk of breakup; 2.Less efficient.	Foam	ESA
			Inflated	GAC
			Fiber-based	US Patent
<b>Electro-dynamic Tether</b>	1.No need for propulsion system; 2.High TRL.	1.Capture needed; 2.Unavailable in GEO.	EDT	JAXA
			Slingshots	USA
<b>Contact Removal</b>	1.Multiple targets removed; 2.Short working period.	1.Rendezvous needed; 2.Complex control system.	Adhesive Method	Astroscale
<b>Contact-less Removal</b>	1.Allows a long distance; 2.Compatible with different sizes of debris.	1.Less efficient; 2.Partially available in GEO.	Artificial atmosphere	US Patent
			Laser System	LODR
			Ion Beam Shepherd	ESA

will be different due to the different non-cooperative levels of each debris object. As a result, the tailored associated capturing and removal methods for each category of space debris object need to be developed.

Various aspects should be concentrated when dealing with space debris objects in different categories. For example, when a rocket upper stage is selected as a target, capturing should be performed with care due to the risk of explosion. Therefore, a harpoon might not be a good choice used to capture such objects. Robotic arm with a probe as the end effector or net capturing method are more appropriate capturing methods for a rocket upper stage removal. The size of a fragment can range from several centimeters to meters. Also, it is fully non-cooperative. A fragment can neither provide a docking interface for capturing nor physical properties for further control. Therefore, for the large size fragments, net capturing method can be considered due to its compatibility to different shapes and sizes of targets. For the small size fragments, it is wise to remove them using removal methods without capturing. When it comes to a non-operational satellite, all capturing methods are applicable.

Some removal methods can only be performed after capturing, e.g., to transport a target to a graveyard orbit. On the contrary, some removal methods avoid capturing at all, such as contactless methods. The DAS and contactless methods are applicable for removal of all types of space debris objects in LEO. Slingshot methods are more promising for removing small size fragments since Slingshots are designed to remove multiple small targets with one device. Moreover, the fragments generated from explosions or collisions always have similar orbital parameters. Therefore, it saves energy for the Slingshots after capturing a space debris object and ejecting it towards the Earth then slide to another space debris object applying the momentum generated from the ejection (Missel and Mortari, 2013). Adhesive method is more appropriate for removing a non-operational satellite or a rocket upper stage since the adhesive plate is designed to attach onto a relatively flat surface of a target which is hardly found on fragments (Okada, 2014). For space debris objects in different categories, the tailored associated capturing and removals methods are provided in Table 2.4.

Among all capturing methods, the net capturing method is found to be compatible with different sizes, shapes, types and orbits of space debris. Moreover, it avoids

Table 2.4: Tailored Associated Capturing and Removal Methods

Categories	Capturing Methods	Removal Methods without Capturing
<b>Non-operational satellites</b>	All	DAS/Contactless/Adhesive
<b>Rocket upper stages</b>	Robotic Arm/Tentacles/Net/ Gripper	DAS/Contactless/Adhesive
<b>Fragments</b>	Net capturing	DAS/Contactless/Slingshots

the close-range rendezvous and docking with the target. Additionally, the net is flexible, lightweight and cost efficient. Therefore, the net capturing method, as one of the most promising ADR methods, will be discussed throughout this thesis.

## 2.5. SUMMARY

Many enabling techniques for ADR have been investigated in the past two decades. This chapter first classified the space debris into three categories: non-operational satellites, rocket upper stages and fragments. To provide a clear impression of the existing techniques for ADR, frameworks of methods for space debris capturing and removal have been developed, respectively. The advantages and drawbacks of the most relevant capturing and removal methods have been addressed as well. Moreover, a comparison between the existing technologies on ADR has been drawn. Finally, a tailored associated capturing and removal method for each category of space debris has been provided to facilitate decision-making through these capturing and removal methods. Net capturing method is considered as a promising method among others. An extensive study on the dynamics of net capturing is, therefore, performed in the following chapters.



# 3

## DEPLOYMENT DYNAMICS OF A NET

---

Parts of this chapter have been published in M. Shan, J. Guo, E. Gill, *Deployment dynamics of tethered-net for space debris removal*, *Acta Astronautica* **132**, 293-302 (2017) and M. Shan, J. Guo, E. Gill, W. Golebiowski, *Validation of Space Net Deployment Modeling Methods Using Parabolic Flight Experiment* *Journal of Guidance, Control and Dynamics* **1**, 1 (2017).

### 3.1. INTRODUCTION

Operational space missions in Low-Earth Orbits (LEO), vital for key services of social relevance, are more and more endangered by millions of space debris objects. As discussed in the previous chapter, many space debris capturing and removal methods have been investigated to mitigate this situation (Shan et al., 2016), such as the robotic arm removal method (Reintsema et al., 2010), the tethered space robot (Huang et al., 2016b), the harpoon (Reed et al., 2012) and the manoeuvrable tether-net space robot system (Huang et al., 2016a). Among these methods, the net capturing method is regarded as one of the most promising capturing methods due to its multiple advantages: it allows a large distance between the chaser satellite and the target, such that close range rendezvous and docking are not mandatory; it is capable to capture various dimensions and shapes of space debris objects; and, finally, the net is flexible, lightweight and cost efficient. The net capture mechanism consists of four flying weights in each corner of a net. The flying weight is called "bullet", shot by a spring system, named "net gun". These four bullets help expand the large net thus wrapping a target. Figure 3.1 shows the conceptual diagram of capturing a non-operational satellite in the initial deployment phase.

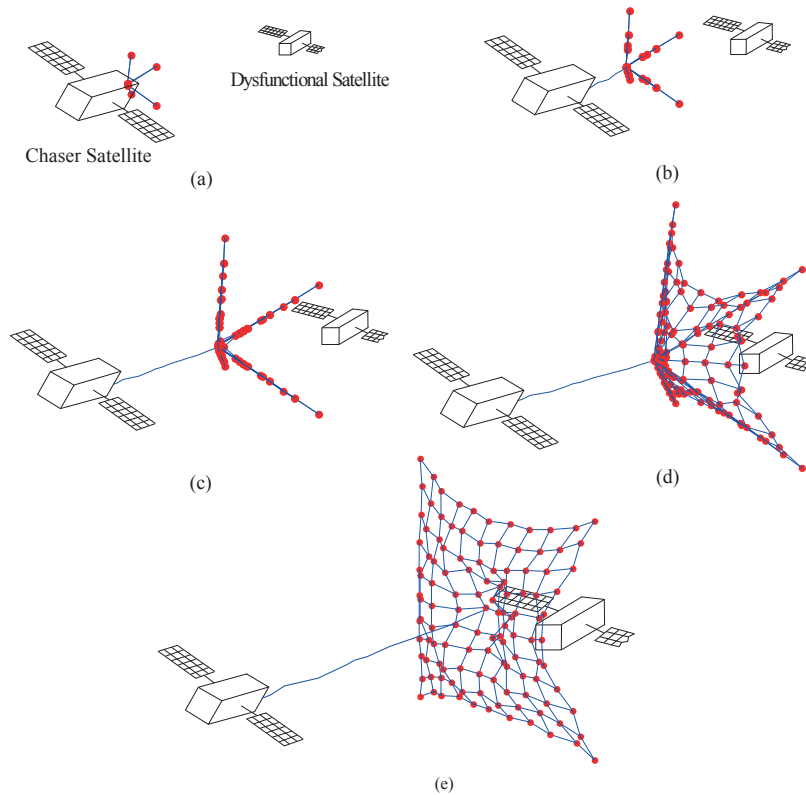


Figure 3.1: Conceptual diagram of initial deployment phase of the net capturing

Many institutes and universities have been studying the net capturing method. ESA has sponsored the Robotic Geostationary Orbit Restorer (ROGER) whose objective is to transport a target into a graveyard orbit using a net (Bischof et al., 2004). The feasibility of the net capturing method has been analyzed based on this concept. Simulations with different parameters such as relative position, relative rotation, tether length and tether stiffness have been performed to investigate the dynamics of a net (Billot et al., 2014). In the project Debris Collecting Net (D-CoNe) (Lavagna et al., 2012), the net is modeled as a lumped mass system, which is the most commonly used modeling method for a tethered-net. In the lumped-mass system, a tether is usually assumed to be formed by several small segments. Since a net is comprised of many small square meshes, the knot at the intersection of the cables is simplified as a mass point, and the tethers between these knots are regarded as spring-damping elements. Many simulations using a mass-spring model for a space tethered-net have been carried out. Botta et al. (2016b) have analyzed the effect of bending stiffness of cables on the deployment dynamics and capturing motion using a net. Benvenuto et al. (2016) focus on the overall dynamics of the net and interface between the net and the free-tumbling object during the disposal maneuvers. Parabolic flight experiments performed by a Spanish company called GMV have validated the simulation results of net deployment and capturing (Lorenzo et al., 2015). Apart from the mass-spring model, Liu et al. (2014) have provided a modeling method for tethered-net based on the absolute nodal coordinate formulation (ANCF) which has been initially proposed by Shabana and has been utilized in solving large displacement and deformation problems (Shabana, 1997). However, both models are not verified sufficiently, and the net deployment dynamics were not further investigated in above research. Therefore, the net deployment dynamics is investigated in this chapter, and models for a net based on the mass-spring and the ANCF model are established, further discussed and compared. Moreover, criteria to evaluate a tethered-net deployment, e.g., maximum deployed area, deployment time, travelling distance and effective period, have been identified, defined and investigated. Their dependencies on the initial deployment conditions are analyzed based on the mass-spring model. A comprehensive study on modeling of a net based on ANCF is provided, and the simulation results are compared with that based on the mass-spring model. The mass-spring model and ANCF model are finally cross-verified and validated by data from a parabolic flight experiment (Gołębowski et al., 2015b).

## 3.2. CHARACTERISTICS OF A NET

### 3.2.1. PHYSICAL PROPERTIES OF A NET

The physical properties of a net, such as strength and stiffness of the net material, are key features for a space net system. They will directly impact in the effect of capturing and removal, e.g., less strong net material might be cut by sharp parts on a space debris object and, consequently, cause a failure of the mission. Since the net material is required to be lightweight, strong and flexible in bending, Honeywell Spectra, Kevlar, Zylon and Carbon fiber are possible material candidates. According to numerical simulations of net casting and disposal strategies, a Kevlar net with the cable diameter of 1 mm is able to carry out all the required operations with target space debris object up to

Table 3.1: Physical properties of net material candidates

Parameter	Honeywell Spectra	Kevlar	Zylon	Carbon fiber
Young's Modulus $E$ , GPa	79	130	180	230
Elongation at break $\epsilon$ , %	3.6	2.8	3.5	1.5
Density $\rho$ , g/cm <sup>3</sup>	0.97	1.44	1.54	1.76
Tensile Strength $\sigma$ , GPa	2.6	3.6	5.8	3.5

## 3

1000 kg without failures (Benvenuto and Carta, 2013). However, the stiffness of material has an influence on the flexibility of the net. To study how different stiffness affects the dynamic characteristics of a net, these four materials are applied and compared. Table 3.1 shows the physical properties of these four materials. In addition, based on the previous studies on space webs, the square web with a square mesh is suggested since it revealed to be the optimum both on manufacturing and stiffness (Tibert and Gärdsback, 2006). Therefore, the remainder of this thesis will only be concerned with the square net with a square mesh.

### 3.2.2. FOLDING SCHEME

A fundamental characteristic for a net and its successful deployment is that it has to be easily folded in a canister. Many folding schemes, such as Miura-Ori folding scheme (Miura, 1985) and Hub-wrapping folding scheme (Furuya et al., 2005) for various solar sails have been proposed. A two-step folding sequence has also been provided by Gärdsback and Tibert (Gärdsback and Tibert, 2009). However, this two-step folding sequence only applies for a spin-deployed space web with a membrane installed on it. For a net to be used for space debris removal, consideration is only taken in the folding of cables. Here, we propose a new folding scheme called 'inwards-folding scheme'. To clarify the folding scheme of a net, Fig. 3.2 shows the folding sequence with four units of square meshes. Apparently, it also applies for odd number of units. Using this folding method, each cable element is folded inwards at its center point, and four bullets are successively coming close. In this way, it turns a net into a folded bundle of cables under a specific configuration. This folding scheme also simplifies the modeling because the numbering of each cable and each node is following a specific formulation, either arithmetic sequence or geometric sequence as shown in Fig. 3.3.

### 3.2.3. OUTPUT AND INPUT PARAMETERS

Once a net is shot, four bullets on the corners of the net help deploy the net. The net's mouth will open to a maximum area then start to close. Assume a net is  $10 \times 10$  meshed and the mesh length is 1 m. Therefore, its designed maximum area is  $100 \text{ m}^2$ . Fig. 3.4 shows the net area changing with time during the net deployment. To describe the dynamic characteristics of a net during deploying, four criteria to evaluate a net are defined with the help of (Yu et al., 2010).

- **Maximum Area** The maximum area of a net is defined as the largest area the net is able to reach during the deployment. The deployment area is defined as the

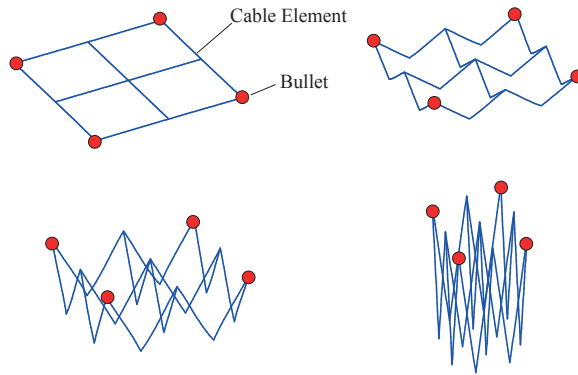


Figure 3.2: Folding sequence

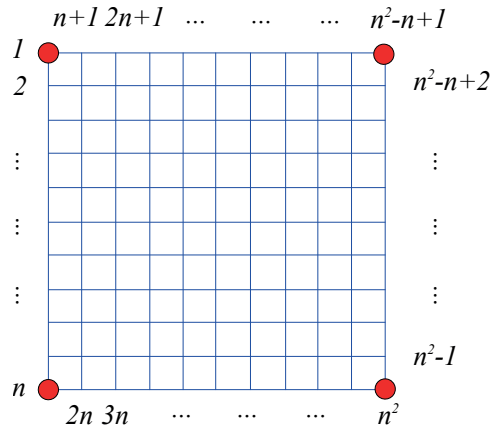


Figure 3.3: Labeling of each node

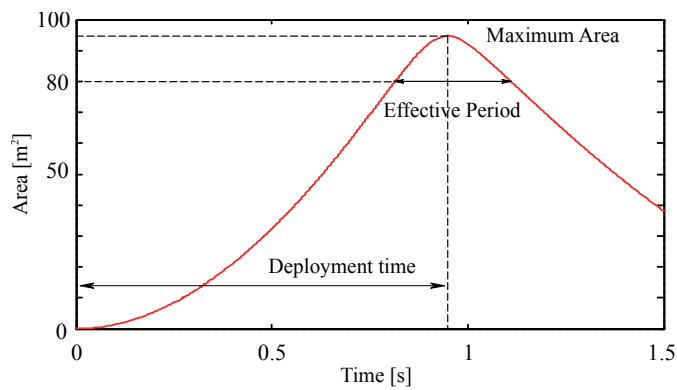


Figure 3.4: Three parameters are shown during the net deployment

projection area composed by four bullets.

- **Deployment Time** Deployment time is the period starting from the time of shooting to when the net reaches its maximum area.
- **Travelling Distance** Travelling distance is the distance the center of mass of a net travels during the deployment time.
- **Effective Period** The period in which the area of a net is beyond 80% of its designed maximum area (We assume that when the net is deployed up to 80 % of its designed maximum area, it is capable to capture a target effectively).

## 3

These four criteria determine the scope of a space debris removal mission using a net. The maximum area a net deploys determines the maximum volume of a space debris object the net is capable of capturing; the distance a chaser satellite should keep with the target in close rendezvous phase depends on the net's travelling distance. In addition, the deployment time determines how efficient the deployment is and the effective period describes how long the net can stay in an effective configuration. Therefore, these four parameters are most critical parameters which characterize the net capturing method.

However, these four critical parameters depend on several initial input parameters, such as the shooting velocity of the bullets, the shooting angle, the bullet mass and the material of a net. The shooting angle  $\theta$  is defined as the angle between the direction of the shooting velocity and the travelling direction of the net, which is shown in Fig. 3.5. The travelling direction of a net is defined as the direction the mass center of the net travels. The initial shooting angle for each bullet is set the same due to the symmetric configuration of the net.

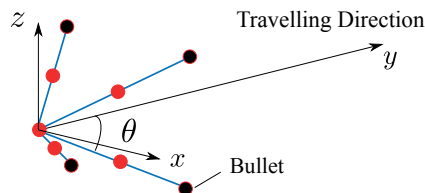


Figure 3.5: Definition of the shooting angle

During the net deployment, the bullets are first shot by the shooting mechanism with the same absolute velocity along each shooting angle  $\theta$ . The rest part of the net will follow the bullet to deploy. The velocities of the bullets will be decreased when the cables are elongated and tensioned. Then the bullets will eventually stop expanding the net until the net reaches its maximum area, after which the net starts to shrink, i.e., the bullets start to travel back towards the center of the net. The motion after shrinkage is not considered in deployment dynamics since a space debris object is supposed to be captured before the net shrinks to a certain configuration. This chapter investigates how the initial parameters affect the dynamic characteristics of a net.

### 3.3. DYNAMIC MODELS OF A NET

#### 3.3.1. MASS-SPRING MODEL

A mass-spring model approximates a flexible cable as a series of mass points connected by mass-less spring-damper elements (Fig. 3.6). As noted earlier, a net for space debris removal is weaved as many square meshes by those thin, flexible and well-knit cables. The knots at the intersections of the net are modeled as mass points, and the cables between them as massless spring-damper elements. Assuming the net material is homogeneous isotropic linear material, the axial stiffness of the cable  $k$  is defined as

$$k = \frac{EA}{l_0}, \quad (3.1)$$

where  $E$  is the elastic Young's modulus of the cable material, and  $A$  and  $l_0$  are the cross section and the initial unstretched length of the mesh cable, respectively.

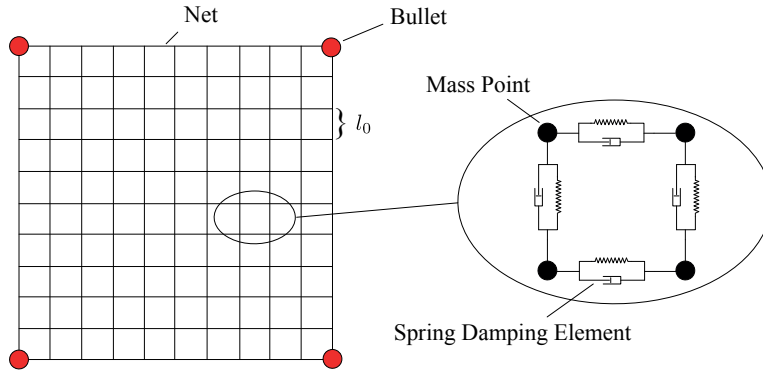


Figure 3.6: Mesh modeling

The mass lumped on each node depends on the number and the cross area of adjacent cables with which is connected. The lumped mass is modeled as the sum of half masses of the cables connected to the node. Thus, the point mass on four edges of the net is different from the inside ones. The mass at  $i$ th node can be expressed as

$$m_i = \begin{cases} m_b & i \text{ at four corners,} \\ 3/2\rho Al_0 & i \text{ at four edges but corners,} \\ 2\rho Al_0 & i \text{ is inside the net.} \end{cases} \quad (3.2)$$

where  $m_b$  is the bullet mass and  $\rho$  is the density of the cable.

According to the nature of the cable material, cable elements are not able to withstand compression and a tension force will only be generated when the cables are elongated. The linear Kelvin-Voigt model is the most efficient and commonly used method to characterize the tension force generated in a cable. Based on the linear Kelvin-Voigt model, the tension force  $f_{ij}$  between nodes  $i$  and  $j$  can be expressed as

$$\mathbf{f}_{ij} = \begin{cases} f_{ij} \hat{\mathbf{r}}_{ij} & r_{ij} > l_0 \text{ and } f_{ij} < 0, \\ 0 & r_{ij} \leq l_0 \text{ or } f_{ij} > 0, \end{cases} \quad (3.3)$$

where  $f_{ij} = -k(r_{ij} - l_0) - c\dot{r}_{ij}$ . In this equation,  $r_{ij}$  and  $\dot{r}_{ij}$  are the distance and the relative velocity between the  $i$ th and  $j$ th node. Further,  $\hat{r}_{ij}$  represents the unit direction vector along the  $i$ th and  $j$ th node expressed in the Local Vertical-Local Horizontal (LVLH) reference frame (Fig. 3.7). The damping coefficient  $c$  of the cable material depends on the cable mass and cable stiffness with its damping ratio  $\xi$ , according to

$$c_i = 2\xi\sqrt{m_i k}. \quad (3.4)$$

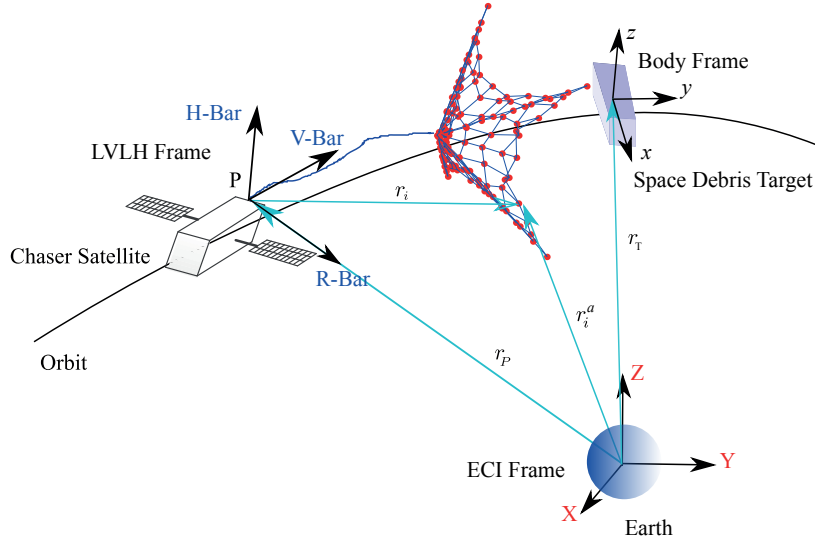


Figure 3.7: Chaser approaching the target along the V-Bar

The chaser satellite is assumed to be approached along-track by the target before shooting the net (Fig. 3.7). The absolute position of mass points in the Earth Centered Inertial (ECI) reference frame is expressed as  $\mathbf{r}_i^e = \mathbf{r}_p + \mathbf{R}^o \mathbf{r}_i$ , in which  $\mathbf{r}_i^e$  is the absolute position vector of the  $i$ th node in the ECI frame, and  $\mathbf{R}^o$  is the rotation matrix that transforms the position vector  $\mathbf{r}_i$  from the LVLH to the ECI frame. With such a model, the dynamic equations of motion for the entire net can be discretized as

$$m_i \frac{d\dot{\mathbf{r}}_i^e}{dt} = \sum_{j=1}^{N_i} \mathbf{R}^o \mathbf{f}_{ij} + \sum_{s=1}^{M_i} \mathbf{f}_{is}^e + \mathbf{g}_i, \quad (3.5)$$

where  $N_i$  is the number of adjacent cables connected to the  $i$ th node,  $\mathbf{f}_{ij}$  is the force on the  $i$ th node generated by the  $j$ th cable connected to it,  $M_i$  is the number of external forces on the  $i$ th node, and  $\mathbf{f}_{is}^e$  is the sum of external forces, e.g., aerodynamic drag, solar radiation pressure and other perturbations. The micro-gravitational force  $\mathbf{g}_i$  on the  $i$ th node is given by

$$\mathbf{g}_i = -\frac{GMm_i \mathbf{r}_i^a}{|\mathbf{r}_i^a|^3}, \quad (3.6)$$

in which  $GM$  is the gravitational coefficient of the Earth.

### 3.3.2. ANCF MODEL

ANCF method originates from the finite element method (FEM). In the classical FEM, infinitesimal or finite rotations are used as nodal coordinates. Assumptions of small deformations and rotations are however made, which causes that the model can not accurately describe the dynamic characteristics of a highly flexible system. In ANCF method, which is initially proposed by Shabana, and utilized in solving large displacement and deformation problems, absolute positions and the gradients of the positions act as the element nodal coordinates to describe the configuration of a flexible system (Shabana, 1997). The nodal coordinates of the elements in ANCF are defined in a global inertial coordinate frame. As a result, coordinate transformations are not necessary when deriving the dynamic equations of motion. Moreover, the gradients of the absolute positions, hereinafter named as the global slopes, instead of infinitesimal or finite rotations are used to describe the orientation of the elements. This important feature leads to a constant mass matrix in ANCF and consequently no centrifugal and Coriolis forces are involved in the derivation of the dynamic equations. On the contrary, the expressions of the elastic forces in ANCF are non-linear and coordinate- or time-dependent. Several simplified models of elastic forces for beam elements have been derived by Berzeri and Shabana (2000). Gerstmayr and Shabana (2006) have developed a low-order cable element, in which it has half degrees of freedom of a fully parameterized beam element. In this cable element, only the deformation along the longitudinal direction (the center line of the cable) is considered which is able to accurately describe the nature of a cable (Gerstmayr and Shabana, 2006). Since four bullets are attached to the four corners of the net to help it extend, a net system becomes a rigid-flexible coupled system. In this section, the dynamic equations of motion for the rigid-flexible coupled system for a net are derived.

For a net which is weaved by cables (as shown in Fig. 3.8), one cable element contains two nodes and the arbitrary position in a cable element can be expressed as

$$\mathbf{r} = \mathbf{S}\mathbf{e} = [S_1\mathbf{I}, S_2\mathbf{I}, S_3\mathbf{I}, S_4\mathbf{I}][\mathbf{e}_1, \mathbf{e}_2]^T, \quad (3.7)$$

where  $\mathbf{S}$  is the global shape function,  $\mathbf{I}$  is a  $3 \times 3$  identity matrix,  $\mathbf{e}_i$  ( $i = 1, 2$ ) is the absolute nodal coordinates at  $x = 0$  and  $x = l_0$  where  $x$  is the local coordinate of arbitrary point on the element and  $l_0$  is the initial length of the cable element.

$$\mathbf{e}_i = [\mathbf{r}_i, \mathbf{r}_{ix}]; \mathbf{r}_{ix} = \frac{\partial \mathbf{r}_i}{\partial x}, \quad (3.8)$$

where  $\mathbf{r}_i$  is the global displacement and  $\mathbf{r}_{ix}$  is the global slope of the element. The shape function  $S_i$  is defined as

$$S_1 = 1 - 3\xi^2 + 2\xi^3, S_2 = l_0(\xi - 2\xi^2 + \xi^3), S_3 = 3\xi^2 - 2\xi^3, S_4 = l_0(-\xi^2 + \xi^3), \quad (3.9)$$

where  $\xi = x/l_0$ . In a gradient deficient cable element,  $y$  and  $z$  dimensions are not taken into account due to the small magnitude in these two directions and this is the main difference between a cable element and a beam element.

The constant mass matrix  $\mathbf{M}_i$  can be derived by evaluating the kinetic energy expression. The kinetic energy of an element can be expressed as

$$T_i = \frac{1}{2} \int_V \rho \dot{\mathbf{r}}_i^T \dot{\mathbf{r}}_i dV = \frac{1}{2} \dot{\mathbf{e}}_i^T \mathbf{M}_i \dot{\mathbf{e}}_i, \quad (3.10)$$

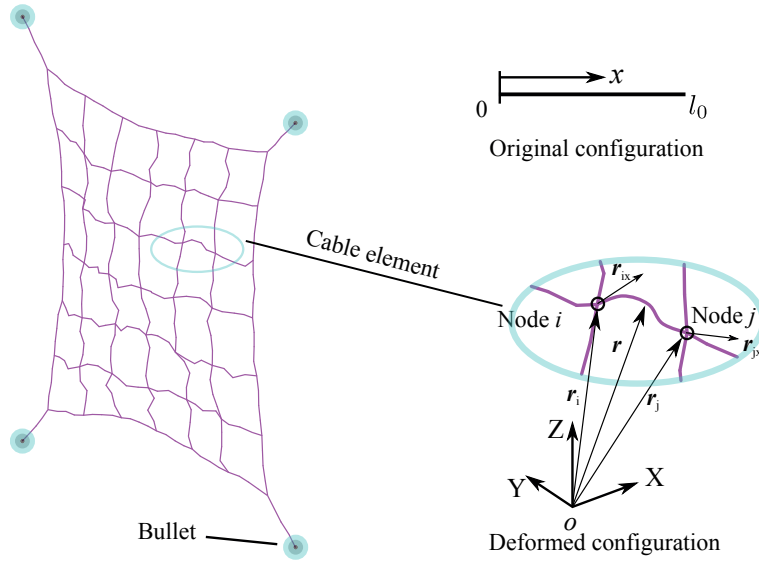


Figure 3.8: Cable element described in a net.

where  $\rho$  is the density of the element material,  $\dot{\mathbf{r}}_i$  is the velocity of the  $i$ th element. The constant mass matrix  $\mathbf{M}_i$  is consequently written as

$$\mathbf{M}_i = \int_V \rho \mathbf{S}^T \mathbf{S} dV. \quad (3.11)$$

The elastic forces of a cable element can be derived from the elastic energy. The energy of a deformed cable element contains two parts: the strain energy  $U_l$  due to longitudinal deformation and the strain energy  $U_b$  due to bending. They can be expressed as

$$U_l = \frac{1}{2} \int_0^{l_0} EA \varepsilon_l^2 dx; \quad U_b = \frac{1}{2} \int_0^{l_0} EI \kappa^2 dx; \quad (3.12)$$

where the axial strain  $\varepsilon_l$  can be expressed based on Cauchy-Green longitudinal strain as

$$\varepsilon_l = \frac{1}{2} (\mathbf{r}'^T \mathbf{r}' - 1). \quad (3.13)$$

and  $I$  is the area moment of inertia of the cable cross-section,  $\kappa$  represents the curvature of the cable that can be derived from the Serret-Frenet frame (Gerstmayr and Shabana, 2006).

Using the expression of the strain energy (Eq. 3.12), one obtains the vector of the elastic forces

$$\mathbf{f}_{ki} = \left( \frac{\partial U}{\partial \mathbf{e}_i} \right)^T = \mathbf{K}_i \mathbf{e}_i \quad (3.14)$$

where  $U = U_l + U_b$ , and  $\mathbf{K}_i$  is the nonlinear stiffness matrix of the element  $i$  which is difficult to calculate. In order to minimize the number of mathematical operations in

the computer implementation, Gaussian quadrature was used for the integration of the non-rational strain energy expressions ( $U_l$ ,  $U_b$ ) to approximate the elastic forces. Other models for evaluating the elastic forces can be found in (Berzeri and Shabana, 2000). However, in this thesis, only the elastic forces due to longitudinal deformation are taken into account because of the flexibility in bending of the cable material.

In the net model, each cable element is connected with other cable elements end by end under a specific configuration which has been introduced in Section 3.2.2. Moreover, the cable elements at four corners of the net are also connected with the rigid bodies (bullets) under constraint conditions. The constraint equations of connected absolute nodal coordinates and constraint equations of bullets are expressed as

$$\mathbf{e}_s^i - \mathbf{e}_e^j = 0, \quad (3.15a)$$

$$\mathbf{q}_b - \mathbf{S}\mathbf{e}_c = 0, \quad (3.15b)$$

in which  $\mathbf{e}_s^i$  is the vector of absolute nodal coordinates of the start of element  $i$  as shown in Fig. 3.9, and  $\mathbf{e}_e^j$  is the vector of the end of element  $j$  of the connected elements  $i$  and  $j$ , and  $\mathbf{q}_b$  represents the vector of the coordinates of the bullets and  $\mathbf{e}_c$  is the vector of absolute nodal coordinates connected with the bullets at four corners of the net.

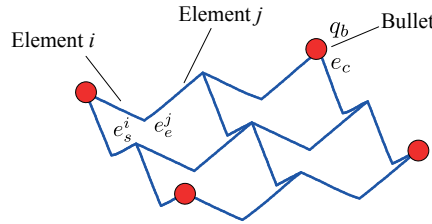


Figure 3.9: Constraints between absolute nodal coordinates.

Using the principle of virtual power and introducing Lagrange multipliers (De Jalon and Bayo, 2012), one can derive the system equations of motion for the tethered-net as

$$\begin{bmatrix} \mathbf{M}_b & \mathbf{0} & \mathbf{0} & \Phi_{q_b}^T \\ \mathbf{0} & \mathbf{M}_e & \Phi_e^T & \Phi_{e_c}^T \\ \mathbf{0} & \Phi_e & \mathbf{0} & \mathbf{0} \\ \Phi_{q_b} & \Phi_{e_c} & \mathbf{0} & \mathbf{0} \end{bmatrix} \begin{bmatrix} \ddot{\mathbf{q}}_b \\ \ddot{\mathbf{e}} \\ \lambda_1 \\ \lambda_2 \end{bmatrix} = \begin{bmatrix} \mathbf{Q}_b \\ \mathbf{Q}_e \\ \mathbf{Q}_1 \\ \mathbf{Q}_2 \end{bmatrix}, \quad (3.16)$$

where  $\mathbf{M}_b$  and  $\mathbf{Q}_b$  are the mass matrix and the external forces, e.g., microgravity, aerodynamic drag and other perturbations of the rigid bodies, namely the bullet masses, respectively;  $\mathbf{M}_e$  and  $\mathbf{Q}_e$  are the constant ANCF mass matrix and the generalized forces associated with absolute nodal coordinates  $\mathbf{e}$ , respectively. In this case,  $\mathbf{Q}_e$  is the external forces plus the elastic forces. Here,  $\lambda_1$  and  $\lambda_2$  represent the Lagrange multipliers;  $\Phi_e$  is the Jacobian matrix of the constraint equations (Eq. 3.15a) associated with the absolute nodal coordinates;  $\Phi_{q_b}$  and  $\Phi_{e_c}$  are the Jacobian matrices of the constraint equations (Eq. 3.15b) associated with the bullet masses and the cable elements;  $\mathbf{Q}_1$  and  $\mathbf{Q}_2$  are quadratic velocity vectors derived by differentiating the constraint equations (Eq. 3.15) twice with respect to time.

Table 3.2: Initial Input Parameters for Simulations

Parameter	Value
Cable diameter $d$ , [mm]	1
Mesh length $l_0$ , [m]	1
Bullet mass $m_b$ , [kg]	$1 \times 4$
Net mass $m_n$ , [kg]	0.2
Shooting velocity $v$ , [m/s]	10
Shooting angle $\theta$ , [°]	55
Net size $A$ , [m <sup>2</sup> ]	$10 \times 10$
Damping ratio $\xi$ , [-]	0.1

### 3.4. SENSITIVITY ANALYSIS

#### 3.4.1. SIMULATION

As introduced in Section 3.2.3, the output parameters such as the maximum area, the deployment time, the travelling distance and the effective period are four most critical parameters for the net deployment. Different initial parameters, such as the initial bullet velocity, the shooting angle, the bullet mass and the net material affect these output parameters in a different way. Thus, it is necessary to investigate the dependency of these initial parameters on these output parameters, respectively. To study how the initial conditions influence the dynamic characteristics of a net, a series of simulations based on the mass-spring model were performed and analyzed. The characteristics of the net materials applied in the simulations are given in Table 3.1. The initial input parameters for the simulations are given in Table 3.2.

#### 3.4.2. INVESTIGATION ON NET CHARACTERISTICS

A univariate analysis is applied to study the influence the different initial input parameters on four critical output parameters. Firstly, the initial bullet velocity is changed from 10 to 28 m/s, while the bullet mass and shooting angle are fixed at  $m_b = 1\text{ kg}$ ,  $\theta = 55^\circ$ . Simulations with four materials were carried out using the mass-spring model and the result is shown in Fig. 3.10. We notice that the maximum deployed area is barely affected by the initial bullet velocity, and the net with the less stiff material is able to extend to a larger area. While the deployment time is decreasing w.r.t. the increasing initial bullet velocity, i.e., the higher the initial bullet velocity, the more efficient the capture is. On the other hand, as the initial bullet velocity is increasing, the effective period for capturing is reduced, and the travelling distance is rarely changing. The reason for this slight variation is due to the fact that the travelling distance depends both on the initial bullet velocity and the deployment time that is changing in the other way around.

In the second case, we use  $v = 10\text{ m/s}$  and  $m_b = 1\text{ kg}$ , and the shooting angle  $\theta$  changes from  $35^\circ$  to  $70^\circ$ . It is shown in Fig. 3.11 that larger shooting angles also help contribute to a larger net area and renders a more efficient capture. Also, the travelling distance is significantly decreased w.r.t. the increasing shooting angles. This because the velocity component in the travelling direction is decreased w.r.t. the increasing shooting

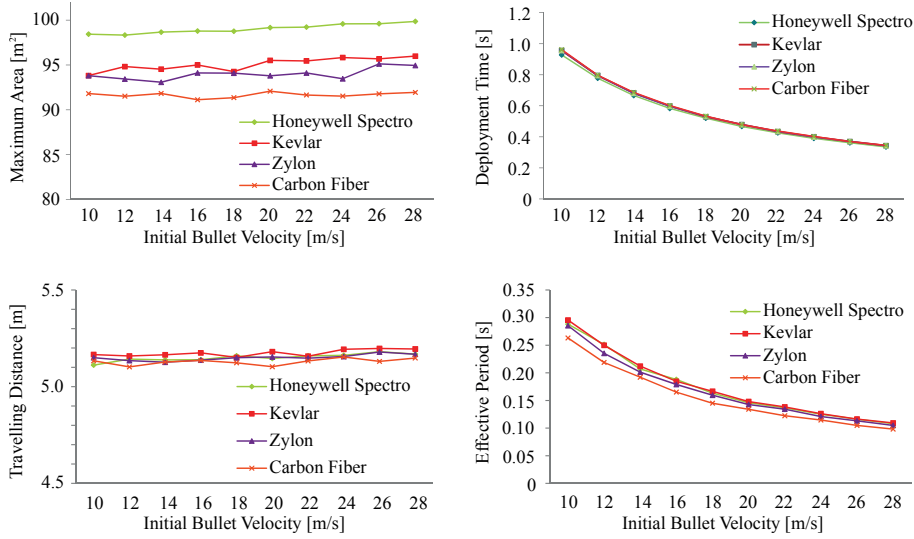


Figure 3.10: Dynamic net parameters changing with different initial bullet velocities (By MS model).

angels.

In the third case, we use  $v = 10\text{m/s}$ , and  $\theta = 55^\circ$ , and the bullet mass changes from 0.4 to 2.2 kg. From Fig. 3.12, it is concluded that the larger bullet mass dramatically help deploy the net but barely affect the deployment time. Moreover, the travelling distance and the effective period share a similar trend w.r.t. the increasing bullet mass.

### 3.4.3. DEPENDENCY ANALYSIS

Following this analysis, it is concluded that the bullet mass and the shooting angle are key parameters influencing the net deploying area, and the shooting angle also influences the travelling distance dramatically. Moreover, the effective period is primarily influenced by the shooting velocity. To clarify the sensitivity of the output parameters on different initial input parameters, Table 3.3 shows the dependency quantitatively. The dependency on input parameters  $D_{ij}$  can be described as

$$D_{ij} = \frac{\delta O_i}{\delta I_j}, \tag{3.17}$$

where  $\delta O_i$  and  $\delta I_j$  are the relative deviation of the  $i$ th output parameter and  $j$ th input parameter, respectively. They can be expressed as

$$\delta O_i = \frac{\Delta O_i}{O_i}, \delta I_j = \frac{\Delta I_j}{I_j}, \tag{3.18}$$

where  $\Delta O_i$  and  $\Delta I_j$  are the absolute deviation of the  $i$ th output parameter and  $j$ th input parameter, respectively. From Eq. 3.18, it is known that output parameters' dependency also relies on the starting value of the input parameters. Table 3.3 displays the dependency in percentage (take Kevlar as an example).

3

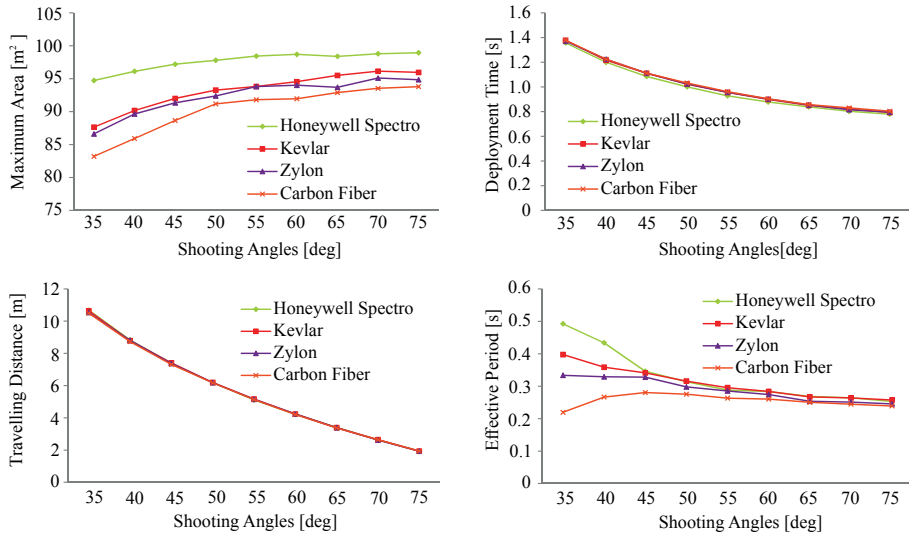


Figure 3.11: Dynamic net parameters changing with different shooting angles (By MS model).

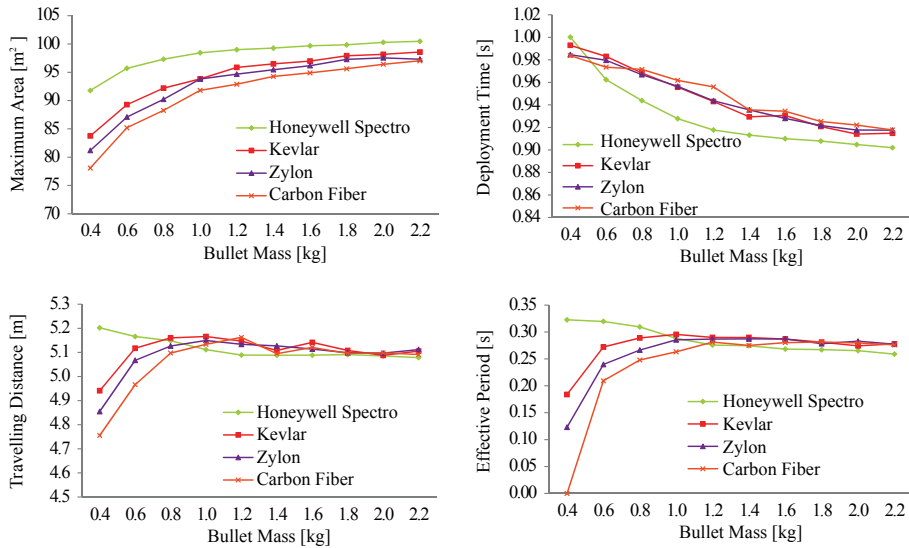


Figure 3.12: Dynamic net parameters changing with different bullet masses (By MS model).

Table 3.3: Output parameters' dependency on initial input parameters. A '-' denotes an inverse dependency. The numbers in the brackets show the relative deviation and the starting value of each input parameter.

	Maximum Area	Deployment Time	Travelling Distance	Effective Period
Initial bullet velocity (180% 10 m/s)	1.28%	-35.61%	0.31%	-35.01%
Shooting angles (85.71% 35°)	8.30%	-37.13%	-71.58%	-30.82%
Bullet mass (450% 0.4 kg)	3.93%	-1.75%	0.74%	11.34%

### 3.5. VERIFICATION AND VALIDATION

As stated previously, the mass-spring model is the most commonly used model for a space net so far. The ANCF model for a net has only been touched by researchers without further discussion. Both models are not verified sufficiently. In this section, two models are cross-verified and experimentally validated.

#### 3.5.1. CROSS-VERIFICATION

The ANCF model that is capable to describe the flexible configuration of the net with fewer nodes, is explored and compared with the mass-spring model. A set of simulations are performed with the same initial conditions as that in the simulations based on the mass-spring model. Kevlar is chosen as the net material in this comparison. Figure 3.13 and 3.14 show the net deployment simulations based on the mass-spring model and the ANCF model, respectively. In the simulations based on the ANCF model, the introduced inwards-folding scheme of the net is used as shown in Fig. 3.2. The damping effect is not considered in both models in this comparison.

It is seen from Fig. 3.13 and 3.14 that the net configurations obtained from the mass-spring model and the ANCF model at a certain moment have a good agreement with each other, which indicates that the ANCF modeling method is also suitable to model a net. To further investigate the capability of the ANCF model, we also investigated the dependency on the four critical output parameters by the initial deployment conditions using both the mass-spring model and the ANCF model, as shown in Fig. 3.15 to Fig. 3.17. The initial input parameters for the ANCF model are set exactly the same as three cases introduced in Section 3.4.2. The comparison of the ANCF and the mass-spring model shown in Fig. 3.15 to Fig. 3.17 displays a great agreement of both models.

While we have shown that both models yield comparable results with figures, it is interesting to quantitatively compare their differences further. Table 3.4 shows the maximum differences in percentage of two models, which is obtained using

$$\Delta = \frac{\max|x_M - x_A|}{x_M}. \quad (3.19)$$

Here  $x_M$  is the data from the mass-spring model and  $x_A$  is the data from the ANCF model. It is seen from the table that the maximum differences between these two modeling methods are below 10% except for the effective period due to its own sensitivity.

Even though the ANCF model obtains a comparable results with the mass-spring model and it can better describe the flexibility of the net than the conventional mass-

3

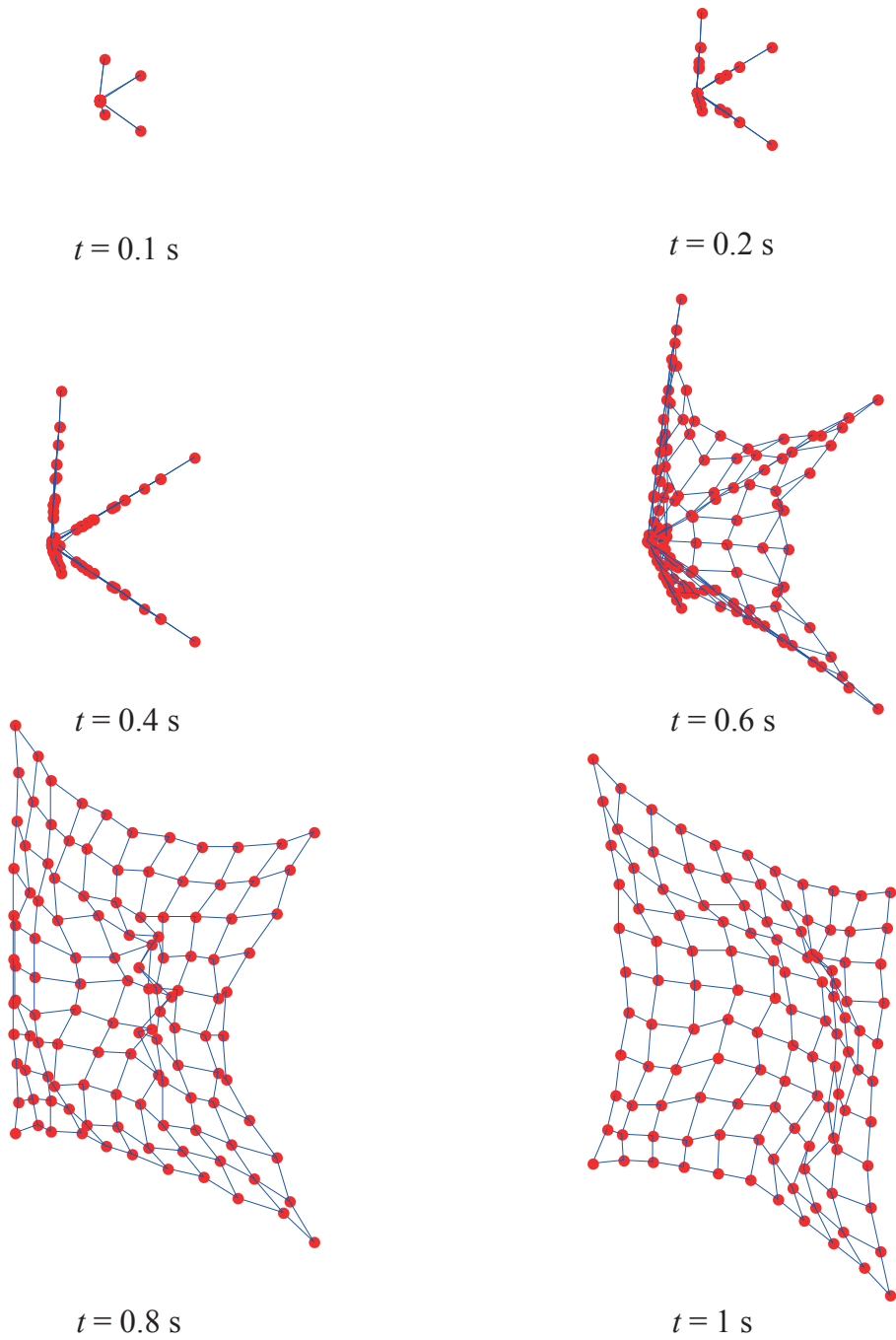


Figure 3.13: Net deployment simulation by Mass-spring model

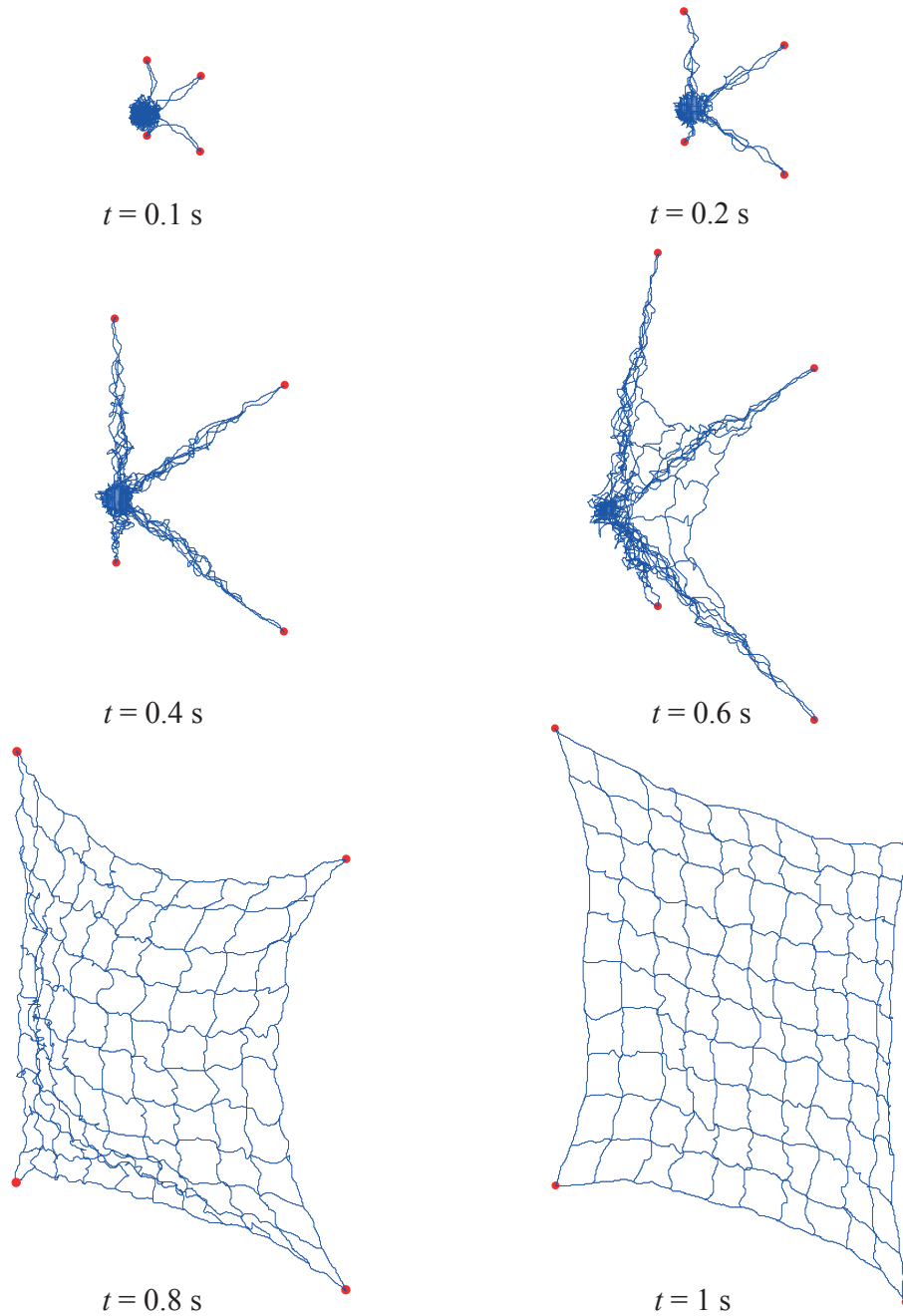


Figure 3.14: Net deployment simulation by ANCF model

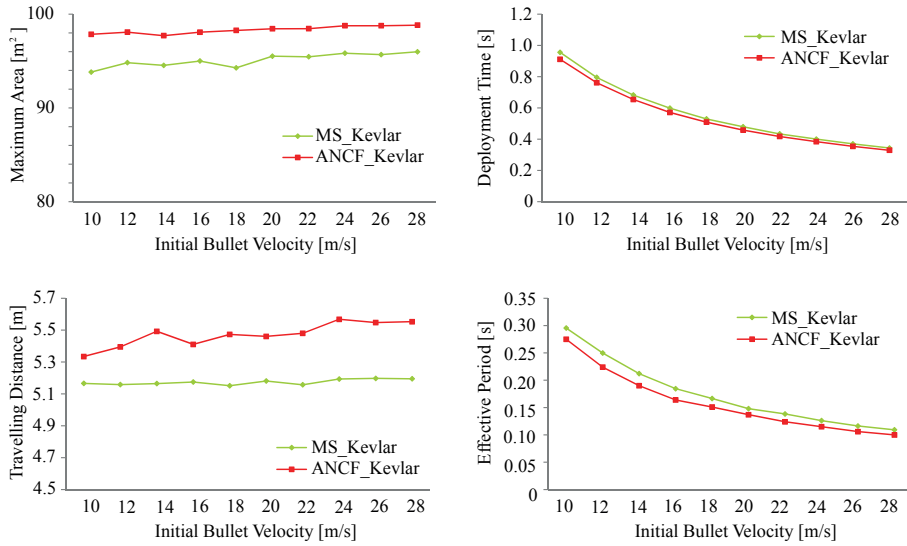


Figure 3.15: Comparison of ANCF and Mass-spring model with different initial bullet velocities

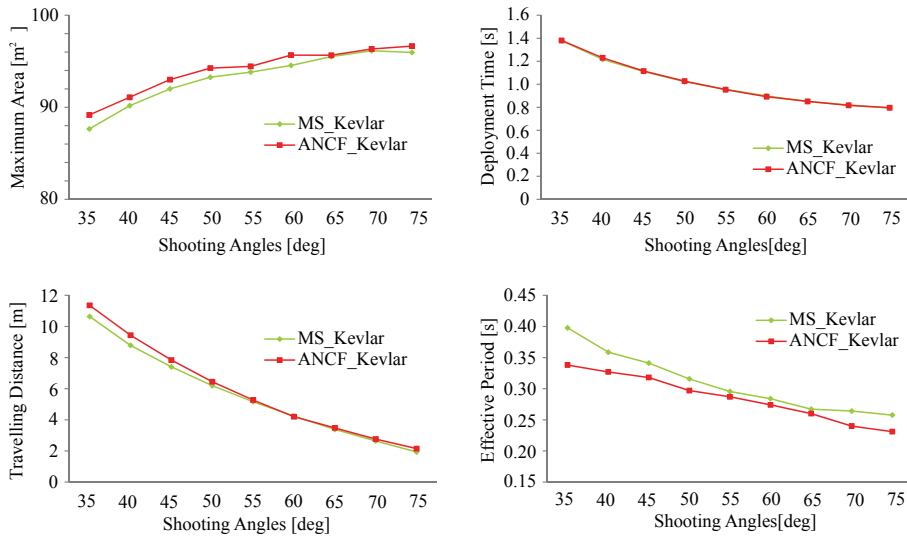


Figure 3.16: Comparison of ANCF and Mass-spring model with different shooting angles

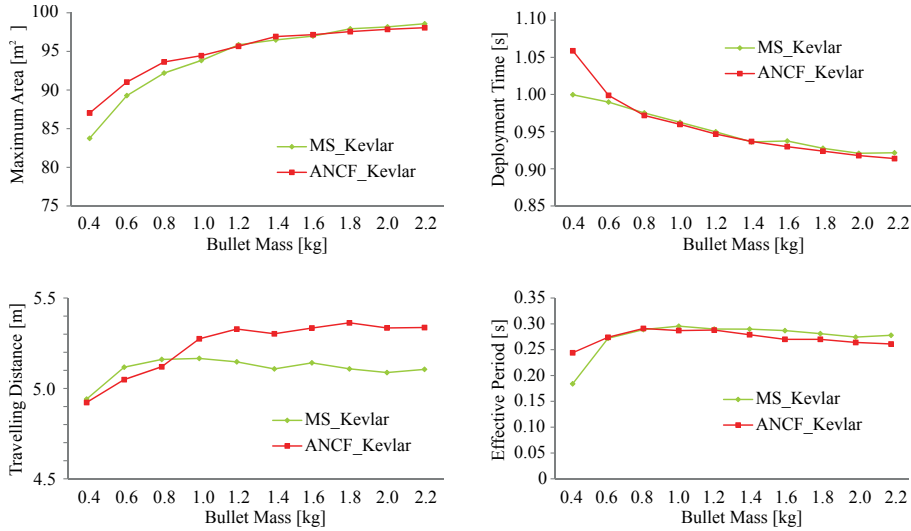


Figure 3.17: Comparison of ANCF and Mass-spring model with different bullet masses

Table 3.4: Maximum difference between the ANCF and the mass-spring model

	Maximum Area	Deployment Time	Travelling Distance	Effective Period
Initial bullet velocity	4.29%	4.68%	7.22%	10.32%
Shooting angles	1.71%	1.11%	6.72%	15.01%
Bullet mass	3.90%	5.95%	6.27%	32.61%

Table 3.5: Comparison of single step computational time of ANCF and Mass-spring model

	Mass-spring Model	ANCF Model
Number of Nodes	121	121
Degrees of Freedom	363	5280
Single Step of Computational Time	7.883 ms	114 ms

spring model, it is much more computationally expensive compared to the conventional mass-spring model because of more degrees of freedom at each node and the complicated evaluations of the elastic forces. Table 3.5 shows the comparison of the computational time in a single step of both modeling methods. It is noticed from the table that the mass-spring model is around 14 times faster than the ANCF model in one single step when they are run in the same simulation environment.

### 3.5.2. VALIDATION BY PARABOLIC FLIGHT EXPERIMENT

#### EXPERIMENTAL

Since the introduced modeling methods allow to simulate the net deployment for space debris removal, these two models have to be experimentally validated. Moreover, in order to reduce the gravity influence, an experiment has to be performed in a micro-gravity environment. The zero-gravity environment can be created in e.g., a drop tower, a neutral buoyancy laboratory, a parabolic flight or space. To ensure an enough experimental period for net deployment and to make it less costly, in this case we use a parabolic flight experiment. This parabolic flight experiment was led by SKA Polska under an ESA contract, and it was performed on board of a Falcon-20 airplane, operated by National Research Council in Ottawa, Canada. The airplane used in the experiment is a 12-seats, 2-engines business jet with the whole cabin available for micro-gravity experiments. The cabin dimensions are 4 m, 1.5 m and 1.6 m in length, width and height, respectively. Depending on the flight profiles, it may achieve micro-gravity periods of up to 23 s with the magnitude of the micro-gravity up to 0.01 g (Gołębowski et al., 2015a).

Due to the geometrical constraint of the airplane, the experiment had to be down-scaled to fit the cabin. The net and an Envisat mock-up are downscaled by a factor of 25. The scaling leads to the net cable diameter a fraction of millimeter, which is almost invisible to the cameras. Therefore, the minimal diameter is achieved based on the camera resolution and the distance to the camera. Moreover, the scaling leads to the stiffness of net material not achievable for solid material, thus the material with small stiffness, Nylon, is chosen as the net material. The Envisat mock-up is firmly connected to a rig instead of being free floating, with a net shot by a pneumatic net ejector to contact the target and wrap it. Figure 3.18 shows the scheme of the parabolic flight experiment. As shown in the figure, the entire process was recorded with two fast stereographic camera sets, such that it is possible to fully reconstruct the 3D trajectory of each individual knot within the net. The reconstruction of the net trajectories can be reduced to the problem of marking 2D positions of net's nodes, labeling them with individual knot IDs on each frame of the particular parabola recording and calculating their 3D positions using a triangulation algorithm. However, when the net is not fully deployed, the knots are very close to each other and their interconnections are not well visible. Hence, the trajectory of some knots is incomplete in the early deployment phase. However, some of the trajectory data can be achieved by linear interpolation with the collected data. Those which neither are collected, nor possible to be achieved by linear interpolation, have not been used for comparison in this thesis. A snapshot of the parabolic flight experiment is shown in Fig. 3.19, and detailed information of this parabolic flight experiment is provided in (Gołębowski et al., 2015b,a). The net used in the experiment is  $10 \times 10$  meshed, and other key parameters of the parabolic flight experiment are summarized in Table 3.6.

#### DISTURBANCES AND SIMULATIONS

As the experimental environment is not strictly gravity-free during the parabola, and the plane was rotating which generates the Coriolis effect on the net, accelerometers and gyroscopes are equipped in the cabin to measure the micro-gravity condition and the rotation rate of the airplane. Figure 3.20 shows the residual gravity and angular velocity recordings along three axes during the net deployment. The orientation of the coordi-

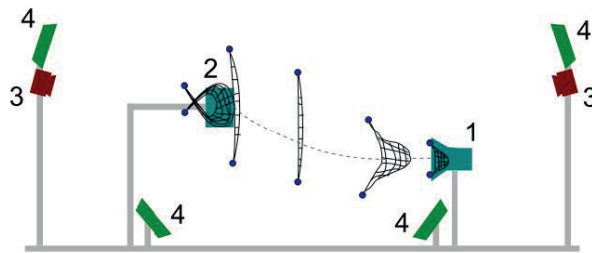


Figure 3.18: Scheme of parabolic flight experiment (1. net ejector, 2. satellite mock-up, 3. stereo cameras pairs, 4. lights) (Gołębowski et al., 2015b).

3



Figure 3.19: Parabolic flight experiment (Gołębowski et al., 2015a).

Table 3.6: Parameters of the parabolic flight experiment (Gołębowski et al., 2016)

Parameter	Value
Net size $A$ , [m <sup>2</sup> ]	0.8×0.8
Mesh length $l_0$ , [m]	0.08
Cable diameter $d$ , [mm]	1
Edge cable diameter $d_e$ , [mm]	3
Bullet mass $m_b$ , [kg]	0.03×4
Material elastic modulus $E$ , [Pa]	4.456×10 <sup>8</sup>
Shooting velocity $v$ , [m/s]	1.8
Shooting angle $\theta$ , [°]	25

nate frame is given in Fig. 3.24.

Simulations based on the mass-spring model and the ANCF model are performed with the same parameters and initial conditions as applied in the experiment. Figure 3.21

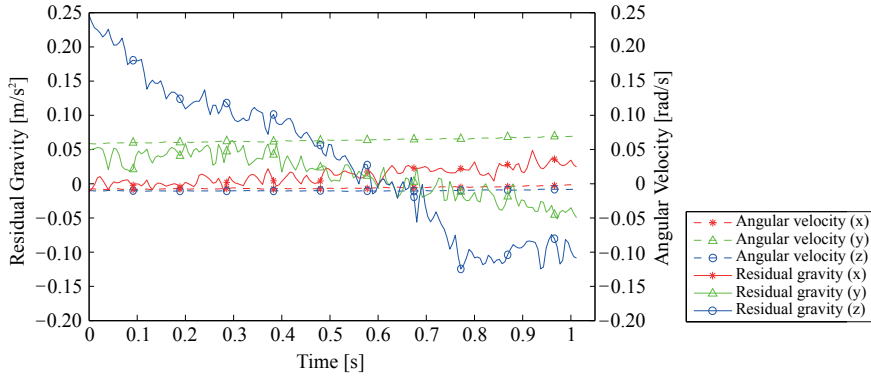


Figure 3.20: Angular velocity and residual gravity.

illustrates the net deployment process in three stages: early deployed stage, middle stage and fully deployed stage. Since the disturbances, in this case the residual gravity and the Coriolis acceleration caused by the airplane rotation, significantly affect the net trajectory, respective variable force fields are applied to both modeling methods (Eq. 3.5 and Eq. 3.16) in the simulations.

To identify the influence of the disturbance on the net trajectory, the following simulations based on both models are performed by taking the central knot (Knot (5,5) in Fig. 3.22) as a target knot: (1) with residual gravity effect only, (2) with Coriolis effect only, (3) with residual gravity and Coriolis effect, (4) without any disturbances. The results have shown that for the central knot, either of the above-mentioned disturbances has little influence for its trajectory along the traveling direction, namely the  $x$  direction. In contrast, both disturbances have affected the motion of the central knot along the  $y$  and  $z$  directions which are supposed to be trivial in the absence of disturbance due to the symmetric configuration of the net. Specifically, the maximum diversion of the central knot along the  $y$  direction is less than four centimeters under both of the disturbances, indicating the disturbances influence is trivial on the  $y$  direction. However, the derivation of motion along the  $z$  direction of the central knot has reached a magnitude of 0.15 m, as shown in Fig. 3.23. This can be explained by the fact that the residual gravity has a much larger component along the  $z$  direction than that along other axes. Also the high angular velocity along the  $y$  direction results in a larger Coriolis effect in the  $z$  direction. Such motion derivation demonstrates that the curvy net trajectories shown in Fig. 3.18 and Fig. 3.19 are governed by the existing disturbances.

### VALIDATION RESULTS

We have introduced and processed the data backed up for the parabolic flight campaign experiment to reconstruct the 3D trajectory of the net. These digitally reconstructed trajectories are then used to compare with those obtained from simulations so as to validate the modeling methods.

Figure 3.24 illustrates the net configuration constructed based on the experimental data and the simulations. Specifically, the configuration for instants of the three deployment stages, namely, early deployed moment, middle stage moment and fully deployed

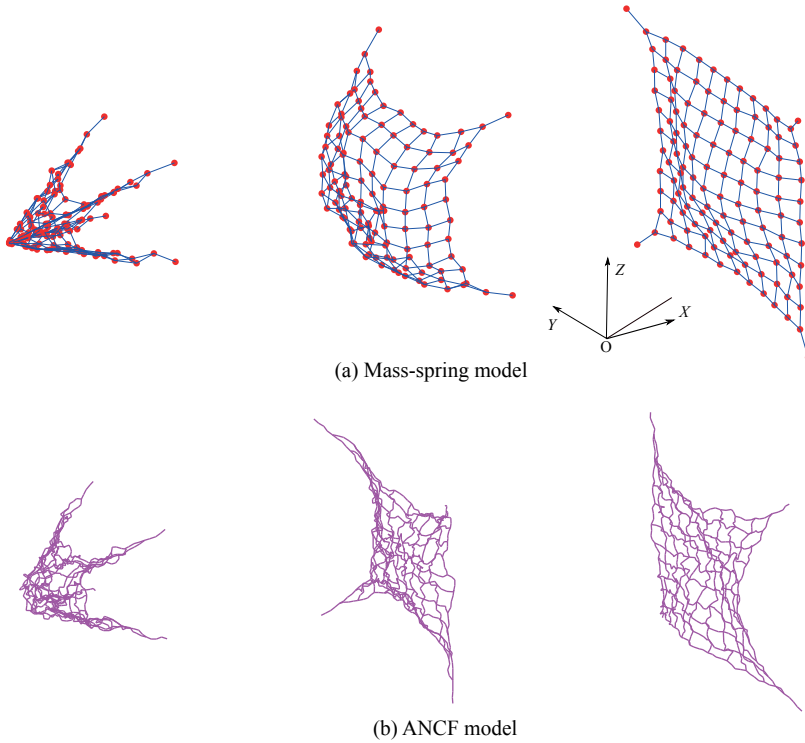


Figure 3.21: Net deployment simulations based on the MS model and the ANCF model.

moment, are presented. As shown in the figure, for the middle stage moment, the net configuration based on the mass-spring model differs significantly from the others. To further quantitatively analyze the difference, the trajectories of the selected typical knots are plotted and presented in Fig. 3.25, Fig. 3.26, and Fig. 3.27. The selected knots are grouped as bullets, edge knots (four knots on edges) and inner knots (four knots in the inner part of the net), as shown in Fig. 3.22. Note that in both the simulation and the experiment, the measured data are transformed into the same coordinate frame, of which the origin of the frame is located at the center of the shooting device and the orientation is given in Fig. 3.24. The Figures 3.25-3.27 show that the trajectories of the selected knots present the same trend and differences between the simulation and the experiment are kept within 0.35 m. Differences of bullets are even smaller. Such comparison demonstrates that the simulation results are in a good agreement with the experiment.

Despite the good agreement between the simulations and the experiment, the plots have shown that the residual errors of the two models (mass-spring model and ANCF model) are non-negligible, especially for the edges knots and the inner knots. Therefore, the absolute residual and the average relative residual are discussed in the following. The absolute residual of each knot along the three axes  $\mathbf{r}e_i$  can be defined as

$$\mathbf{r}e_i = |\mathbf{s}_i - \mathbf{e}\mathbf{x}_i|, \quad (3.20)$$

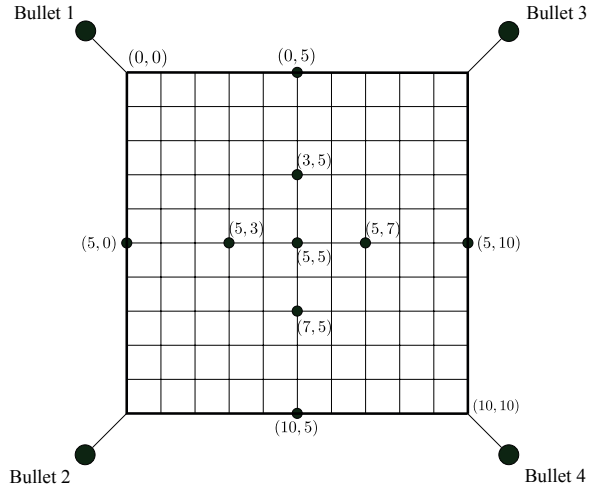
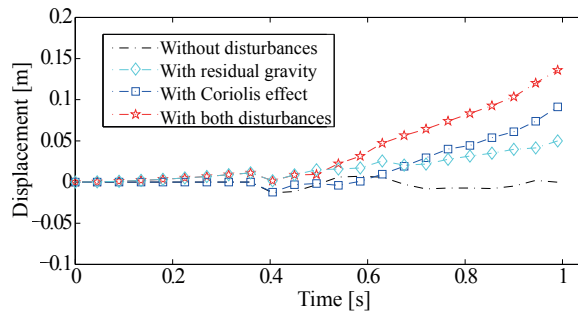
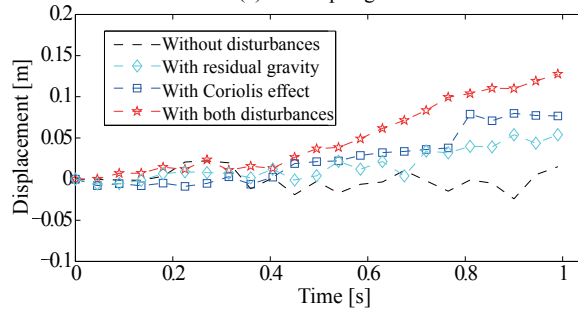


Figure 3.22: Knots coordinates of the net.



(a) Mass-spring model



(b) ANCF model

Figure 3.23: Central knot trajectories under disturbances along  $z$  direction.

where  $\mathbf{s}_i$  and  $\mathbf{e}\mathbf{x}_i$  represent the displacement of the  $i$ th node in the simulation and in the experiment, respectively. Some relatively larger residuals over time on typical knots are shown in Fig. 3.28.

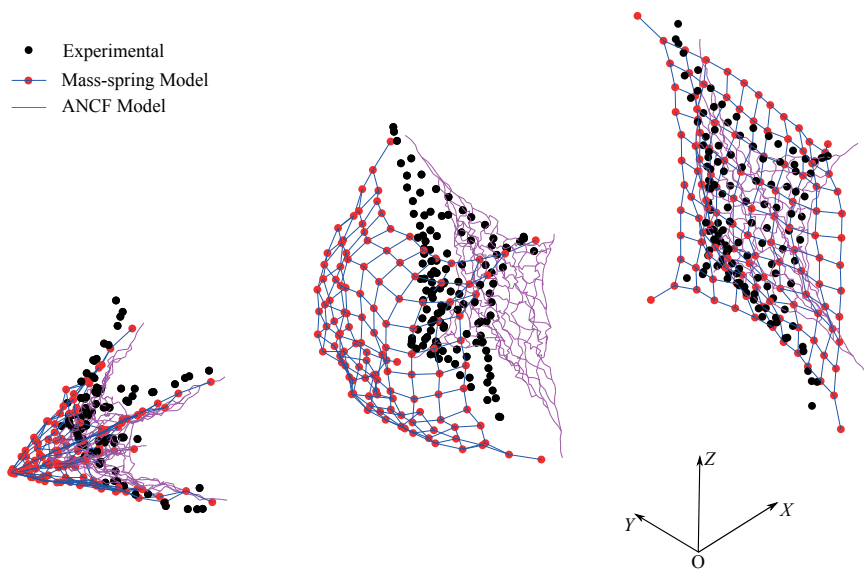


Figure 3.24: Comparison of net deployment simulations and parabolic flight experiment.

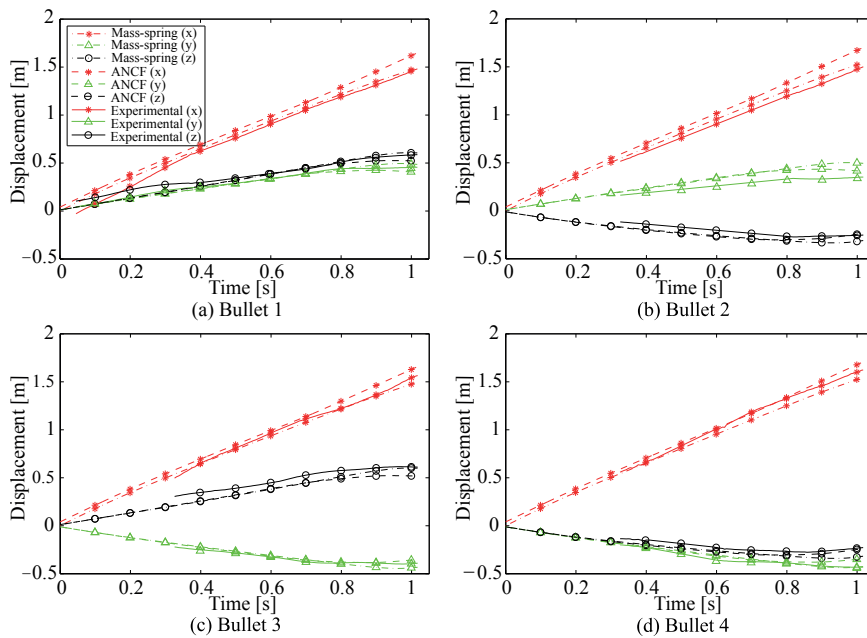


Figure 3.25: Comparison of the bullets trajectories.

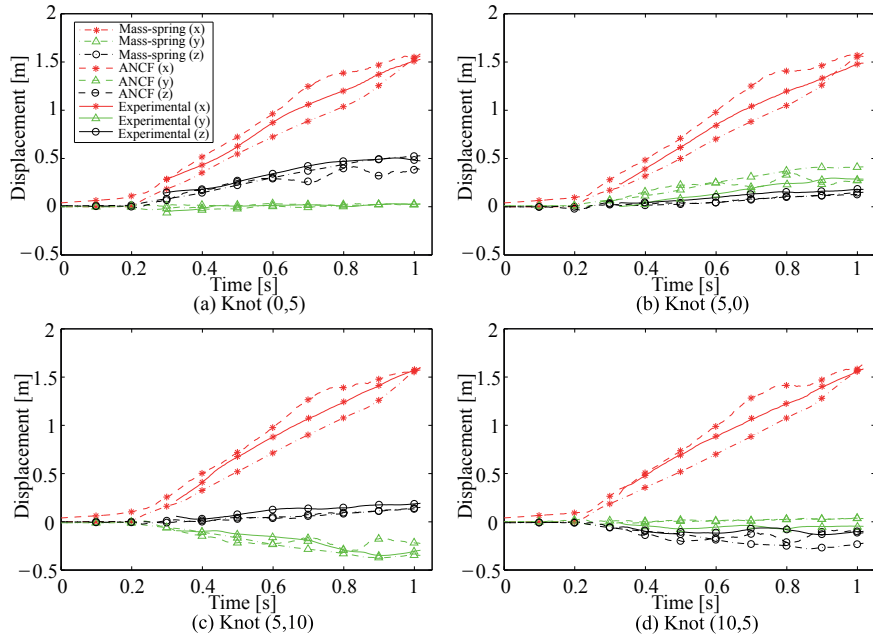


Figure 3.26: Comparison of the edge knots trajectories.

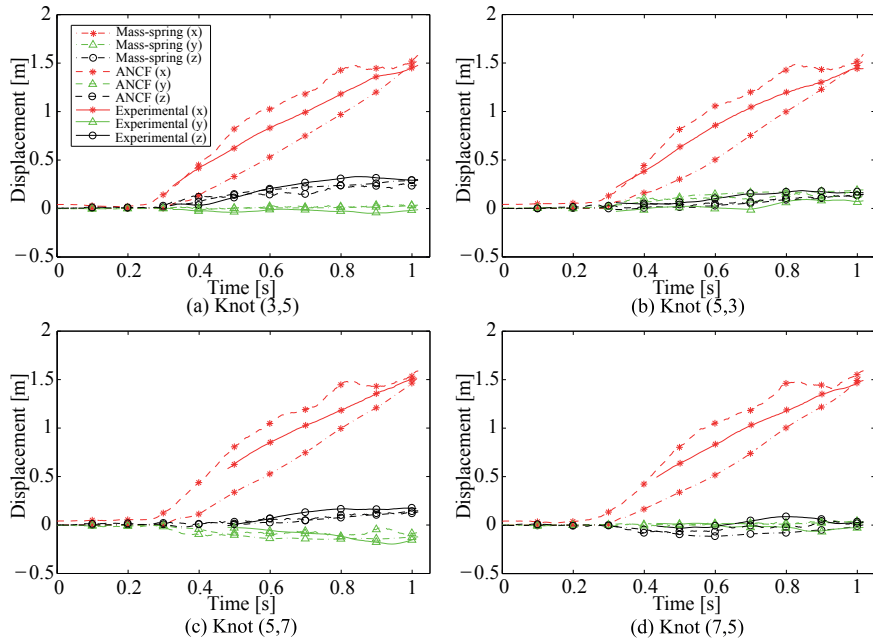


Figure 3.27: Comparison of the inner knots trajectories.

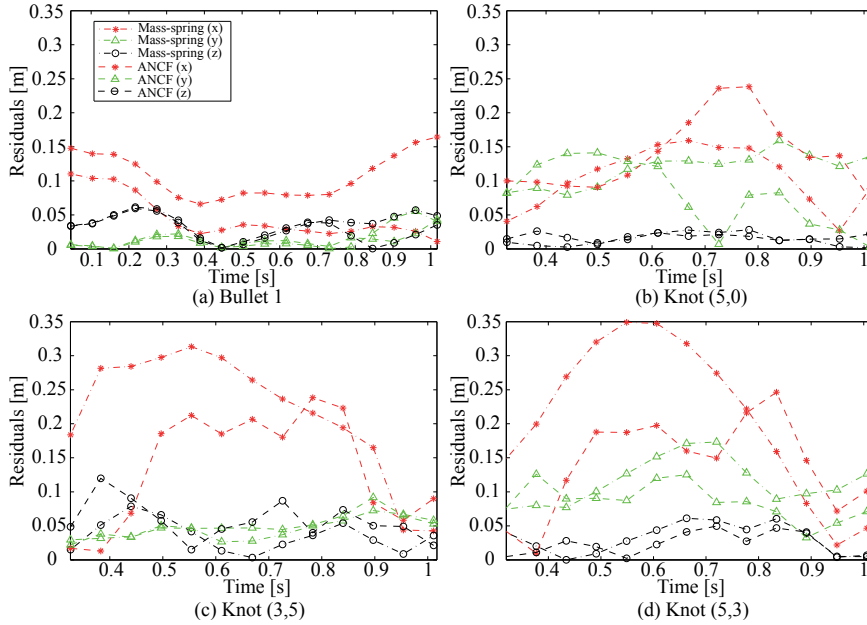


Figure 3.28: Absolute residuals over time of some typical knots.

To statistically present the residual during the net deployment period, the residuals of each selected knot along three axes are shown using boxplot in Fig. 3.29, in which the markers in the boxes represent the mean value of the residuals within the deployment time. It is clearly observed that the residuals of the bullets are restricted within 0.2 m, which is less than that of the other knots. Moreover, due to the symmetric configuration of the net along the  $y$  and  $z$  axes, the residuals along those axes are always smaller compared with those along the  $x$  direction. In addition, for the bullets, residuals of the mass-spring model are smaller, especially in the  $x$  direction; on the contrary, for the inner knots, residuals of ANCF model are always less significant. This is because the masses of the cables are evenly distributed in the ANCF model, which better describe the nature of the cables than the mass-spring model. Such comparisons indicate that, under the net configuration as shown in Fig. 3.22, the mass-spring model can better reflect the bullet movements, whereas the ANCF model is superior to the mass-spring model in describing the motion of the inner knots of the net.

The average relative residual  $ar_i$  is defined as the mean percentage of the relative residual of each group of knots (the bullets, the edge knots or the inner knots), which takes the expression

$$ar_i = \frac{1}{n} \sum_{i=1}^n \frac{re_i}{D_i} \times 100\%, \quad (3.21)$$

where  $D_i$  is the farthest distance that the node  $i$  traveled along the  $x$ ,  $y$  or  $z$  direction. Table 3.7 presents the average relative residuals of the mass-spring model and the ANCF model. It has been indicated that both models are able to describe the bullet trajectory-

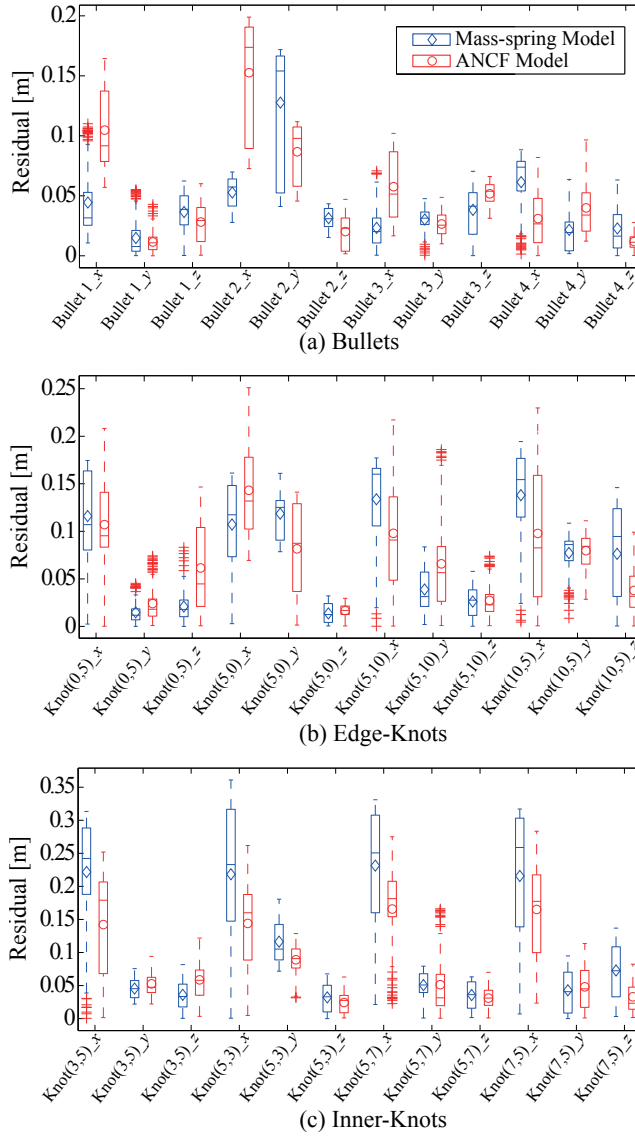


Figure 3.29: Residuals of the selected knots with boxplot.

Table 3.7: Average relative residual of the mass-spring model and the ANCF model w.r.t. experimental

<b>Knots</b>	<b><math>x</math> MS</b>	<b><math>x</math> ANCF</b>	<b><math>y</math> MS</b>	<b><math>y</math> ANCF</b>	<b><math>z</math> MS</b>	<b><math>z</math> ANCF</b>
Bullets	2.94%	5.71%	13.26%	10.87%	7.72%	6.09%
Knots on the edges	7.97%	7.23%	41.75%	44.79%	19.06%	15.96%
Inner knots	14.95%	10.39%	75.45%	72.00%	44.29%	27.75%

ries and the knots displacement along the  $x$  direction with an average relative residual less than 15%. Most relative residual percentages of the ANCF model are less than that of the mass-spring model except for the bullets displacement in the  $x$  direction and the edge knots displacement in the  $y$  direction. Therefore, with the net configuration as shown in Fig. 3.22, the ANCF model has a higher accuracy in describing the general movement of the entire net. The table also demonstrates that the relative residual percentages along the  $y$  and  $z$  directions are much more significant in the edges knots and the inner knots. This is understandable since the symmetric configuration of the net leads to a small value for the denominator in Eq. 3.21. However, the absolute residuals of these knots along these two axes are relatively smaller, up to 0.1 m, as shown in the boxplot in Fig. 3.29.

### 3.6. SUMMARY

In this chapter, the dynamic characteristics of a net in its deployment phase have been investigated. Four critical parameters describing the deployment dynamic characteristics of the net, namely, the maximum area, the deployment time, the travelling distance and the effective period have been identified and defined. These parameters have been investigated by simulations under different initial input parameters, namely, the initial bullet velocity, the shooting angle and the bullet mass. It is concluded that a higher bullet mass, shooting angle and more flexible net material contribute to a larger net area. The net material has little influence on deployment time and travelling distance. Moreover, a higher initial bullet velocity and a larger shooting angle lead to a shorter effective period which renders the capturing with a higher risk to fail and therefore less reliable. The dependency of four output parameters on different initial input parameters has been provided quantitatively. Besides, a comprehensive study on modeling of a net based on ANCF has been provided. Simulations based on ANCF have been performed and compared with the conventional mass-spring model. The results from both methods show a good agreement with respect to the sensitivity of the four critical parameters, which indicates that the ANCF model is also suitable to describe the deployment dynamics of a net. The maximum differences between two methods are below 10% except for the sensitive effective period. Furthermore, the ANCF model is more capable of describing the flexibility of the net with fewer nodes than the conventional mass-spring model. However, it is more computationally expensive. Based on the comparison of single-step computational time, the mass-spring model is nearly 15 times faster than the ANCF model.

To verify the two methods, data from a parabolic flight experiment has been used which allow to compare with the simulations of both models. From the analysis of

the absolute residual and the average relative residual between the simulations and the parabolic flight experiment results, it is concluded that, under a net configuration as shown in Fig. 3.22, both models are able to describe the movement of the bullets and the net movement along the traveling direction with an average relative residual error up to 15%. Moreover, the mass-spring model is superior in reflecting the movements of bullets along the traveling direction in comparison to the ANCF model. On the contrary, the ANCF model is superior to the mass-spring model in describing the dynamics of the inner knots of the net. This chapter focused on the net deployment phase, while the contact dynamics implemented in both net models and the validation of the capturing dynamics are discussed in the following chapters.

# 4

## CONTACT DYNAMICS OF NETS AND TARGETS

---

Parts of this chapter have been published in Minghe Shan, Jian Guo, Eberhard Gill. *Contact Dynamic Models of Space Debris Capturing Using A Net*, Acta Astronautica (2017).

### 4.1. INTRODUCTION

The process of space debris capturing with a net can be divided into two steps, namely, net deployment and target capturing. Net deployment dynamics has been investigated in Chapter 3. This chapter covers the second step, target capturing, and focus on the contact dynamics between the net and the target. To better understand the contact dynamics from a mathematical point of view, it is necessary to classify the dynamics problem. The dynamics problem consist of three categories based on the types of constraints as shown in Fig. 4.1: unconstrained problem, equality constrained problem and inequality constrained problem. As the name implies, unconstrained motion refers to the motion without any external constraints, e.g., free falling of an object (Fig. 4.1 (a)). Equality constrained problem, also named as "bilateral constrained problem", means that the expressions of all the constraints in the system can be formulated as equality expressions. Taking the crank-sliding mechanism as an example (Fig. 4.1 (b)), suppose  $\mathbf{x}_0$  and  $\mathbf{x}_1$  are vectors of two points on different bodies which are jointed at point  $O$ . Here,  $\mathbf{x}_0$  represents the vector of one end of the crank and  $\mathbf{x}_1$  represents the vector of one end of the link. The constraint  $\mathbf{x}_1 - \mathbf{x}_0 = 0$  must hold during the entire motion. An inequality constrained problem, also named as "unilateral constrained problem", means that the expressions of some constraints in the system can be formulated as inequality expressions. For example, when a mass point has to move on the left side of a surface as shown in Fig. 4.1 (c), the constraint is  $f(\mathbf{x}_m) > 0$ , where  $f$  is the function of the surface and  $\mathbf{x}_m$  is the vector of the mass point.

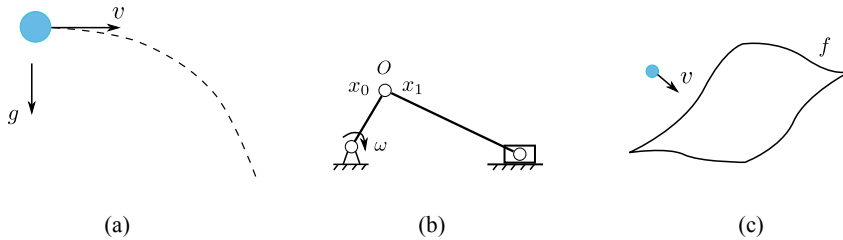


Figure 4.1: Constraint motions: (a) Unconstrained motion. (b) Equality constrained motion. (c) Inequality constrained motion.

The contact problem can be considered as an inequality constraint problem since the contacting bodies are not allowed to intersect each other. The contact modeling methods commonly used are the penalty-based method (Flores and Lankarani, 2016) and the impulse-based method (Mirtich and Canny, 1995). In the penalty-based method, contact forces are expressed as continuous functions of the penetrations between contacting bodies (Flores and Lankarani, 2016). The penalty-based method is straightforward to be implemented either in programming or in analytical form. Botta et al. (2016a) and Benvenuto et al. (2016) both used the penalty-based method to evaluate the contact forces between the net and the target. However, in the penalty-based method, a large contact stiffness is needed to keep the penetration sufficiently small such that it will generate large forces leading to a stiff equation system. Moreover, a contact stiffness suitable for one situation may not necessarily be adequate for another due to the different ma-

materials of the contacting bodies. Additionally, fictitious penetration between the net and the target cannot be avoided. The impulse-based method calculates the impulse applied on the contacting bodies, thus calculating their respective velocity changes. The immediate velocity changes are able to prevent the interpenetration between the contacting bodies since the bodies start to move away from each other once the contact occurs. The impulse-based method has been widely used in game and/or virtual reality environments (Chang and Colgate, 1997; Bender, 2007). Furthermore, it is commonly used in the contact between two separate bodies (Mirtich, 1996). However, the net capturing process is treated as multiple mass points, representing the net, contacting with one single object. The impulse-based method applied in this situation needs to be derived. In this chapter, the penalty-based method is reviewed and the impulse-based method as a contact modeling method is being used in the net capturing scenarios. Analytical solutions for this specific situation are derived based on both methods. Moreover, both methods have to be verified and experimentally validated. This chapter presents the verification and validation of both methods. The cross-verification of both methods is made by comparing the simulation results of the capturing of basic shaped targets, such as a cube, a ball and a cylinder. The validation of both models is made by comparing the simulation of the capturing of an Envisat mockup with the parabolic flight experiment introduced in Chapter 3. The effectiveness of both models for space debris capturing is therefore demonstrated.

## 4.2. PENALTY-BASED METHOD

Since a net is assumed to be multiple mass points connected with spring-dashpot elements in a certain pattern, net contacting with a target can be considered as multiple mass points contacting with the surfaces of the target as shown in Fig. 4.2. The mass points have to move outside the space of the target and they are not allowed to penetrate the target. According to this description, net capturing is an inequality constraint problem as previously discussed. The penalty-based method, which is usually used in

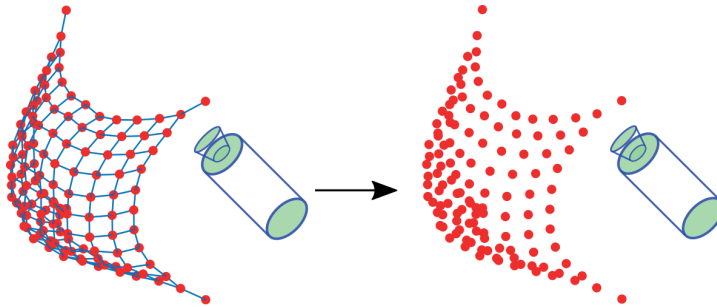


Figure 4.2: Net contacting with a target (left) and simplified contact scenario (right).

the optimization problem, is a very attractive method to solve the inequality constraint problem. In the optimization problem, an inequality constraint problem can be formulated as

$$\text{Minimize } f(x), \text{ subject to } c(x) \geq 0 \quad (4.1)$$

where  $f(x)$  is the objective function,  $c(x)$  is the constraint equation. It is possible to convert this inequality constraint problem into a suitable unconstrained problem as

$$\text{Minimize } f(x) + \mu \min\{0, c(x)\}, \quad \text{subject to } x \in R^n \quad (4.2)$$

The term " $\mu \min\{0, c(x)\}$ " is called the penalty function. If  $c(x) \geq 0$ , then  $\min\{0, c(x)\} = 0$  and no penalty occurs. If by any chance,  $c(x) < 0$ , then  $\min\{0, c(x)\} = c(x)$ . The penalty should be added into the objective function to prevent this from happening. Taking the point-surface contact problem as an example, the point is constrained to be always moving above the surface, which is  $c(x) \geq 0$ . If the constraint equation holds, which means the point is not contacting with the surface, thus  $\min\{0, c(x)\} = 0$ . On the contrary, if it is detected that  $c(x) < 0$ , which means the point is penetrating the surface. The penalty force, here the contact force,  $\mu c(x)$  will be added to  $f(x)$  to push the point away from the surface and prevent the penetration from continuing.

According to this definition, the penalty function, " $\mu \min\{0, c(x)\}$ ", can be considered as a function of the penetration depth. In fact, a contact between the elastic bodies will lead to a deformation on colliding bodies, and the contact force can be expressed as a function of the contact deformation. In the simulation of a contact scenario, the contact deformation can be parameterized as a function of the penetration depth between the colliding bodies. In the penalty-based method, the response force depends on the penetration depth: the larger the penetration, the higher the penalty.

#### 4.2.1. NORMAL CONTACT FORCE

According to the review of the contact dynamics modeling by Gilardi and Sharf (2002), two main categories of contact dynamics models can be distinguished: discrete models and continuous models. Discrete models assume that the impact process is instantaneous. Therefore they are not applicable to the penalty-based method. Commonly used continuous contact dynamics models are: spring-dashpot model, Hertz's model and non-linear damping model. Those models account for the normal force based on the deformation. The direction of the force is along the normal line of the contact. Table 4.1 lists the expressions of the normal contact forces in those models. In the expressions,  $k$  represents the contact stiffness,  $d$  represents the damping coefficient,  $\delta$  represents the deformation or the penetration in the simulation, and  $n$  represents a coefficient depending on the materials and geometries of the contacting bodies.

Table 4.1: Comparison of Three Contact Dynamic Models

Contact Models	Expressions
Spring-dashpot model	$f_n = k\delta + d\dot{\delta}$
Hertz's model	$f_n = k\delta^n$
Nonlinear damping model	$f_n = k\delta^n + d\dot{\delta}^n$

Figure 4.3 shows contact force history of those models. The spring-dashpot model assumes that a spring-dashpot element is set between the colliding bodies. However, this spring can only be compressed, i.e., it only pushes bodies away from each other rather than pull them together. The linear and explicit normal force  $f_n$  depends on the

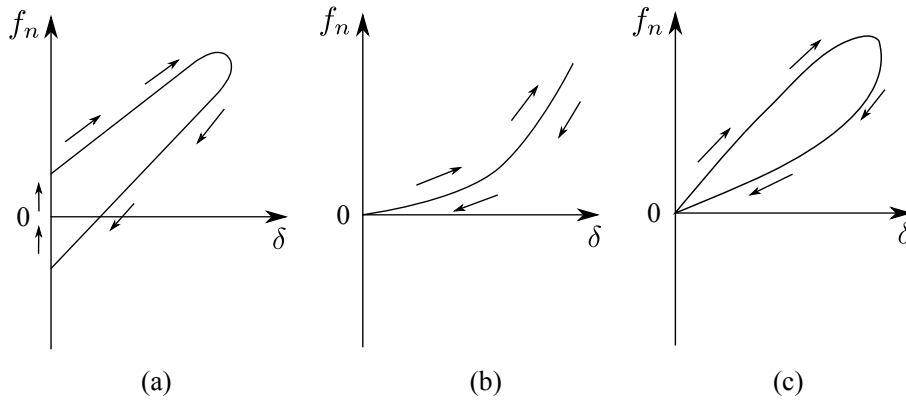


Figure 4.3: Continuous Contact dynamics models: (a) Spring-dashpot model. (b) Hertz's model. (c) Non-linear damping model.

penetration depth  $\delta$  and the penetration rate  $\dot{\delta}$ . However, due to the damping term, the spring-dashpot model involves a discontinuity at the beginning of the contact as shown in Fig. 4.3 (a). Similarly, the contact force holds the colliding bodies together by the end of a contact, which is not realistic. The Hertz's model assumes the contacting bodies interacting via a non-linear spring. Such a model has overcome the defect of the drift at the zero penetration. The normal force is continuous at the beginning and the end of a contact (Fig. 4.3 (b)). However, it does not take the damping into consideration, such that the energy dissipation is not accounted for. The non-linear damping model combines the advantages of the two aforementioned models. It is taking into account the damping and remaining the continuity at zero deformation (Fig. 4.3 (c)). Therefore, the non-linear damping model is selected as the contact model in the penalty-based method throughout this thesis.

While we have selected the contact model for the net capturing, it is necessary to calculate the coefficients, such as the stiffness  $k$  and the damping coefficient  $d$ , in the model. As previously mentioned, the net is modeled as a series of connected mass points. Because of the lightness of the net and the thinness of the cable, the value of the radii of the mass points are assumed to be the radius of the cable, which are negligible compared to the surface of a target. Therefore, the contact of a mass point with the surface of a target can be treated as a sphere-plane contact. According to the Hertzian contact theory (Johnson, 1987), for a sphere-plane contact, the contact stiffness can be obtained by

$$k = \frac{4\sqrt{r}}{3\pi(h_1 + h_2)}, \quad (4.3)$$

with

$$h_i = \frac{1 - \nu_i^2}{\pi E_i}, \quad (i = 1, 2), \quad (4.4)$$

where  $E_i$  and  $\nu_i$  are Young's modulus and Poisson's ratio of the material of the contacting bodies, respectively, and  $r$  is the radius of the contacting mass point. Here,  $i = 1$  indicates

the parameters of the chaser material and  $i = 2$  indicates the parameters of the target material.

For the damping coefficient  $d$ , [Hunt and Crossley \(1975\)](#) have established

$$d = \frac{3\alpha k}{2}, \quad (4.5)$$

where  $\alpha$  is an experimental parameter that varies in the range of 0.08-0.32 s/m according to [Benvenuto et al. \(2016\)](#).

#### 4.2.2. FRICTION

There are several models to describe the friction of two contacting bodies. The Coulomb friction model is the most commonly used model for friction. It has a linear relation with the normal force with a frictional coefficient. However, this model neglects the static friction, which describes the friction at or near zero relative velocity. It also neglects the Stribeck effect, which describes the friction force reduction with increasing relative velocity of contacting surfaces. [Andersson et al.](#), [Specker et al.](#) and [Brown et al.](#) have developed separate friction models to describe the static friction and the Stribeck effect. Among the existing models, Hollars friction model is the most commonly used one due to its advantage of the physical meaning at the transition velocity  $v_{t0}$ . The friction force reaches its maximum at  $v_{t0}$  and decreases with the increasing of the relative velocity. [Figure 4.4](#) shows the comparison of the Coulomb friction model and Hollars friction model, from which it is seen that the Coulomb model is a simplified version of the Hollars model. The expression of the friction force in Hollars model is

$$f_t = [\min\{\frac{v_t}{v_{t0}}, 1\}(\mu_k + \frac{2(\mu_s - \mu_k)}{1 + (\frac{v_t}{v_{t0}})^2})]f_n \quad (4.6)$$

where  $v_t$  is the relative velocity of colliding bodies,  $v_{t0}$  is the transition velocity,  $f_n$  is the magnitude of normal force, and  $\mu_s, \mu_k$  are the coefficients of static and kinetic friction, respectively.

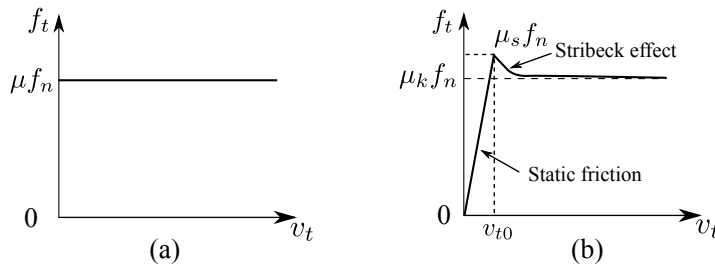


Figure 4.4: Friction models: (a) Coulomb friction model. (b) Hollars friction model.

The frictional force vector generated from the contact is always opposite to the relative velocity along the tangential direction of the contact surface. Assume a mass point  $p_i$  is in contact with an object on point  $O$  and the normal vector of point  $O$  on the object

is  $\mathbf{n}$  (see Fig. 4.5). Then the relative velocity  $\mathbf{v}_r$  of the points  $p_i$  and  $O$  can be expressed as

$$\mathbf{v}_r = \mathbf{v}_{pi} - \mathbf{v}_O. \quad (4.7)$$

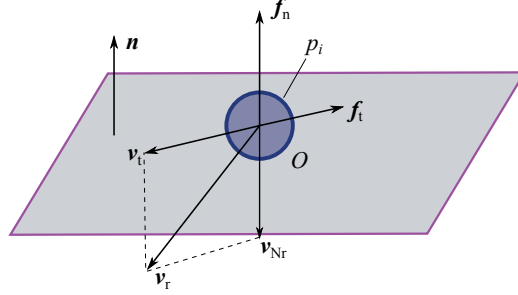


Figure 4.5: Normal and frictional force on contacting point.

The component of the relative velocity along the normal  $\mathbf{v}_{Nr}$  is

$$\mathbf{v}_{Nr} = (\mathbf{n}^T \mathbf{v}_r) \mathbf{n}. \quad (4.8)$$

Therefore, the relative velocity vector along the tangential direction  $\mathbf{v}_t$  is obtained as

$$\mathbf{v}_t = \mathbf{v}_r - \mathbf{v}_{Nr}. \quad (4.9)$$

The friction force  $\mathbf{f}_t$  can therefore be obtained by Eq. 4.6,

$$\mathbf{f}_t = -f_t \mathbf{n}_t, \quad (4.10)$$

with  $\mathbf{n}_t = \mathbf{v}_t / v_t$ .

### 4.3. IMPULSE-BASED METHOD

There are several disadvantages to the aforementioned penalty-based method. For instance, in the penalty-based method, a large contact stiffness is needed to keep the penetration sufficiently small that will generate large contact forces resulting in a stiff equation system. A stiff equation is usually numerically unstable unless the step size is taken extremely small. Moreover, a contact stiffness suitable for one situation may not necessarily be adequate for another due to the different materials of the contacting bodies. In addition, to stop an object penetrating a surface instantaneously requires an infinite force that is impossible to achieve. The impulse-based method can somehow overcome these defects by calculating the impulse between two contacting objects and setting new velocities for those objects in simulation. The impulse-based method is commonly used in game and/or virtual reality environments, especially to model the contact between two separate bodies (Mirtich, 1996). Mirtich et al. have done extensively research on the impulse-based method. However, they consider that the impulse-based method has a weakness on the handling of multiple and simultaneous contacts (Mirtich, 1996). This

thesis, for the first time, applies the impulse-based contact dynamic model on the net capturing of a space debris object. The theoretical solution of multiple and simultaneous contacts is derived and verified by the simulations.

In the simulation of the net capturing of a target based on the impulse-based method, the net is described by the mass-spring model and the target is set at a certain distance away from the net shooter. Contact detection needs to be performed at every step of the simulation. As previously introduced, when using the mass-spring model, a net can be discretized into mass points connected by the spring-dashpot elements under a specific configuration. Therefore, a net contacting with a target is considered as a single mass point or multiple mass points contacting with one single object, as shown in Fig. 4.6. The number of the contacting mass points depends on the relative position of the net and the target. Once a single contact or multiple contacts are detected, contact dynamics takes over the simulation. The algorithm of the net capturing of a target based on the impulse-based method is shown in Fig. 4.7.

4

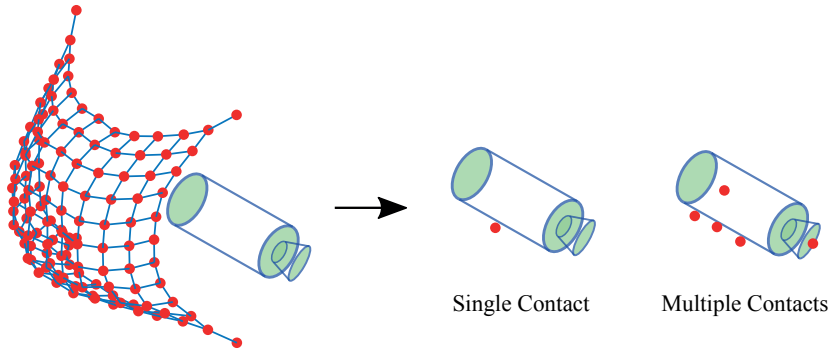


Figure 4.6: Single contact and multiple contacts.

#### 4.3.1. SINGLE CONTACT ON ONE TARGET

A net contacting with a target is typically a simultaneous multiple-contacts problem. However, as a single contact is the basic case of multiple contacts, we first introduce the single contact dynamics to help readers understand the problem. In the impulse-based method, the impulse caused by the contact instead of the contact force, is calculated. Therefore, the velocity change after the contact can be computed once the impulse is known. Introducing the coefficient of restitution to characterize the elasticity of the contact response, the relative velocity change is expressed as

$$e = -\frac{v_r^+}{v_r^-}, \quad (4.11)$$

where  $0 \leq e \leq 1$ . In this chapter, superscript '-' and '+' indicate the status before and after the contact. Thus,  $v_r^+$  is the relative velocity of two objects after contact, and  $v_r^-$  is the relative velocity of two objects before contact. When  $e = 0$ , then  $v_r^+ = 0$ , the contact is fully inelastic, and when  $e = 1$ ,  $v_r^+ = -v_r^-$ , the contact is fully elastic. Assume a single

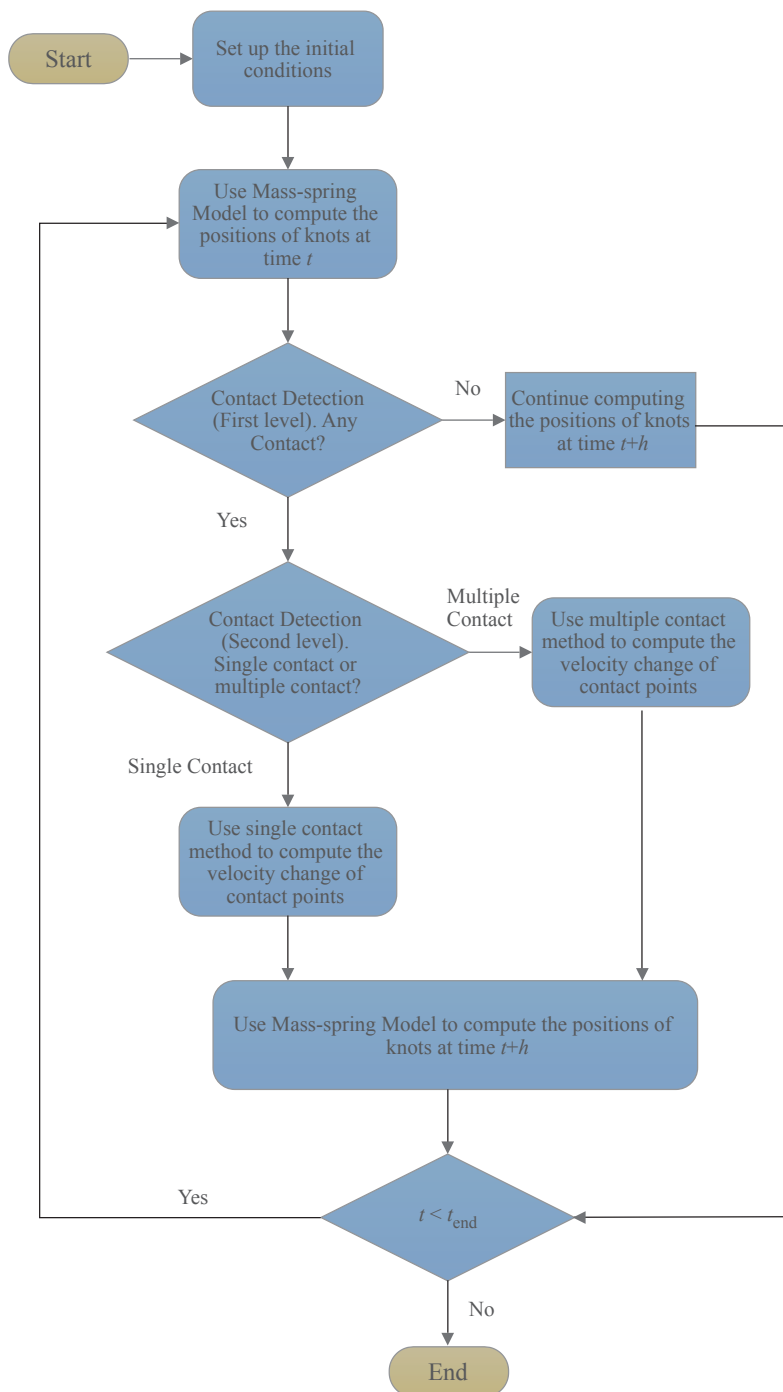


Figure 4.7: Flowchart of the impulse-based method on space debris capturing.

mass point  $P$  contact with an tumbling object  $O$  whose angular velocity is  $\omega_O$  as shown in Fig. 4.8.

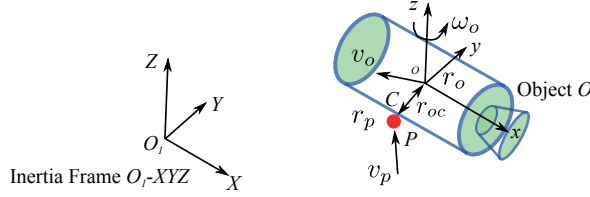


Figure 4.8: Single contact of point  $P$  with an object  $O$ .

4

The position of the mass point is  $r_p$ , and the position of the center of mass of the object is  $r_o$ . Velocities of  $P$  and  $O$  are represented by  $v_p$  and  $v_o$ , respectively. Let  $\mathbf{n}$  represent the normal direction of the contact plane on object  $O$ . Velocities and angular velocities after contact can then be expressed as

$$\mathbf{v}_p^+ = \mathbf{v}_p^- + j\mathbf{n}/m_p, \quad (4.12)$$

$$\mathbf{v}_o^+ = \mathbf{v}_o^- - j\mathbf{n}/m_o, \quad (4.13)$$

$$\boldsymbol{\omega}_o^+ = \boldsymbol{\omega}_o^- - \mathbf{I}_o^{-1}(\mathbf{r}_{oC} \times j\mathbf{n}), \quad (4.14)$$

where  $m_p$  and  $m_o$  are masses of two contact objects,  $\mathbf{I}_o$  is the moment of inertia of the object  $O$ ,  $j$  is the impulse generated from the contact, and  $\mathbf{r}_{oC} = \mathbf{r}_C - \mathbf{r}_o$  is the relative position of the contact point  $C$  with respect to the center of mass of the object  $O$ . Therefore, the relative velocity along the direction normal to the contact plane can be expressed as

$$v_r^+ = \mathbf{n}(\dot{\mathbf{r}}_p^+ - \dot{\mathbf{r}}_{oC}^+), \quad (4.15)$$

$$v_r^+ = \mathbf{n}(\mathbf{v}_p^+ - (\mathbf{v}_o^+ + \boldsymbol{\omega}_o^+ \times \mathbf{r}_{oC})), \quad (4.16)$$

Substituting Eq. 4.12, 4.13 and 4.14 into Eq. 4.16, and using Eq. 4.11, yields

$$j = \frac{-(e+1)v_r^-}{1/m_p + 1/m_o + \mathbf{n}((\mathbf{I}_o^{-1}(\mathbf{r}_{oC} \times \mathbf{n})) \times \mathbf{r}_{oC})}. \quad (4.17)$$

The velocities of two objects after contact can be achieved using the computed impulse  $j$  by Eq. 4.12 and Eq. 4.13.

#### 4.3.2. MULTIPLE CONTACTS ON ONE TARGET

A net contacting a target is normally a simultaneous multiple-contacts problem. The number of the contacts will also change at different step of simulation. The single target is suffering multiple contacts simultaneously and the further motion of the target results from those contacts. Coupling between contacts brings difficulties to the simultaneous multiple-contacts problem. Mirtich et al. concerns that the impulse-based method has a weakness on handling multiple and simultaneous contacts (Mirtich, 1996). Since the contact problem is usually between two objects, the simultaneous multiple contacts problem has rarely been discussed. This section provides an analytical solution to this

problem by decoupling each contact and establishing system equations to calculate the impulse on every contacting point. Based on the conservation law of momentum, the linear momentum and the angular momentum before and after contact shall be conserved

$$\begin{aligned} m_O \mathbf{v}_O^- + \sum(m_i \mathbf{v}_i^-) &= m_O \mathbf{v}_O^+ + \sum(m_i \mathbf{v}_i^+), \\ I_O(\boldsymbol{\omega}_O^+ - \boldsymbol{\omega}_O^-) &= \sum(\mathbf{r}_i \times j_i \mathbf{n}_i). \end{aligned} \quad (4.18)$$

where  $\mathbf{v}_i$  represents the velocity of the  $i$ th mass point. Let  $\mathbf{n}_i$  represent the normal direction of the contact plane,  $m_i$  represent the mass of the  $i$ th contact point, and  $j_i$  represent the magnitude of the impulse of the  $i$ th contact. Assume that  $k$  mass points simultaneously contact the tumbling object  $O$ . The velocity of the  $i$ th mass point after contact is

$$\mathbf{v}_i^+ = \mathbf{v}_i^- + j_i \mathbf{n}_i / m_i. \quad (4.19)$$

The linear and angular velocity of the target after contact are

$$\begin{aligned} \mathbf{v}_O^+ &= \mathbf{v}_O^- - (j_1 \mathbf{n}_1 + j_2 \mathbf{n}_2 + \cdots + j_k \mathbf{n}_k) / m_O \\ \boldsymbol{\omega}_O^+ &= \boldsymbol{\omega}_O^- - \mathbf{I}_O^{-1}(\mathbf{r}_1 \times j_1 \mathbf{n}_1 + \mathbf{r}_2 \times j_2 \mathbf{n}_2 + \cdots + \mathbf{r}_k \times j_k \mathbf{n}_k). \end{aligned} \quad (4.20)$$

In the above equation, the contact impulse vector  $\mathbf{j}$  is

$$\mathbf{j} = [j_1, j_2, \cdots, j_k]^T. \quad (4.21)$$

an undetermined vector.

To simplify the expression, we define the normal vector  $\mathbf{N}$  as

$$\mathbf{N} = [\mathbf{n}_1, \mathbf{n}_2, \cdots, \mathbf{n}_k]^T, \quad (4.22)$$

and  $\boldsymbol{\Sigma}_{rk}$  is defined as the following expression

$$\boldsymbol{\Sigma}_{rk} = \sum_{i=1}^{i=k} \mathbf{r}_i \times j_i \mathbf{n}_i. \quad (4.23)$$

Therefore, Eq. 4.20 is can be written as

$$\begin{aligned} \mathbf{v}_O^+ &= \mathbf{v}_O^- - \mathbf{N}^T \mathbf{j} / m_O \\ \boldsymbol{\omega}_O^+ &= \boldsymbol{\omega}_O^- - \mathbf{I}_O^{-1} \boldsymbol{\Sigma}_{rk}. \end{aligned} \quad (4.24)$$

Based on the law of impulse conservation and introducing the coefficient of restitution  $e$ , relative velocities after contact in the direction normal to the contact plane can be derived as

$$\begin{aligned} -(e+1)v_{r1}^- &= \mathbf{n}_1 [j_1 \mathbf{n}_1 / m_1 + \mathbf{N}^T \mathbf{j} / m_O + (\mathbf{I}_O^{-1} \boldsymbol{\Sigma}_{rk}) \times \mathbf{r}_1] \\ -(e+1)v_{r2}^- &= \mathbf{n}_2 [j_2 \mathbf{n}_2 / m_2 + \mathbf{N}^T \mathbf{j} / m_O + (\mathbf{I}_O^{-1} \boldsymbol{\Sigma}_{rk}) \times \mathbf{r}_2] \\ &\quad \dots \\ -(e+1)v_{rk}^- &= \mathbf{n}_k [j_k \mathbf{n}_k / m_k + \mathbf{N}^T \mathbf{j} / m_O + (\mathbf{I}_O^{-1} \boldsymbol{\Sigma}_{rk}) \times \mathbf{r}_k]. \end{aligned} \quad (4.25)$$

On the left side, the expression can be reformulated using the vector notation  $\mathbf{v}$ ,

$$\mathbf{v} = -(e+1)[v_{r1}^-, v_{r2}^-, \cdots, v_{rk}^-]^T. \quad (4.26)$$

To further simplify the expression of Eq. 4.25, we define

$$\mathbf{IC}_{ijk} = (\mathbf{I}_O^{-1}(\mathbf{r}_i \times \mathbf{n}_j)) \times \mathbf{r}_k. \quad (4.27)$$

Thus, the coefficient matrix  $\mathbf{M}$  is derived from Eq. 4.25,

$$\mathbf{M} = \begin{bmatrix} \frac{1}{m_1} + \frac{1}{m_O} + \mathbf{n}_1 \mathbf{IC}_{111} & \frac{\mathbf{n}_1 \mathbf{n}_2}{m_O} + \mathbf{n}_1 \mathbf{IC}_{221} & \cdots & \frac{\mathbf{n}_1 \mathbf{n}_k}{m_O} + \mathbf{n}_1 \mathbf{IC}_{kk1} \\ \frac{\mathbf{n}_2 \mathbf{n}_1}{m_O} + \mathbf{n}_2 \mathbf{IC}_{112} & \frac{1}{m_2} + \frac{1}{m_O} + \mathbf{n}_2 \mathbf{IC}_{222} & \cdots & \frac{\mathbf{n}_2 \mathbf{n}_k}{m_O} + \mathbf{n}_2 \mathbf{IC}_{kk2} \\ \vdots & \vdots & \ddots & \vdots \\ \frac{\mathbf{n}_k \mathbf{n}_1}{m_O} + \mathbf{n}_k \mathbf{IC}_{11k} & \cdots & \cdots & \frac{1}{m_k} + \frac{1}{m_O} + \mathbf{n}_k \mathbf{IC}_{kkk} \end{bmatrix}. \quad (4.28)$$

Equation 4.25 can then be rewritten as

$$\mathbf{v} = \mathbf{M} \mathbf{j}. \quad (4.29)$$

Therefore, the impulse vector of every contact can be derived from

$$\mathbf{j} = \mathbf{M}^{-1} \mathbf{v}. \quad (4.30)$$

With a computed impulse of each contacting points  $\mathbf{j}$ , the velocities after contact can consequently be derived from Eq. 4.19 and 4.20.

#### 4.4. MODELING OF FLEXIBILITY

The mass-spring model is usually applied for net modeling by discretizing cables into mass-spring elements. This model has a limitation in describing the flexibility of the cable between two mass points. Obviously, the flexibility between two mass points can be described by discretizing the cable into multiple segments as shown in Fig. 4.9. However, this dramatically increases the degrees of freedom and the complexity of the system equations. In addition, the mass-spring model has a limitation in describing the contact between a net and a target because the fictitious penetration of the massless spring-damping elements into the target's body cannot be avoided. The ANCF model has also been applied to model the net, and this model is able to describe the flexibility of the net. Moreover, the penetration between the cable elements and the target's body can be avoided by distributing fictitious contacting spheres on the cable element. Contacting spheres on one ANCF cable element can differ based on the requirements of accuracy and computational performance. In other words, the contacting spheres can be several spherical points (Fig. 4.10 (a), (b)) distributed along the centreline of a cable element, or even a chain of spheres (Fig. 4.10 (c)). The segment between contacting spheres are not detected in a contact detection algorithm. Thus, penetration between the segment with the target might happen in that region. With increasing number of spheres, the computational time to evaluate the contact detection and the contact force will increase. On the other hand, the accuracy of the net motion might be enhanced and the penetration might be avoided.

However, the influence on the net dynamics by the flexibility modeling of a net is not well understood so far. For example, to express the flexibility of a cable using the mass-spring model, the number of mass points added on one cable element can be 2,

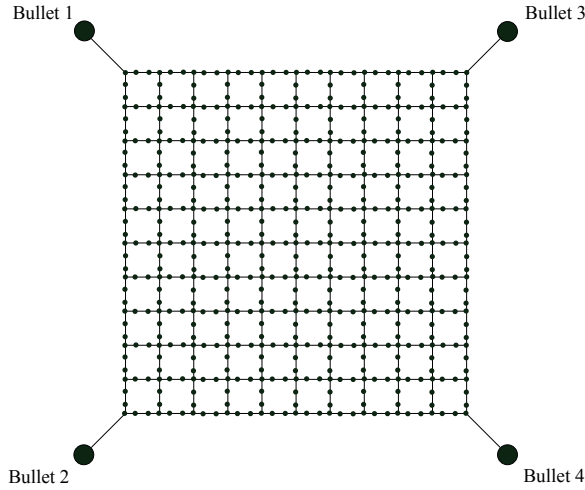


Figure 4.9: Flexibility modeling based on the mass-spring model.

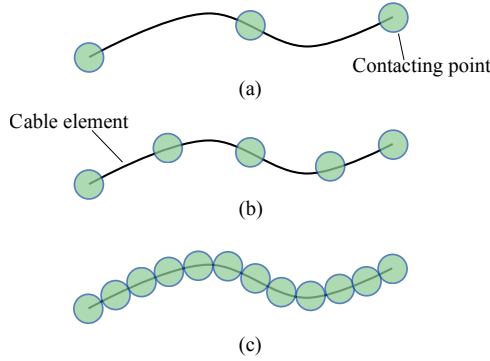


Figure 4.10: Contacting spheres on one cable element.

3 or even more (Fig. 4.9). How the net dynamics influenced by the number of those added mass points is unclear. In this section, the influence on the net dynamics by the flexibility modeling is investigated via simulations of capturing a ball and a cube shaped targets using the mass-spring model and the ANCF model.

The net deployment dynamics based on these two models have been introduced in Chapter 3. The net contact dynamics have been introduced in this chapter. The only thing needs to pay attention is, for the contacting spheres distributed on cable elements in the ANCF model, the contact force  $f_c$  needs to be converted to generalized force  $Q_c$  to fit the system equations based on the ANCF model. Using the principle of virtual work, the generalized contact force distributed on cable element is

$$Q_c = S(\xi_i) f_c. \quad (4.31)$$

with  $S$  being the shape function matrix of the cable element,  $\xi_i$  the element coordinates

Table 4.2: Simulation Parameters

	Parameter	Value
<b>Net</b>	Net size $A$ , [m <sup>2</sup> ]	0.64 × 0.64
	Mesh square $\square$ , [-]	6 × 6
	Mesh length $l_0$ , [m]	0.08
	Bullet mass $m_b$ , [kg]	0.05 × 4
	Shooting velocity $v$ , [m/s]	1.5
	Shooting angle $\theta$ , [°]	25
	Distance to the target $d_t$ , [m]	1
<b>Targets</b>	Cube length $a$ , [m]	0.12
	Ball radius $r$ , [m]	0.08

## 4

of the  $i$ th contacting sphere on the same cable element. Finally, implement  $f_c$  and  $Q_c$  into  $Q_b$  and  $Q_e$ , respectively in Eq. 3.16 to solve the system equations therefore to achieve the motion of the net with contacts.

To investigate the influence on the net dynamics by the flexibility modeling, simulations of capturing a ball and a cube shaped targets using the mass-spring model and the ANCF model are performed. The configurations of the net and the targets along with other simulation parameters are summarized in Table. 4.2. Figure 4.11 and 4.12 show the screenshots of simulations of the ball and the cube capturing based on the mass-spring model and the ANCF model. In both Fig. 4.11 and 4.12, (a) shows the simulation of the ball or the cube capturing based on the mass-spring without any added middle mass points on one cable element, (b) shows the simulation of the ball or the cube capturing based on the mass-spring with three middle mass points on one cable element, (c) shows the simulation of the ball or the cube capturing based on the ANCF model with three virtual contacting spheres on one cable element.

It can be clearly seen in the above figures that the penetration occurs when not applying the middle points, while adding three middle points on one cable element can effectively avoid the penetration. Since we have performed the ball and the cube capturing based on both models with different number of middle points on cable element, it would be interesting to compare those simulation results and analyze the influence of the flexibility modeling. We compare the trajectory of one of the bullets, (in this case we choose the bullet one, which is at the left up corner of the net) due to the symmetric configuration of the net. Figure 4.13 shows the bullet displacements along three axes, from which we notice that the bullet displacements under three cases (without middle points using the mass-spring model, with three middle points using the mass-spring model and with three contacting points using the ANCF model) are actually quite close to each other. The maximum difference is , and the relative difference comparing to the traveling distance of the net is , which indicates that the flexibility modeling has trivial influence on the net dynamics during capturing. Since adding more mass points in the mass-spring model or adding more contacting spheres on cable element in the ANCF model will better describe the flexibility of the net. However, it will also increase the degree of freedoms of the system or the contact detection effort. Moreover, since the

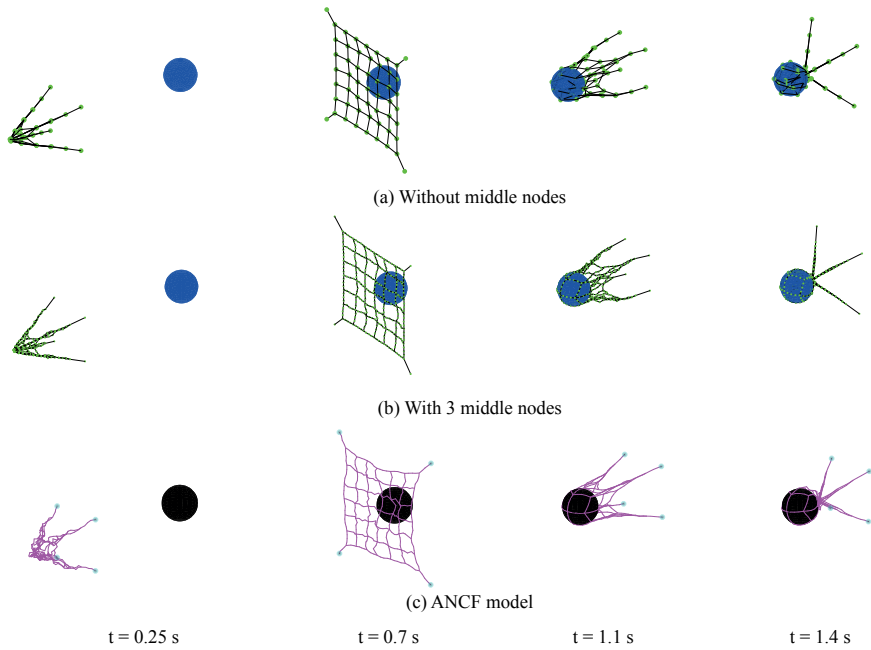


Figure 4.11: Ball capturing based on the mass-spring model and the ANCF model.

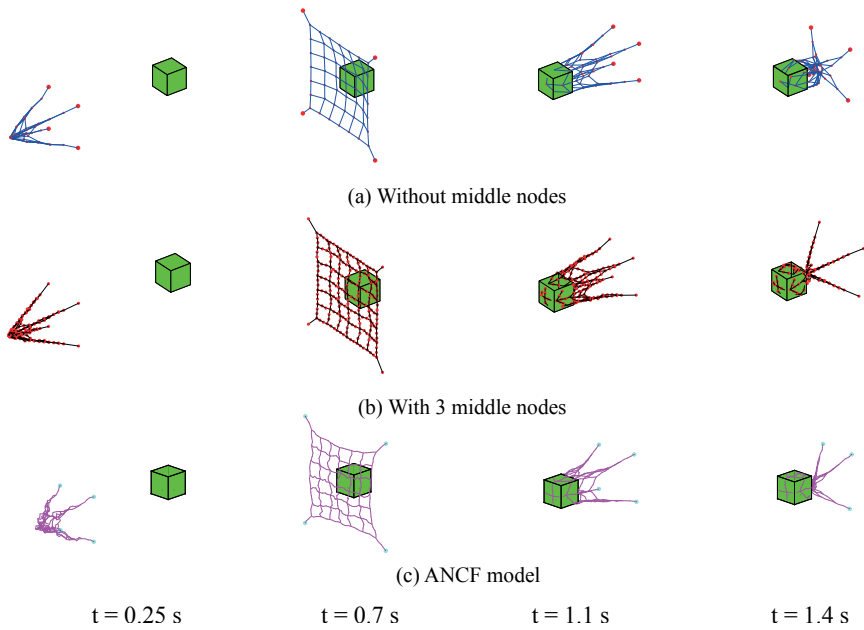


Figure 4.12: Cube capturing based on the mass-spring model and the ANCF model.

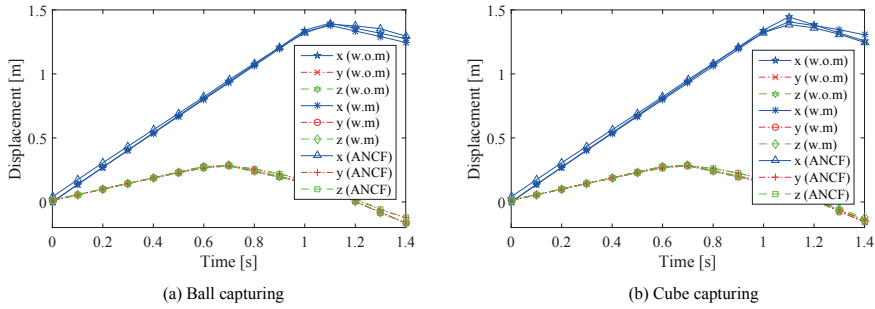


Figure 4.13: Bullet displacements of the ball and the cube capturing.

## 4

flexibility modeling actually has trivial influence on the dynamics of the net, the following studies are based on the mass-spring model without any middle mass points on a cable element.

### 4.5. VERIFICATION AND VALIDATION

We have derived the theoretical solutions of these two contact models. However, they have to be verified and experimentally validated. This section verifies and validates the models in two ways: by cross-verification and by experimental validation. The cross-verification of both methods is made by comparing the simulation results of the capturing of basic shaped targets, such as a cube, a ball and a cylinder. The validation of both models is made by comparing the simulation of the capturing of an Envisat mockup within a parabolic flight experiment introduced in Chapter 3.

#### 4.5.1. CROSS-VERIFICATION

In the cross-verification of two contact models, the capturing of basic shaped targets based on both models is simulated, compared and analyzed. Simulations are performed following the flowchart shown in Fig. 4.7. Since the number of contacts and positions of contacts might change at every step of simulation, contact detection has to be performed before calculating the contact responses. This section starts with introducing the contact detection algorithm.

#### CONTACT DETECTION

Contact detection needs to be performed at every step of the simulation such that a contact can immediately be detected once it occurs. The contact detection algorithm introduced in this chapter is based on the Axis-Aligned Bounding Box (AABB) method. The bounding box is the box with the smallest measure (volume in this thesis) within which all the points on the target lie. In the AABB method, the bounding boxes are axis-aligned, which means the bounding boxes for each object are not orientation-dependent. They need not to be rotated in the inertial frame at every step of the simulation (Jiménez et al., 2001). Therefore, the AABB method has a good efficiency dealing with the contact detection. The contact detection algorithm is divided into two levels so as to improve the computational performance of the simulation. In the first level of the contact detec-

tion, the net and the target are assumed to be contained in the bounding box  $N$  and the bounding box  $T$ , respectively. The first level of contact detection is only performed between these two bounding boxes (Fig. 4.14 a). At the beginning of the net deployment, since the net is still away from the target, the first level of contact detection dominates the simulation to improve the computational performance. The second level of contact detection starts once the two bounding boxes intersect with each other (Fig. 4.14 b). In the second level of detection, every node of the net is checked for a contact with the target by calculating the distance  $d$  between the node and the target. Once the distance is smaller than a threshold distance  $\epsilon$ , a respective contact response will be applied on the node. The contact response depends on the chosen contact modeling method, namely, the penalty-based or the impulse-based method. In the penalty-based method, the contact force acting on the contact point will be calculated once a contact is detected. In the impulse-based method, the contact impulse and velocity change will be calculated. The new velocities will then be integrated to the dynamic equations of the net.

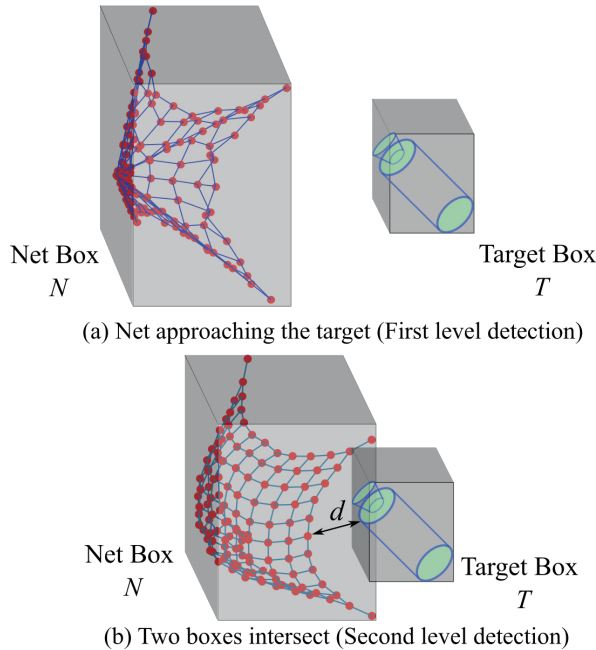


Figure 4.14: Sequence of contact detection.

#### SIMULATION

To cross-verify the two contact models, the capturing of various targets using both models are simulated, compared and analyzed in this section. Three basic shaped targets, namely, a cube, a ball and a cylinder without appendages are chosen so as to demonstrate the net's compatibility of different shaped targets. Moreover, it is also to make sure that both contact methods can be applied to different scenarios without loss of generality. The simulation parameters and the characteristics of the basic shapes of the targets

are summarized in Table 4.3. Simulations are performed in the local reference frame as shown in Fig. 3.7, and the targets are assumed to be massive enough that will not be affected by the contact force. Floating targets and tumbling targets capturing will be discussed in Chapter 5. Figures 4.15, 4.16 and 4.17 show screenshots of the cube, ball and cylinder capturing processes based on both contact models, respectively. The net capturing process includes the net deployment, net approaches to the target and target capturing. The simulations of the entire capturing process are verified using the momentum conservation law. Due to the similarity of the momentum and energy changing curves, only those of the cube capturing based on the impulse-based model are provided as shown in Fig. 4.18. The momentum is always conserved since the external forces, such as micro-gravity and other disturbances on the net and the target are not taken into account in the simulation. The mechanical energy of the system, which is the sum of the kinetic and elastic energy, decreases slightly at the beginning of the net deployment phase due to the damping of the net. At the moments of contacting, such as around 0.8 s, 1.2 s and 1.5 s, the mechanical energy drops due to the energy loss by contacts. After the moment around 1.5 s, the mechanical energy drops dramatically since the net is wrapping the target from that moment, and the contacts are keeping ongoing and dissipating the energy. The contact response is either contact force or contact impulse that depends on the chosen contact model. Figure 4.19 shows the contact responses of these three scenarios. The peaks of the maximum contact force or impulse occur when there is a status changing due to the contact. As shown in Fig. 4.19, the time of contacts are quite close to each other for the two models. However, the trends of the maximum contact force and the impulse can not be exactly the same since the number of contacts and the contacting points are not the same at every step of simulations. Comparing Fig. 4.19 with Fig. 4.18 (b), it is found that the time of peaks corresponds to each other. Qualitatively speaking, it is noticed that the net configurations obtained by two contact models are close to each other in every step of the capturing. Those findings indicate that the two contact models are both able to describe the contacts dynamics of net capturing. They have a good agreement with each other. In the following section, simulation results are compared quantitatively.

#### COMPARISON

To quantitatively compare the two contact models, trajectory differences of typical knots on the net are collected and compared. We chose to compare the trajectories of the four bullets since the bullets are able to describe the general configuration of the net to some extent. The trajectory differences of those four bullets in three scenarios are reported in Fig. 4.20 using boxplots. The definitions of the markers in this boxplot figure have been introduced in Section 3.5.2. It is noticed that the maximum differences of some bullets in the cube capturing scenario are larger than those of the other two scenarios. This is caused by the uneven shape of the target. Nevertheless, the median of the distributed data of the trajectory differences are all below 0.01 m, and all the average differences are below 0.04 m. The mean value of the average differences in three scenarios are 0.01 m, 0.009 m, 0.002 m, respectively. Comparing with the travelling distance of the net, the differences between the penalty-based and the impulse-based method are 1%, 0.9%, and 0.2%, respectively, which indicates that the two contact models excellently agree with each other. The main difference of the two contact dynamic models is the way of coping

Table 4.3: Simulation Parameters

	Parameter	Value
<b>Net</b>	Net size $A$ , [m <sup>2</sup> ]	0.64×0.64
	Mesh square $\square$ , [-]	8 × 8
	Mesh length $l_0$ , [m]	0.08
	Bullet mass $m_b$ , [kg]	0.05×4
	Shooting velocity $v$ , [m/s]	1.5
	Shooting angle $\theta$ , [°]	25
	Distance to the target $d_t$ , [m]	1
	Simulation time $t$ , [s]	2
<b>Targets</b>	Cube length $a$ , [m]	0.16
	Ball radius $r$ , [m]	0.12
	Cylinder radius and length $r_c \times l_c$ , [m × m]	0.075 × 0.3

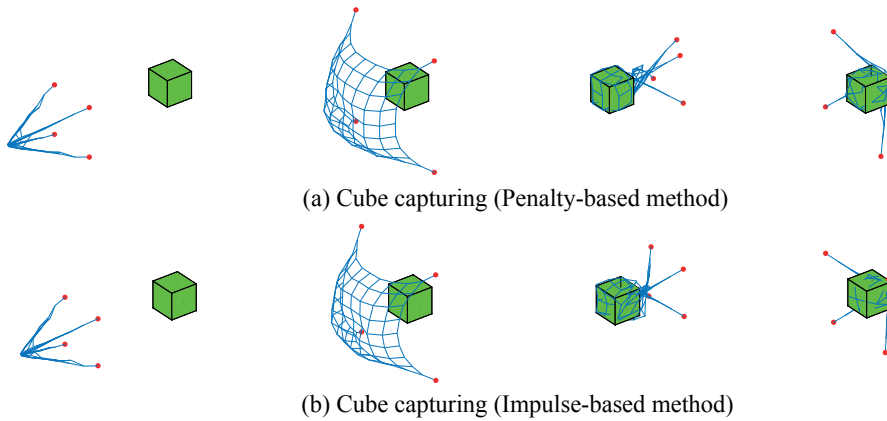


Figure 4.15: Cube capturing based on two contact models.

with the contact response. For the penalty-based method, the contact response is the contact force which depends on the fictitious penetration. On the contrary, the contact response in the impulse-based method is based on the impulse by the impact. In these two contact modeling methods, each method has its own strengths and weaknesses. For instance, for the penalty-based method, the contact force can be easily computed and it is better at coping with the simultaneous contacts, both from a programming point of view as well as from a theoretical point of view. However, in the penalty-based method, a large contact stiffness is needed to keep the penetration sufficiently small that will generate large forces leading to a stiff equation system. On the contrary, the impulse-based method is able to avoid the penetration and the stiff equations system. However, it requires a smaller step size when dealing with a small coefficient of restitution. In addition, when it comes to the simultaneous contacts, the impulse-based method is more complicated than the penalty-based method. In Table. 4.4, these two contact modeling methods are compared in different aspects.

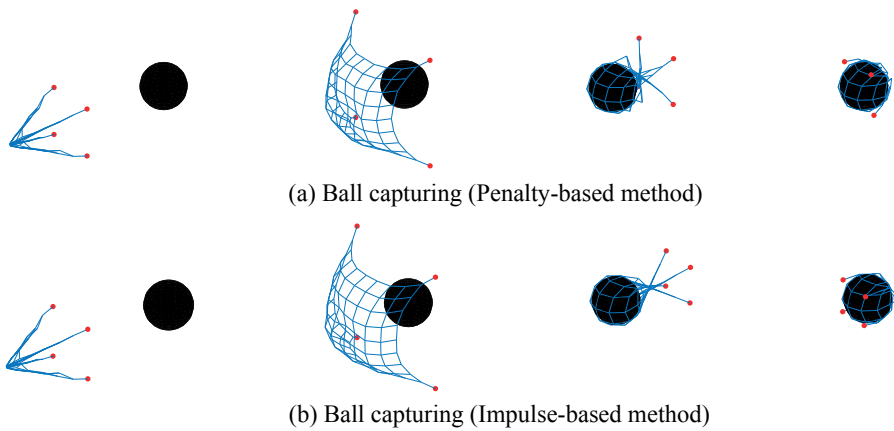


Figure 4.16: Ball capturing based on two contact models.

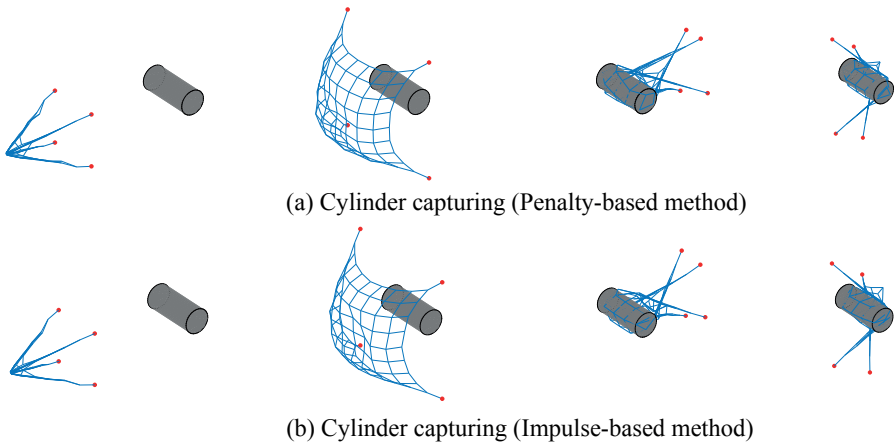


Figure 4.17: Cylinder capturing based on two contact models.

Table 4.4: Comparison of Two Contact Dynamic Models

	<b>Penalty-based Method</b>	<b>Impulse-based Method</b>
Contact response	Explicit contact force based on penetration	Collision impulse applied on contact bodies
Fictitious penetration	Yes	No
Differential equations	Stiff when the penalty is high	Non-stiff
Computational robustness	Fair	Good
Step size	Fair	Small
Handling of simultaneous contacts	Good	Fair

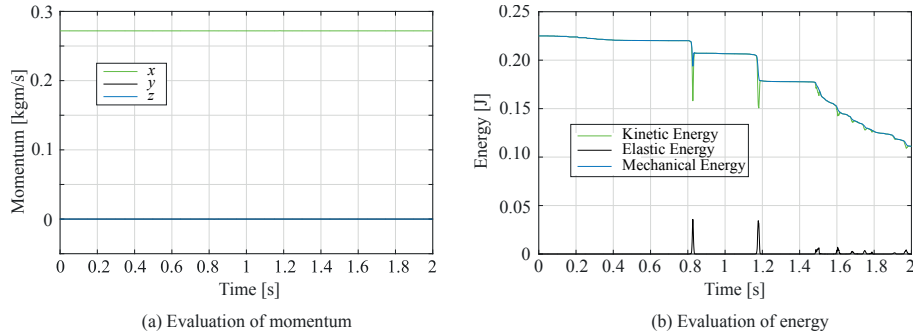


Figure 4.18: Momentum and energy of the cube capturing.

#### 4.5.2. VALIDATION BY PARABOLIC FLIGHT EXPERIMENT

The contact modeling methods introduced above allow to simulate the net capturing of space debris objects. However, the models have to be experimentally validated. To avoid the gravity influence, the experiment has to be performed in a micro-gravity environment, in this case, using a parabolic flight. This section presents the parabolic flight experiment and the validation of both contact models.

##### EXPERIMENT

The background and setup of this parabolic flight experiment have been partially introduced in Section 3.5.2. The parabolic flight experiment was led by SKA Polska under an ESA contract, and it was performed on board of a Falcon-20 airplane. The airplane used in the experiment is a business jet with the whole cabin available for zero-gravity experiments. The cabin dimensions are 4 m, 1.5 m and 1.6 m in length, width and height, respectively. Due to the geometrical constraint of the airplane, the experiment setup had to be down-scaled to fit the cabin. A net and an Envisat mockup are down-scaled by a factor of 25. The scaling leads to the net cable diameter a fraction of millimeter, which is almost invisible to the cameras. Therefore, the minimal diameter of the net cable is achieved based on the camera resolution and the distance to the cameras. Moreover, the scaling leads to the stiffness of net material not achievable for solid material, thus the closest existing material Nylon is chosen for the experiment. The Envisat mockup is firmly connected to a rig, with a net shot by a pneumatic net ejector to contact the target and embrace it. The key parameters of the parabolic flight experiment are summarized in Table 3.6. Since the experimental environment is not strictly gravity-free during the parabola, and the plane was rotating which generates the Coriolis effect on the net, accelerometers and gyroscopes had been equipped to measure the micro-gravity condition and the rotation rate of the airplane. The residual gravity and angular velocity recordings along three axes during the net deployment are shown in Fig. 3.20.

##### VALIDATION

In this section, the two contact models are validated by comparing the simulation of the Envisat mockup capturing with the above introduced experiment. As Fig. 4.21 shows, the shape of the Envisat mockup model is simplified to be composed of three cuboids,

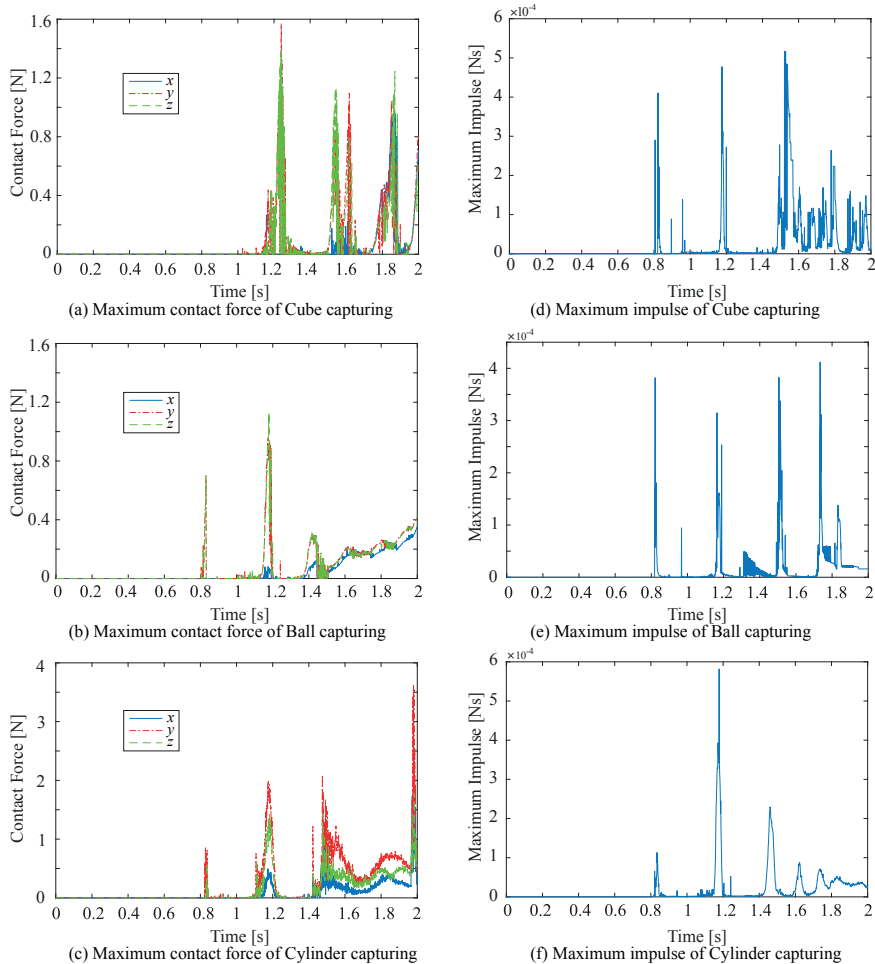


Figure 4.19: Contact responses of two contact modeling method: penalty-based method (left), impulse-based method (right).

one as the main body of the satellite, the thin and wide one as the solar panel and another one on the top of the main body as the synthetic aperture radar (SAR). The solar panel are connected with the main body of the satellite with a rod. Table 4.5 summarizes the dimensions of the Envisat mockup which have been down-scaled by a factor of 25. However, the thickness of the representations of the solar panel and the SAR are too thin to be detected as a contact with the mass points on the net. Therefore, their thicknesses are set as 0.05 m in the simulations.

The initial parameters such as the bullet mass, bullet velocity and shooting angle, etc. applied in the simulations are set the same as the parameters used in the parabolic flight experiment. The disturbances during the experiment are also taken into account in the simulations as described in Section 3.5.2. Figure 4.22 and 4.23 show the simulation

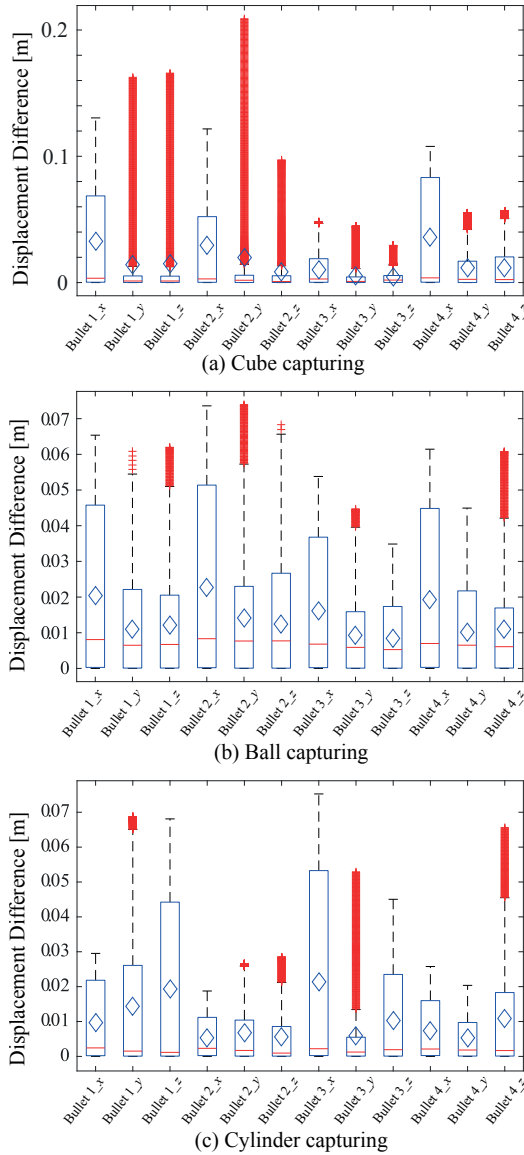


Figure 4.20: The trajectory differences of bullets in three scenarios.

screenshots of the net capturing process using the penalty-based and the impulse-based method, respectively. Since the shape of the Envisat mockup is more complex than the basic shapes introduced in Section 4.5.1, the number and positions of the contacting points at each step of simulation are not expected to be the same for the two contact models. This will accumulate the differences and lead to a systematic difference of the net configurations. The difference of the net configurations can be noticed when com-

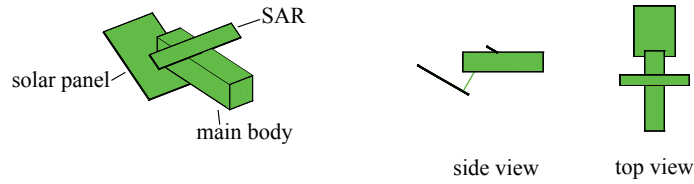


Figure 4.21: Envisat mockup.

Table 4.5: Dimensions of the Envisat mockup components

	Length × Width × Height [m]
<b>Satellite main body</b>	0.165 × 0.040 × 0.040
<b>Solar panel</b>	0.143 × 0.025 × 0.002
<b>SAR</b>	0.120 × 0.085 × 0.002

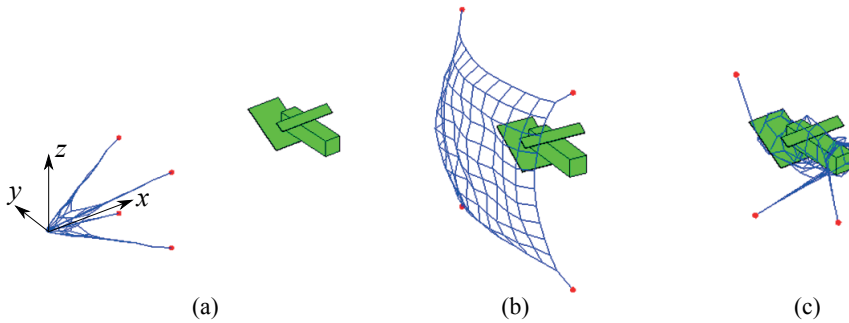


Figure 4.22: Simulation of the Envisat Mockup Capturing (Penalty-based Method).

paring these two figures. Because of this situation, the maximum contact responses, namely contact force or impulse of two models show that peaks occur at quite different moments as well (see Fig. 4.24).

With the simulations obtained from both contact models, it is interesting to qualitatively compare the net configurations of the simulations with the experiment. Trajectories of four bullets are chosen to be compared since they are able to describe the general configuration of the net. As shown in Fig. 4.25, before 1 s, i.e., in the net deployment phase, the simulations have a good agreement with the experiment that have been verified in Chapter 3. At the beginning of the contact between 1 s to 2 s, the agreement continues. However, in the simulation, the link connecting the satellite and the solar panel is not considered in the contact detection algorithm. Moreover, the number and positions of the contacting points are not expected to be the same with the experiment all the time. This accumulates the error and leads to a poor agreement of the experiment and the simulation data in the final capturing stage between 2 s to 3 s, such as bullet 2 in  $y$ -direction and bullet 3 in  $z$ -direction. Except for that, the bullets trajectories obtained from the experiment and the simulation have a good agreement with each other. It is

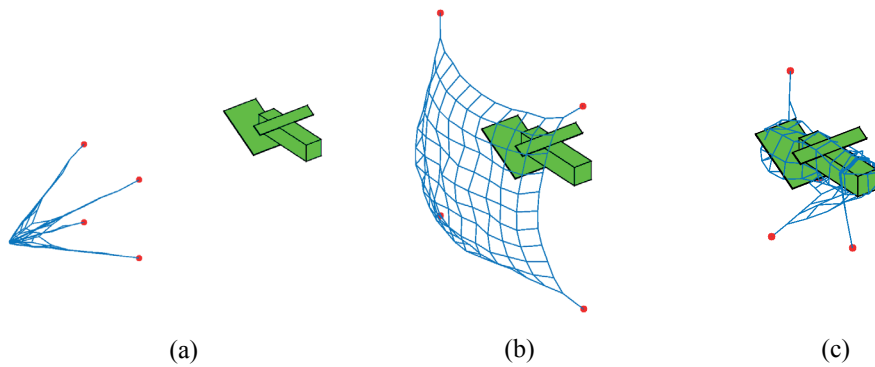


Figure 4.23: Simulation of the Envisat Mockup Capturing (Impulse-based Method).

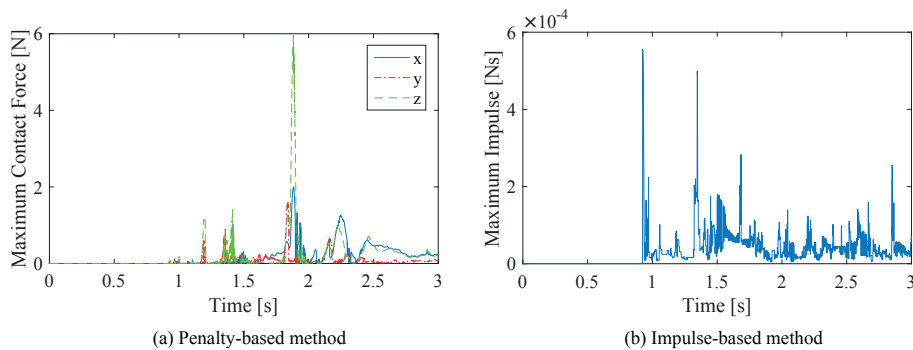


Figure 4.24: Maximum response under two contact models.

also noticed that the bullets trajectories from two simulations are always have a good agreement.

To further quantitatively analyze the difference of the simulation and the experiment, the displacement differences of these four bullets trajectories are obtained by taking the absolute value of the subtraction of the simulations results from the experimental results as shown in Fig. 4.26. This figure clearly shows that the higher and the maximum differences are distributed in the final stage of capturing. The differences can stem from either  $x$ ,  $y$ , or  $z$  direction which are random and can not be predicted. The distributions of the differences are shown with boxplots in Fig. 4.27. In Fig. 4.27, the diamonds in the boxes measure the average differences of the bullets trajectories. The lines in the boxes indicate the medians of each group of data. Higher whiskers represent the maximum values of the difference, and the lower whiskers represent the minimum. The sign '+' indicates an outlier. As shown in Fig. 4.27, apart from the outliers, the residual distributions are within 0.4 m. The average residuals of each bullet along each axis are within 0.2 m.

The residuals of two contact models along  $x$ ,  $y$ , and  $z$  are calculated and provided in Table 4.6. It is noticed that the residuals along each axis of the impulse-based method are

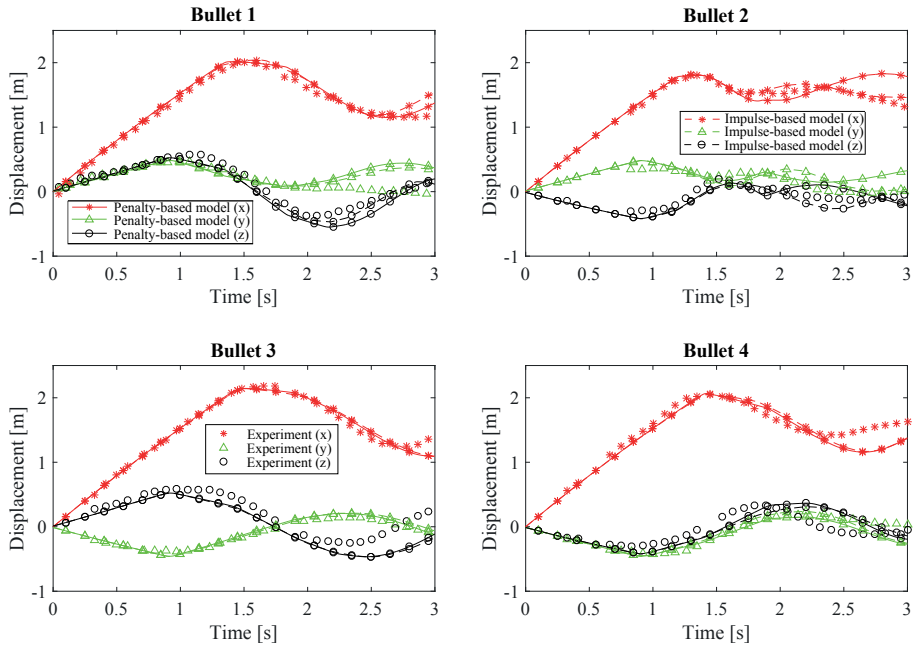


Figure 4.25: Bullets trajectories under simulation and experiment.

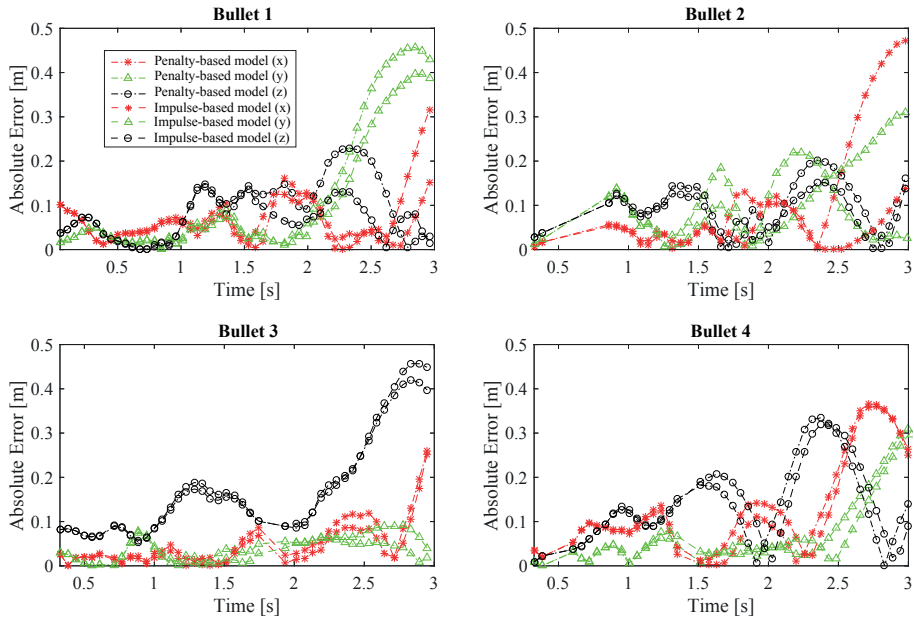


Figure 4.26: Bullets residuals under penalty-based method and impulse-based method.

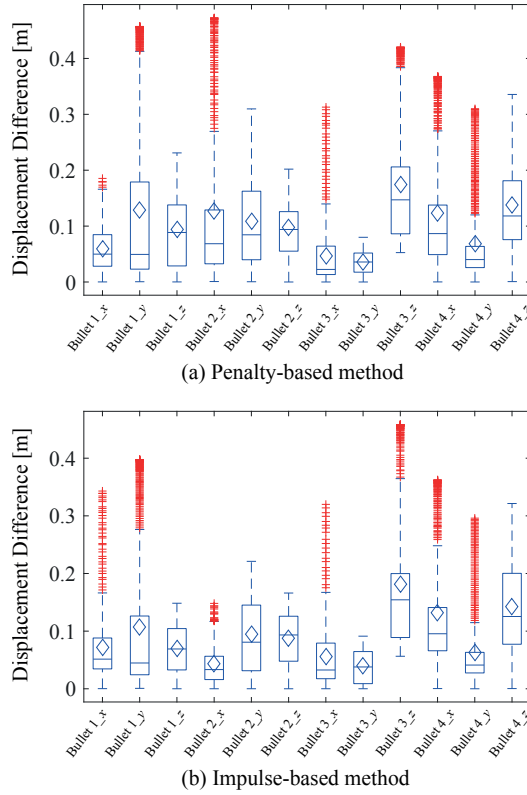


Figure 4.27: Difference of bullets trajectories between simulation and experiment.

all smaller than that of the penalty-based method. The average difference with the experiment are 10 cm and 9 cm, respectively. When comparing the average difference with the traveling distance of the net, the difference is restricted within 7%. This indicates that both contact models are able to simulate the net capturing of the Envisat mockup with a relative accuracy up to 7%, with the impulse-based method being slightly more accurate than the penalty-based method.

Table 4.6: Residuals of Two Contact Dynamic Models

	x [m]	y [m]	z [m]	Average [m]
<b>Penalty-based Method</b>	0.089	0.087	0.125	0.100
<b>Impulse-based Method</b>	0.075	0.076	0.120	0.090

## 4.6. SUMMARY

In the context of the net capturing for ADR, two contact modeling methods, the penalty-based method and the impulse-based method are introduced, compared and analyzed.

The penalty-based method is reviewed first, followed by the derivation of theoretical solutions of single and multiple contacts dynamics based on the impulse-based method. The impulse-based method is, for the first time, being used in a net capturing scenario. Numerical simulations of the capturing of basic shaped targets are performed to cross-verify the two contact models. These two models are further validated by the parabolic flight experiment of an Envisat mockup capturing. The comparison of the simulations based on two models with the parabolic flight experiment shows that the average difference between them is 7% when compared with the travelling distance of the net. Moreover, the impulse-based method is slightly more accurate than the penalty-based method. The results of the numerical simulations of the target capturing evaluate the effectiveness of the contact dynamic models. In addition, strengths and weaknesses of these two contact modeling methods are identified and compared. It is concluded that the impulse-based method is a suitable contact modeling method that can be used for the simulation of net capturing. Moreover, the impulse-based method is superior to the penalty-based method in the penetration avoidance and computational robustness. Due to multiple advantages of the impulse-based method with respect to the implementation and accuracy, the capturing of tumbling target will be only based on the impulse-based method in Chapter 5.

# 5

## CAPTURING OF TUMBLING TARGETS

---

Parts of this chapter have been published in Minghe Shan, Jian Guo, Eberhard Gill. *Tumbling Space Debris Removal Using a Net*, Journal of Guidance, Control and Dynamics (2017)

## 5.1. INTRODUCTION

The capturing of space debris objects belongs to the most crucial activities of active space debris removal. Space debris objects can have very different properties, such as size and shape or dynamical states. Space debris objects might be tumbling due to the residual angular momentum. This complicates the capturing. When using a robotic arm for capturing, attitude synchronization and/or de-tumbling must be performed before capturing so that the target is stable relative to the chaser. According to the research conducted by JAXA, objects with tumbling rates below  $3^\circ/\text{s}$  can be easily captured by a robotic arm; tumbling rates above  $30^\circ/\text{s}$  will hardly be treated using a robotic arm; tumbling rate between  $3\text{--}30^\circ/\text{s}$  can be de-tumbled using brush contact (Nishida and Kawamoto, 2011). Therefore, it is challenging to perform a tumbling target capturing using a robotic arm. The net capturing method is a candidate to overcome this defect due to its general compatibility with tumbling space debris. According to Retat and Bischof (2012), there is no need to perform attitude synchronization or de-tumbling using net capturing. However, the acceptable tumbling range of a target for net capturing is not yet fully understood. Moreover, a target is non-cooperative and its physical information, such as the orientation of the tumbling axis and the tumbling rate is typically not prior known. A net might be twined by a highly tumbling target, thus causing a failure of the capturing. Therefore, an acceptable tumbling range of a target and the way to treat a highly tumbling target need to be investigated.

### 5

Currently, extensive simulations on the space debris capturing using a net have been performed. Yang et al. (2017) have investigated the rotating and non-rotating net deployment dynamics, along with the analysis on the capturing simulation from different directions and the net-closing simulation. However, the target in this research is assumed to be fixed in space which means the target has zero degree of freedom in space. Botta et al. (2016a) have investigated the contact dynamics during capturing by applying a continuous compliant approach to the normal contact force modeling and a modified damped bristle model for the friction force modeling. A rocket upper stage which tumbles at a rate of  $5^\circ/\text{s}$ , is simulated to be captured by a net in this research. It is found that although the net wraps around the target, it opens again after a certain time due to the spinning of the target (Botta et al., 2016b). A necessity of a closing mechanism has been discussed, and a special closing system has been designed and tested by Sharf et al. (2017). The proposed net closing mechanism functions by extending the main tether connecting the chaser spacecraft and the net vertex to the perimeter and around the perimeter of the net, allowing the tether to actuate closure of the net in a manner similar to a cinch cord (Sharf et al., 2017). Benvenuto et al. have explored the contact dynamics of net capturing based on the penalty-based method. A cuboid shaped target and a coarse representation of the Envisat satellite tumbling at a rate of  $5^\circ/\text{s}$  are simulated to be captured with a net, respectively (Benvenuto et al., 2015, 2016). Two types of closing mechanisms have been proposed and simulated to ensure a successful capturing (Benvenuto et al., 2015). Gołębowski et al. have developed a simulator based on the Cossret rod theory and simulated the net contacting with a fixed Envisat mockup using the predictor-corrector algorithm (Gołębowski et al., 2015b). The net simulator and the contact algorithm have been validated by a parabolic flight experiment (Gołębowski et al., 2016).

However, the targets described in the existing researches are either fixed in space or tumbling at a low rate. The capturing of free-floating target, which is not controlled and moves freely in space, and acceptable tumbling rates of space debris objects for net capturing remain untouched. This chapter investigates the capturing of free-floating targets and tumbling targets based on the impulse method that has been validated by a comparison between the simulation and the parabolic flight experiment of a fixed Envisat mockup capturing in Chapter 4. Moreover, since a closing mechanism will increase the complexity of the capturing system, the range of tumbling rates avoiding a closing mechanism are studied and the stability of the system is discussed. However, it is found that a closing mechanism is still needed for highly tumbling targets to reduce the risk of slipping out of the net. Therefore, the final part of the chapter introduces a closing mechanism, that is designed and integrated to the net capturing system to ensure a successful capturing of targets with higher tumbling rates.

## 5.2. CAPTURING OF FREE-FLOATING TARGETS

To demonstrate the net's compatibility to different sizes and shapes of targets, targets investigated in this chapter vary in size and shape. Some typical targets are chosen: a 3-unit Cubesat without appendages, an upper stage of the Zenit-2 rocket and a coarse representation of the Envisat satellite. Figure 5.1 shows the three types of targets and the orientations of the local reference frame that are located at the center of the net container. The axes in the local reference frame are defined as: the  $X$ -axis is along the traveling direction; the  $Y$ -axis is orthogonal to the  $X$ -axis and pointing to the left side of the target, the  $Z$ -axis follows the right-hand rule and orthogonal to the  $X$ - and  $Y$ -axes. Following the same rule, the body reference frame  $o-xyz$  is attached on each target and located at the mass center of each target. The orientations of the body reference frame are also shown in Fig. 5.1. When shooting a net onto a target, the contact with the net might change the motion of the target. As discussed in Chapter 4, the impulse-based method has been validated by the parabolic flight experiment and its effectiveness has been demonstrated. Due to its multiple advantages over the penalty-based method, the impulse-based method is applied to investigate the capturing of free-floating and tumbling targets throughout this chapter. According to the parabolic flight experiment, the net can not be removed from the Envisat mockup without cutting it, which claims the effectiveness and the firmness of the net capturing (Gołębowski et al., 2016). Therefore, a successful capturing in the simulation is defined as when the net is able to close and fully embrace the target.

A space debris object is either free-floating or tumbling in space which depends on its residual angular momentum. A free-floating object refers to a target that is not controlled in space and has zero tumbling rate, and a tumbling object refers to an object that tumbles at a certain tumbling rate along its minimum or maximum inertial axis. Since the motion of a target might be changed by the contact impulse, e.g., pushed away by the net, it is necessary to investigate the influence of the contact during capturing to ensure a successful capturing. This section focuses on the net capturing of free-floating targets and aims to demonstrate the effectiveness of the net capturing by simulation. The motion change of the target based on the impulse method has been derived as shown in Eq. 4.20. The dimensions of the targets and the other simulation parameters are sum-

marised in Table. 5.1.

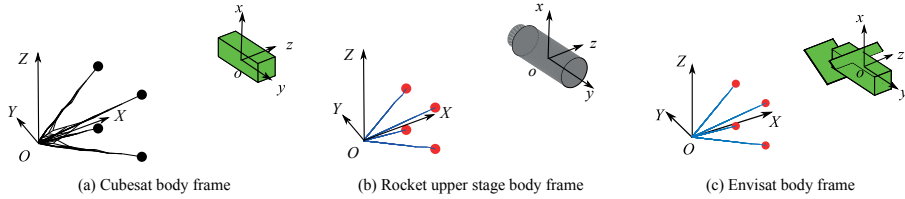


Figure 5.1: Reference frames of the targets.

Table 5.1: Parameters of Tumbling Targets Capturing

Parameters	Cubesat Capturing	Rocket Upper-Stage Capturing	Envisat Capturing
Dimensions , [m]	$0.1 \times 0.1 \times 0.3$	$3.9 \times 11.047$	$2.5 \times 2.5 \times 10$
Net size $A$ , [m <sup>2</sup> ]	$0.7 \times 0.7$	$30 \times 30$	$30 \times 30$
Mesh square , [-]	$10 \times 10$	$20 \times 20$	$20 \times 20$
Mesh length $l_0$ , [m]	0.07	1.5	1.5
Bullet mass $m_b$ , [kg]	$0.03 \times 4$	$1 \times 4$	$1 \times 4$
Shooting velocity $v$ , [m/s]	1.8	10	10
Shooting angle $\theta$ , [deg]	25	25	25
Distance to the target $d_t$ , [m]	1.3	35	35
Simulation time $t$ , [s]	3	10	15
Target mass $m_t$ , [kg]	3.5	8226	8000

### 5.2.1. FREE-FLOATING CUBESAT

An increasing number of launched Cubesats pose a threat to other operational satellites in space. Due to the small mass of the Cubesat, the risk of the net pushing the target away before closing the net is high. In this section, numerical simulations of capturing a 3-unit defunct Cubesat are performed to evaluate the effectiveness of the net capturing of a small free-floating target. Figure 5.2 shows screenshots of the capturing process under the simulation parameters summarized in Table 5.1. The simulation is performed in the reference frame shown in Fig. 5.1 (a). The local reference frame is centred at the centre of mass of the net container. This applies to the capturing of the other two targets that will be introduced in the next sections. The Cubesat is captured by a  $10 \times 10$  mesh squared net. The net is fully deployed around 0.8 s and then contacts with the Cubesat. After contacting, the four bullets first move towards each other, then pass by each other and surround the target which makes the net embracing and fully wrapping the target.

As previously introduced, there is a risk for capturing of a free-floating target since a net might push the target away before closing and therefore miss the target, especially for targets with small masses. In this case study, the motion of the Cubesat will be slightly affected by the momentum exchange during the net contacting. Figure 5.3 shows the translational motion of a free-floating Cubesat during capturing. According to the simulation, the maximum contact impulse acting on the target is as small as  $4 \times 10^{-4}$  Ns due to the lightness and low shooting velocity of the net that the target only moves less than 10 centimeters along the  $X$ -direction. It is found that, with a proper net configuration

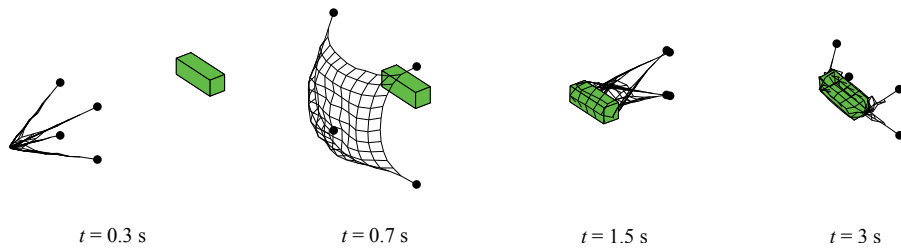


Figure 5.2: Screenshots of the capturing of free-floating Cubesat.

and shooting velocity, the net is able to close before pushing the target away and it will not lose the target. The changing of the momentum and the energy of the system is similar to what has been depicted in Fig. 4.18: the momentum of the system is conserved, and the mechanical energy of the system decreases due to the energy loss by contacts.

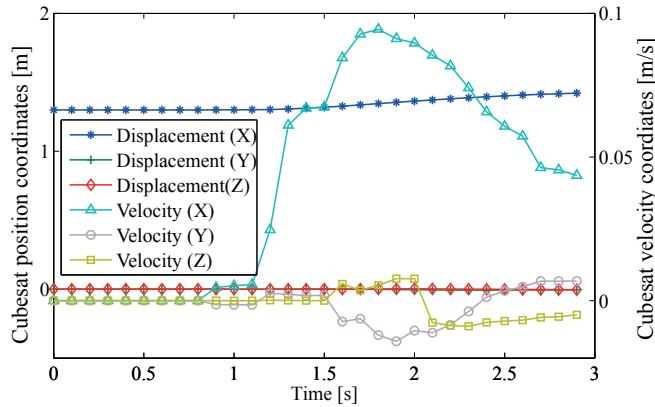


Figure 5.3: The motion of the Cubesat during capturing.

### 5.2.2. FREE-FLOATING ROCKET UPPER STAGE

Based on the analyses by [Bonnal et al. \(2013\)](#), [Liou et al. \(2010\)](#), and [Wiedemann et al. \(2012\)](#), rocket upper stages and the Envisat satellite are the most threatening targets among space debris objects. Therefore, they should be considered to be removed with high priority. In the list of the most threatening space debris objects summarized by [Wiedemann et al. \(2012\)](#) and [Van der Pas et al. \(2014\)](#), 20 out of 22 threatening objects are rocket upper stages. Among those rocket upper stages, 19 are the second stages of the rocket Zenit-2. Therefore, the second stage of the rocket Zenit-2, whose size is 3.9 m in diameter and about 11 m in length, is chosen as the target for net capturing throughout this chapter. To capture a free-floating rocket upper stage, the side length of a net should be larger than the perimeter of the target to ensure wrapping. Therefore the side length of the net is defined as 30 m in this case study. Figure 5.4 shows screenshots of capturing

process of the upper stage. According to the simulation, each bullet with the partial connected net forms an arm-shaped structure, and these four arm-shaped structures cross each other and embrace the target, ensuring a firm capturing. Due to the large mass of the upper stage, which is more than 8 tons, both translational and rotational movement are hardly affected by the net as shown in Fig. 5.5. Figure 5.5 (a) shows the displacements of the mass center of the target in three directions, which are almost immobile at its initial position. Figure 5.5 (b) shows the angular velocities of the target with respect to the local reference frame  $O - XYZ$ . Here, the value of the angular velocities are as small as  $10^{-4}$  rad/s which can be negligible. The peak of the curve occurs at the moment when the target suffers uneven contacts. Since the number and the positions of the contacts are not the same at every step of the simulation, the peak of the curve of angular velocity is not predictable.

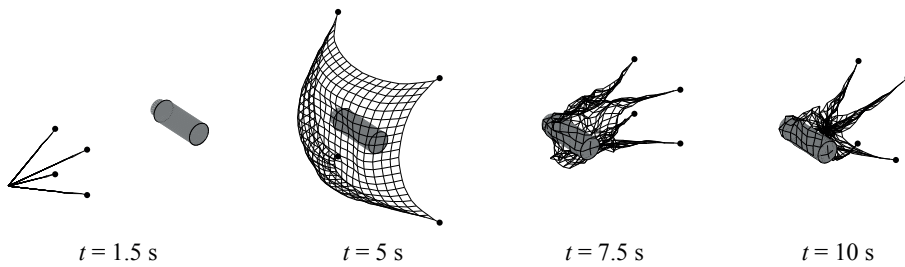


Figure 5.4: Screenshots of the capturing of free-floating rocket upper stage .

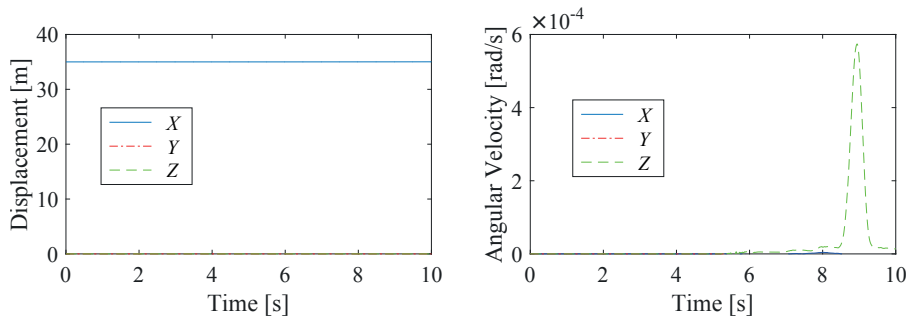


Figure 5.5: Displacement and angular velocity of the rocket upper stage during capturing.

### 5.2.3. FREE-FLOATING ENVISAT

Simulations on the capturing of the 3-unit Cubesat and the rocket upper stage demonstrate that net capturing is compatible to different sizes of the targets. However, the shapes of these targets are regular as cuboid and cylinder-like, respectively. This section considers appendages of the target object, such as the solar panel or the antenna, in the simulation. Envisat is one of the most threatening space debris objects as previously discussed. Its main body is also cuboid-shaped with dimension  $2.5 \times 2.5 \times 10$  m. The external solar panel is aligned besides the main body and connected with it by a rod. The

coarse representation of Envisat is shown in Fig. 4.21. Figure 5.6 shows screenshots the capturing process of the free-floating Envisat. Those four arm-shaped structures cross each other and embrace the target then surround back the target with another round. Similar to the capturing of the rocket upper stage, the motion of Envisat is either hardly affected by the net due to its large mass. The successful capturing of the free-floating Envisat indicates that net capturing is also compatible to different shaped targets. In fact, the net capturing is more robust to irregularly shaped targets, such as satellites with appendages, since the net meshes would be hung up or wound on those appendages to prevent the target slipping off. This will also be discussed in Section 5.3.

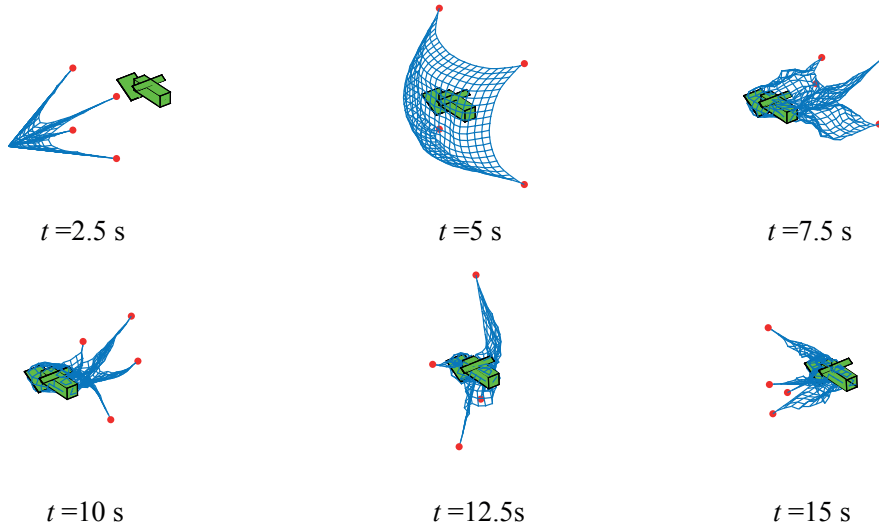


Figure 5.6: Screenshots of the capturing of free-floating Envisat.

### 5.3. CAPTURING OF TUMBLING TARGETS

Apart from the free-floating space debris objects, the targets might be tumbling at a certain rate due to their residual angular momentums. Highly tumbling targets may pose a risk of slipping out of the net, thus a failure of capturing. Moreover, acceptable tumbling rates of space debris objects where net capturing is successful are still not well understood. This section investigates the net capturing of tumbling targets. Three targets and the respective net configurations remain the same as those in the previous section as shown in Fig. 5.1 and Table 5.1.

#### 5.3.1. TUMBLING CUBESAT

Since a Cubesat has a small inertia and mass, its tumbling rate is higher than that of a larger target with the same residual momentum. Therefore, the investigation on the Cubesat capturing starts with a high tumbling rate. Assume that the 3-unit Cubesat is tumbling with an initial angular velocity, e.g., 1, 1.5 and 2 rad/s, respectively, along the  $x$ -axis in the body frame. Figure 5.1 shows the reference frames of the Cubesat capturing

system: the local reference frame  $O - XYZ$  and the body reference frame  $o - xyz$ . Figure 5.7 depicts the simulation processes of the capturing of the tumbling Cubesat with different initial angular velocities. It is noticed that when the target is tumbling too fast, e.g., 2 rad/s, the net configuration will be affected dramatically by the tumbling target. The net first tries to embrace the target, and then it will tumble with the target, re-open and miss the target. Eventually, it is not able to close and surround the target. This leads to a failed capturing according to what has been defined as successful capturing criteria. Therefore, based on the simulations, the suggested tumbling rate of a 3-unit Cubesat with net capturing is smaller than 1.5 rad/s.

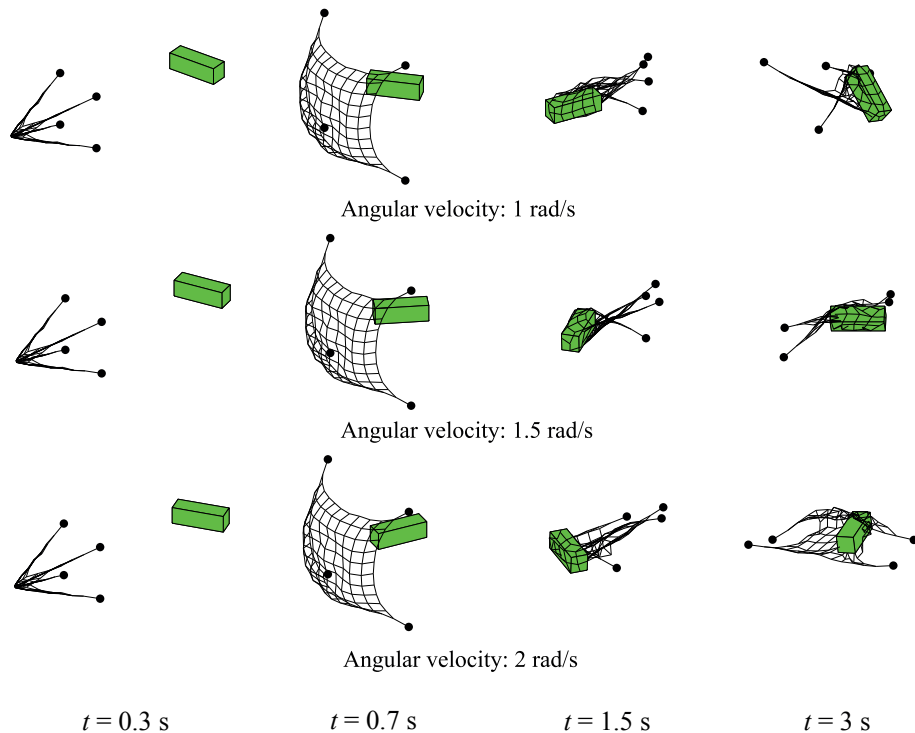


Figure 5.7: Cubesat capturing under different initial tumbling rates.

According to the simulations, the translational and rotational motion of the Cubesat will be slightly affected by the momentum exchange during the net contacting. Since the translational motions of the Cubesat under different initial angular velocities are similar to that of the free-floating Cubesat capturing, they are referred to Fig. 5.3 and no more repeatedly provided. Maximum impulse during contacting is given in Fig. 5.8. It is found that the maximum impulse is within  $3 \times 10^{-4}$  Ns. Moreover, the non-rotating Cubesat experiences a higher impulse at the first contact than the others, and the higher the initial angular velocity, the lower the impulse. This is because for the non-rotating Cubesat, the net contacts with the target directly along the normal to the surface of the target. However, for the rotating Cubesat, an angle is formed between the surface of the

target and the velocity of the mass points of the net. Therefore, the maximum impulse is calculated by the component of the velocity of the mass points along the normal of the surface of the target. Moreover, the higher the initial angular velocity, the larger the angles formed, thus the smaller the impulse exchanged. Fig. 5.9 shows the changes of the angular velocities of the target under different initial conditions. Due to the small momentum exchange, the tumbling rate will only be slightly affected by the net contacting. Specially, the tumbling rate along its main axis is decreased, that along the other two axes are raised. This indicates that the net surrounding process changes the target's initial status. However, since the number and the positions of the contacts are not the same at every step of the simulation, its tumbling status during capturing is complex, chaotic and unpredictable.

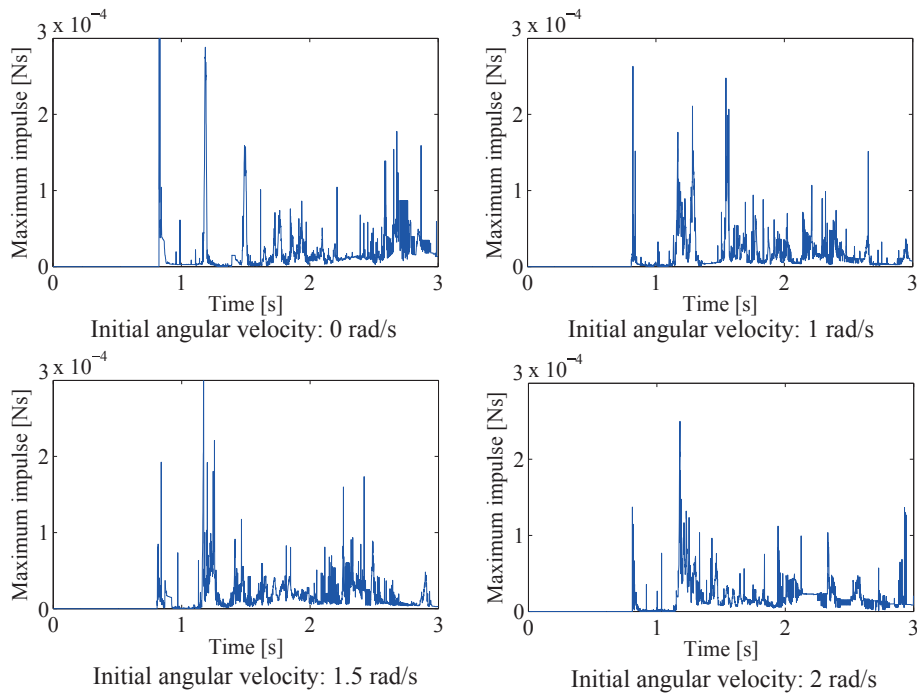


Figure 5.8: Maximum impulse of contacts during capturing.

### 5.3.2. TUMBLING ROCKET UPPER STAGE

As introduced in Section 5.2.2, 19 out of 22 most threatening objects are the second stages of the rocket Zenit-2 [Wiedemann et al. \(2012\)](#); [Van der Pas et al. \(2014\)](#). Due to its large inertia and mass, the tumbling rate of an upper stage is normally not very high. Therefore, this section investigates the capturing of tumbling upper stage starting with an initial angular velocity of 0.1 rad/s. The simulations of the upper stage capturing with an initial angular velocity, 0.1, 0.4, 0.7 rad/s, respectively, along the  $z$ -axis in the body frame that are presented in Fig. 5.10. The translational and rotational motion of the up-

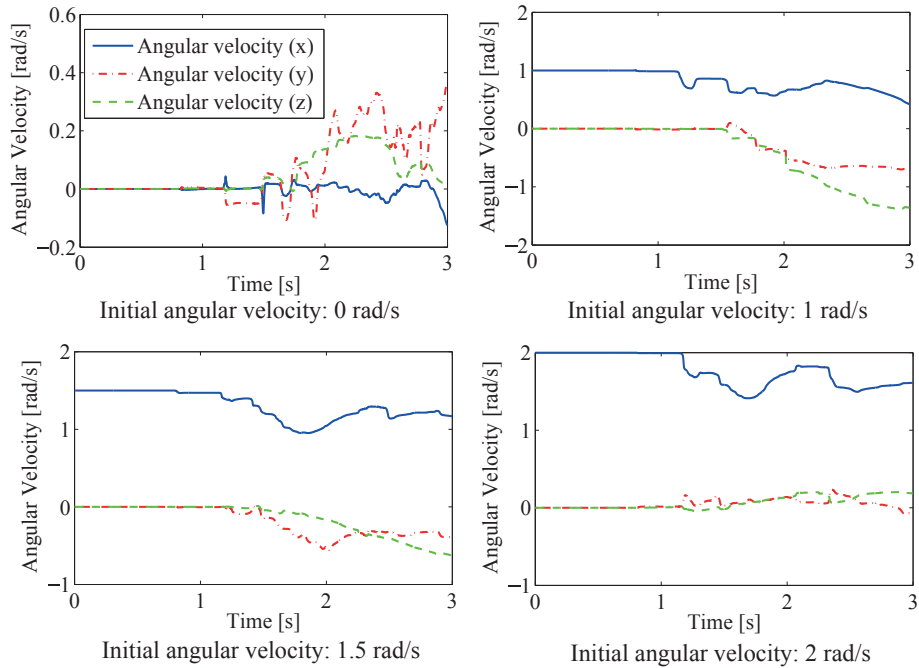


Figure 5.9: Angular velocity of the Cubesat during capturing.

per stage can hardly be affected due to its large inertia and mass and due to the lightness and low shooting velocity of the net. Each bullet with the connected partial net forms an arm-shaped structure. These four arm-shaped structures cross each other and embrace the target, thus ensuring a firm capturing. However, as the initial angular velocity increases, the net motion will be affected more significantly. Eventually, the net tumbles together with the target, and the arm-shaped structures are not able to cross and capture the target successfully.

This situation becomes worse when capturing the upper stage tumbling around the  $x$ -axis. The values of the initial angular velocity are set as 0.1, 0.4, 0.7 rad/s, respectively, as well. The simulations of the upper stage capturing with these initial angular velocities are presented in Fig. 5.11. It is noticed that the upper stage slips out of the net when its tumbling rate is as high as 0.7 rad/s. The free-throwing net, i.e., the net without a closing mechanism, is able to close and surround the upper stage when the tumbling rate is smaller than 0.7 rad/s. However, it is hard to make sure that the capturing is successful when the tumbling rate exceed 0.7 rad/s. Therefore, beyond that threshold, a closing mechanism is definitely needed to ensure a successful capturing.

### 5.3.3. TUMBLING ENVISAT

The Envisat satellite is the most widely discussed space debris object. It is tumbling with an approximate angular velocity of 0.1 rad/s. Figure 5.12 shows the screenshots of capturing of the tumbling Envisat with an initial angular velocity of 0.1 rad/s. These

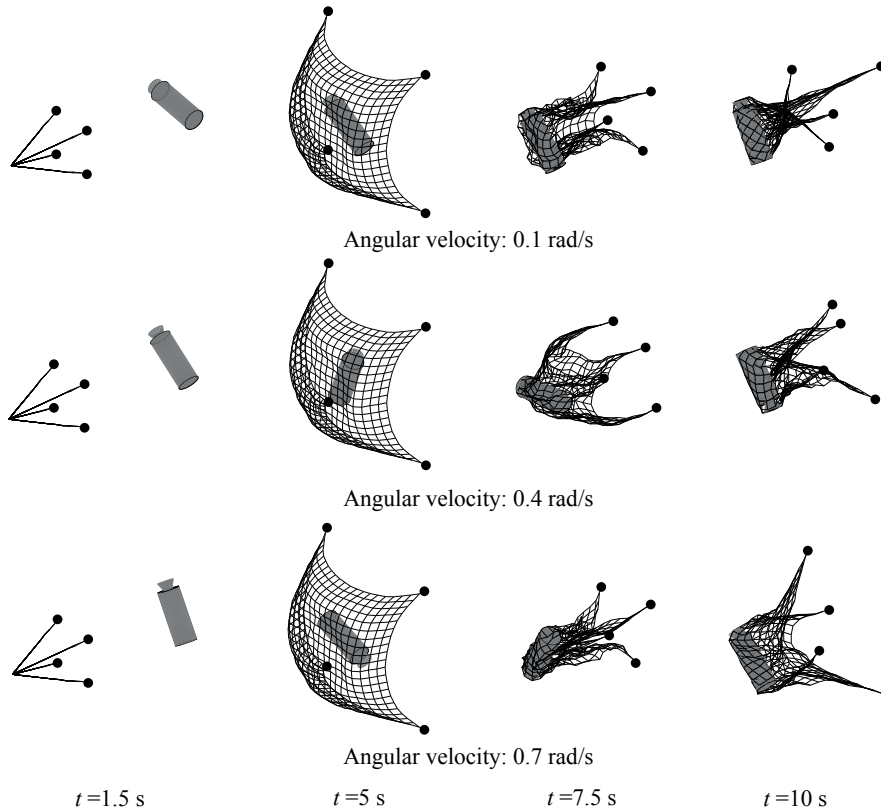


Figure 5.10: Capturing of rocket upper stage (tumbling along  $z$ -axis in body frame).

four arm-shaped structures cross each other and embrace the target then surround back the target with another round. Due to the existing of the appendages such as the solar panel and the radar antenna, parts of the net cables are wound around them, avoiding the target from slipping out of the net. Even when the initial angular velocity is as high as 1 rad/s (Fig. 5.13), the net is still able to surround the target without losing it. This indicates that the net capturing method is more robust to the irregularly shaped targets.

## 5.4. NET CLOSING SYSTEM

### 5.4.1. INTRODUCTION OF THE NET CLOSING MECHANISM

By analysing the net capturing of free-floating and tumbling targets, it is found that a free-throwing net without a net closing mechanism is able to successfully capture only free-floating targets and tumbling targets within a certain range of tumbling rates. For those target whose tumbling rates exceed that threshold, a closing mechanism is needed to ensure a successful capturing. The general idea of a net closing mechanism is to close the net mouth by a winch mechanism installed in each bullet. The closing mechanism

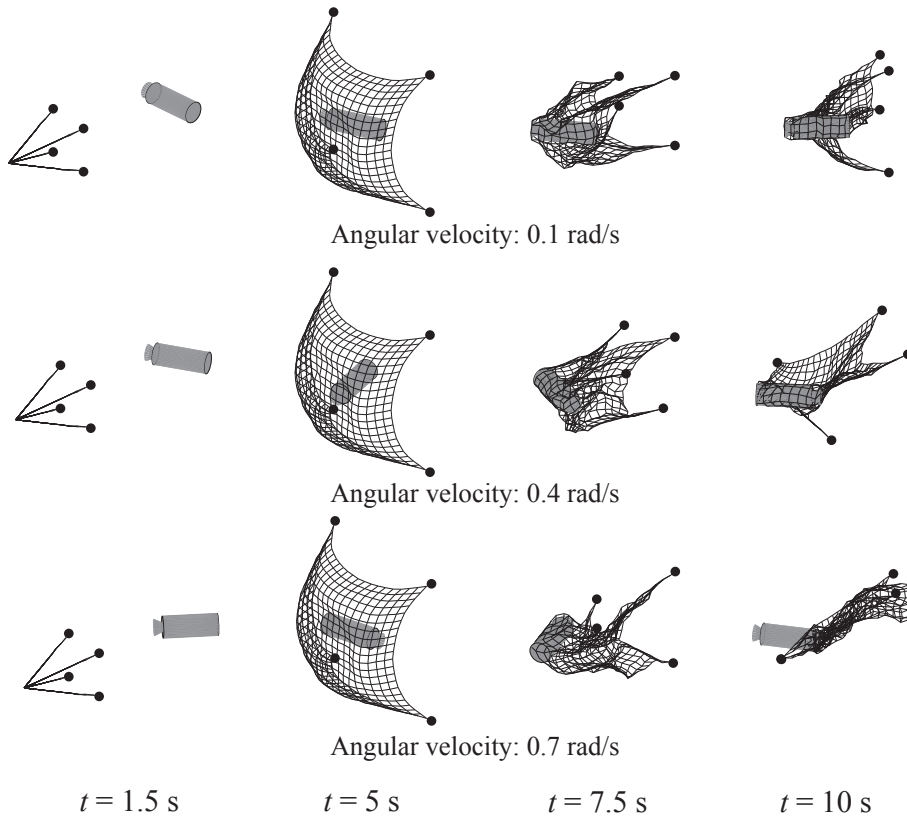


Figure 5.11: Capturing of rocket upper stage (tumbling along  $x$ -axis in body frame).

is initialized after the net contacting with the target, and the winches in the four bullets start to wind the cables interlaced with the net perimeter. This makes the four bullets move towards each other until the net closes. In this way, it is ensured that the target is not slipping off. [Benvenuto et al. \(2015\)](#) have proposed two types of closing mechanisms as shown in Fig. 5.14. In the first case, the closing thread is interlaced with the net perimeter, while in the second case the closing thread is only connected to bullets. Both types of closing mechanisms have been simulated and their effectiveness has been demonstrated by the simulations ([Benvenuto et al., 2015](#)). However, using either way, a gap will be formed by the net perimeters even when the bullets move close together. This brings uncertainties and reduces the reliability of the system. Another type of the net closing system has been designed and experimentally tested by [Sharf et al. \(2017\)](#). The idea of this design is to actuate the closure by towing the main tether connecting the chaser satellite to the net vertex, thus controlling the closure. According to [Sharf et al. \(2017\)](#), "the tether can function as a cinch cord by extending from the net center to the net perimeter, and then looping around the perimeter of the net, so that pulling on the tether will reduce the perimeter of the net mouth, thus securing the debris within the net". Figure 5.15 shows the concept design of this mechanism. The controllability of the

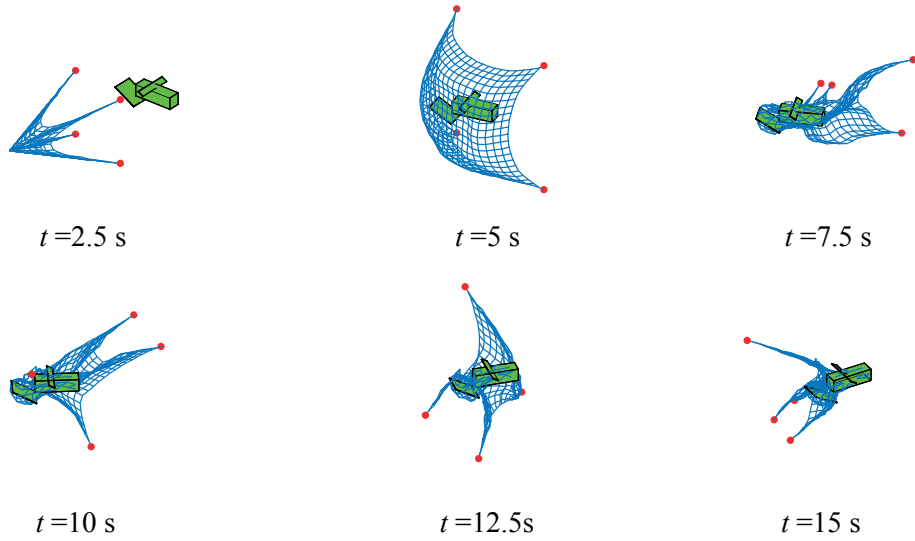


Figure 5.12: Capturing of tumbling Envisat (tumbling along  $x$ -axis in body frame,  $\omega_0 = 0.1$  rad/s).

5

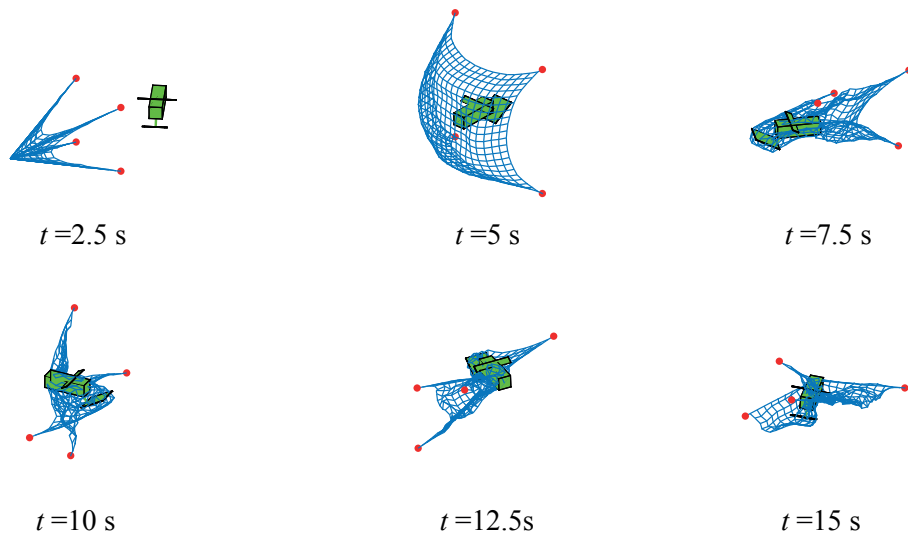


Figure 5.13: Capturing of tumbling Envisat (tumbling along  $x$ -axis in body frame,  $\omega_0 = 1$  rad/s).

closure makes this design more practical. However, it adds the complexity and therefore enhances the risk of failure of capturing to the system.

The design proposed in this research is based on the first type of the closing mechanism proposed by [Benvenuto et al. \(2015\)](#) (Fig. 5.14 (a)) due to its simplicity. However, instead of interlacing the closing thread with the net perimeter, we utilize flexible tubes as the net perimeter and let the closing thread run through inside the tube and then

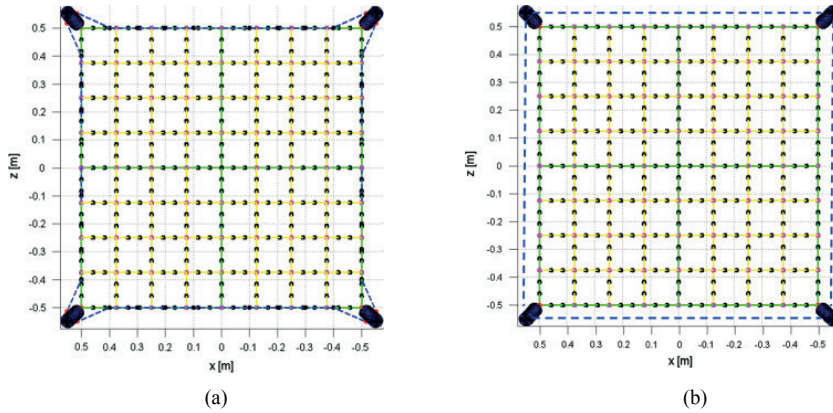


Figure 5.14: Two concepts of closing mechanism by [Benvenuto et al. \(2015\)](#). (a), interlaced thread closing. (b), free closing.

## 5

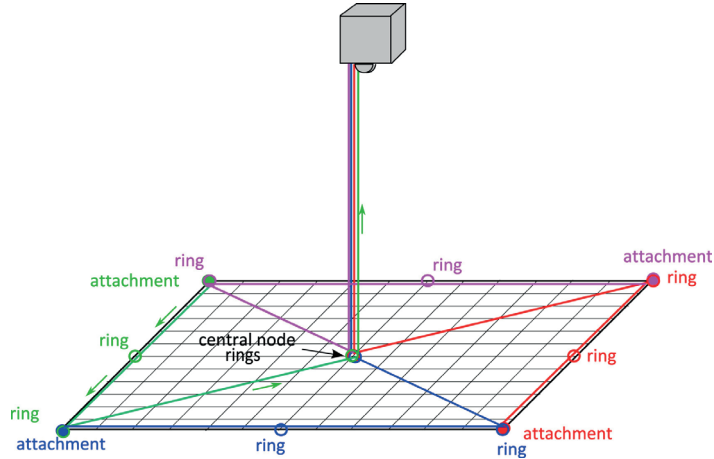


Figure 5.15: Concept of closing mechanism by [Sharf et al. \(2017\)](#).

connect to the winch inside the bullets. Net cables are knotted with the outside of the tube as well as the bullets. By triggering the winch inside the bullets once the contact is detected, the closing thread inside the tube will be wound in the bullets thus closing the mouth of the net in a manner similar to the cinch cord, and then secure the target within the net without any gap formed. Figure 5.16 shows the novel concept design of the closing mechanism.

#### 5.4.2. TARGETS CAPTURING WITH CLOSING MECHANISM

With a closing mechanism, net capturing can accommodate a wide range of different sizes, shapes and tumbling rates of the targets. This makes net capturing more powerful and reliable for ADR. This section demonstrates the effectiveness of the net closing

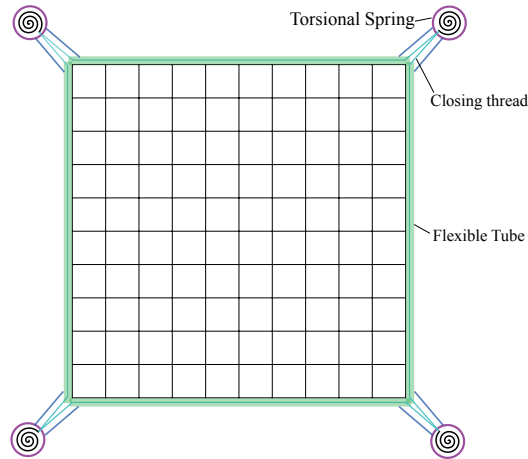


Figure 5.16: A novel concept of closing mechanism

mechanism by simulating the capturing of the same three targets with a higher tumbling rate. Figure 5.17 shows the capturing of the 3-unit Cubesat with a closing mechanism when its tumbling rate is as high as 2 rad/s, and tumbling around the  $x$ -axis in the body frame. The closing mechanism is triggered once the contact is detected. Four bullets start to move towards each other, and the knots at the net perimeter also move towards the bullets. This closure secures the target within the net even with a high tumbling rate. It also applies to the capturing of the target tumbling around the  $z$ -axis of the body frame as shown in Fig. 5.18.

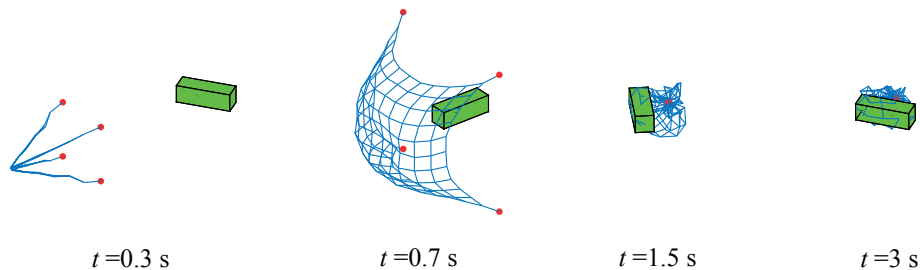


Figure 5.17: Capturing of Cubesat with closing mechanism (tumbling around the  $x$ -axis of the body frame,  $\omega_0 = 2$  rad/s).

Figure 5.19 shows the capturing of an upper stage with a closing mechanism when the tumbling rate is as high as 1.1 rad/s, which ends up with a firm and successful capture. It goes without saying that it also succeeds when the target is tumbling around  $z$ -direction as shown in Fig. 5.20.

The tumbling rate of the Envisat is assumed to be 0.5 rad/s. Figure 5.21 shows the capturing with closure. It clearly shows the net closing process from 5 s to 7.5 s.

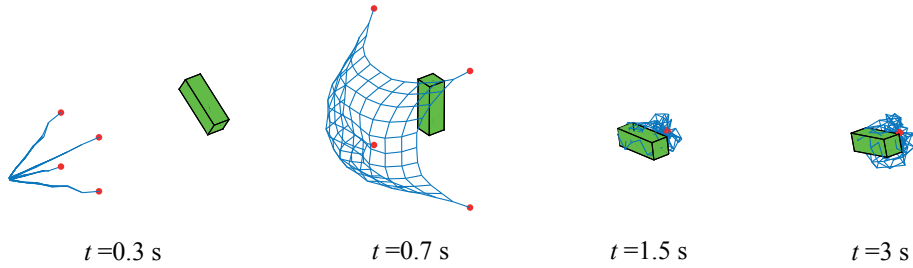


Figure 5.18: Capturing of Cubesat with closing mechanism (tumbling around the  $z$ -axis of the body frame,  $\omega_0 = 2 \text{ rad/s}$ ).

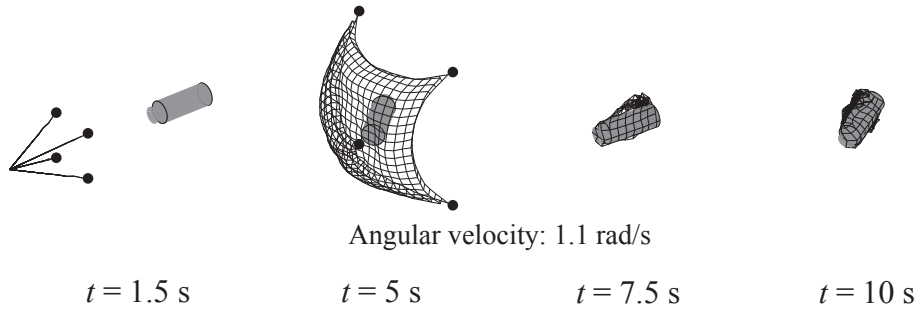


Figure 5.19: Capturing of upper stage with closing mechanism (tumbling around the  $x$ -axis of the body frame,  $\omega_0 = 1.1 \text{ rad/s}$ ).

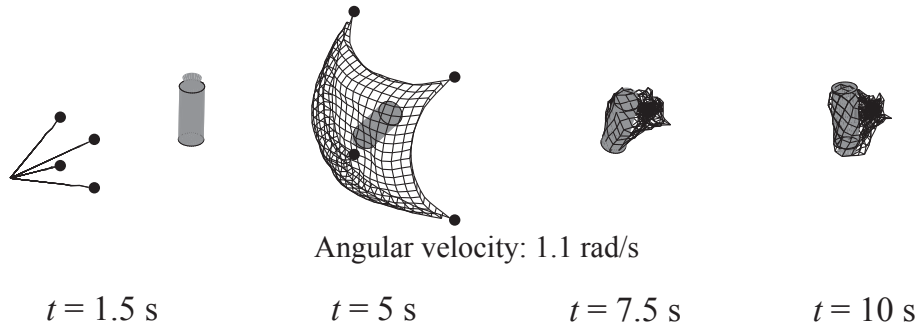


Figure 5.20: Capturing of upper stage with closing mechanism (tumbling around the  $z$ -axis of the body frame,  $\omega_0 = 1.1 \text{ rad/s}$ ).

## 5.5. SUMMARY

This chapter investigates the net capturing of free-floating targets and tumbling targets. The capturing is studied for three targets varying in size and shape: a 3-unit Cubesat without appendages, the second upper stage of the Zenit-2 rocket and a coarse representation of the Envisat satellite to demonstrate net's compatibility with different sizes and shapes of the targets. Simulation results show that, for the free-floating targets, the net is

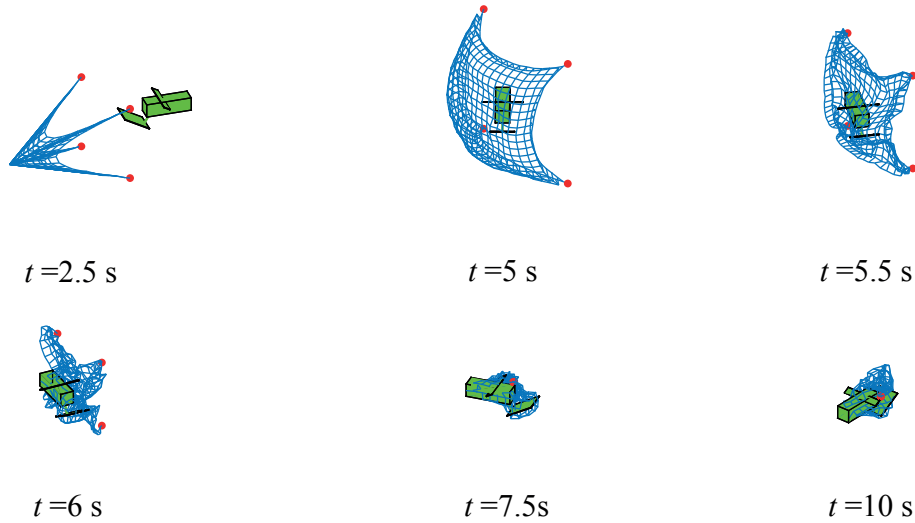


Figure 5.21: Capturing of Envisat with closing mechanism (tumbling around the  $x$ -axis of the body frame,  $\omega_0 = 0.5$  rad/s).

able to easily capture and surround the target without pushing them away. A tumbling Cubesat, with a specific net configuration, can be successfully captured when the tumbling rate is smaller than 2 rad/s. However, for rocket upper-stages, with a specific net configuration, they can be successfully captured only when the tumbling rate is smaller than 0.7 rad/s. Simulations of the tumbling Envisat with its appendages, such as a solar panel and a radar antenna, indicate that the net capturing method is more robust to irregularly shaped targets. Finally, a novel closing mechanism is proposed to ensure a successful capturing of the targets even with a higher tumbling rate. The effectiveness of the closing mechanism has been demonstrated by the simulations.



# 6

## CONCLUSION

## 6.1. SUMMARY

Space debris poses a big threat to operational satellites which form a crucial infrastructure for society and even to astronauts' lives. To mitigate the risk of collision and stabilize the space environment, active debris removal (ADR) is of great relevance. Many space debris capturing and removal methods have been proposed and net capturing is regarded as one of the most promising capturing methods due to its multiple advantages. For example, it allows a large distance between a chaser satellite and a target, so that close rendezvous and docking are not mandatory. It is furthermore compatible to different sizes, shapes and orbits of space debris. Additionally, it is flexible, lightweight and cost efficient. In this thesis, the dynamics of the net deployment and debris capturing along with the feasibility and reliability of capturing tumbling targets using a net were investigated and discussed. Research questions of this thesis were formulated as follows.

**RQ1. Which levels of non-cooperativeness of space debris exist? Which are their associated capturing and/or removal methods and what is the role the net capturing method plays among all those methods?**

**RQ2. What are the dynamic characteristics of the net capturing method?**

**RQ3. How to reliably capture a tumbling and non-cooperative debris object using the net capturing method?**

Chapter 2 was answering the first research question. Firstly, space debris objects were divided into three categories based on their properties, namely, non-operational satellites, rocket upper stages and fragments from collision or explosion. Furthermore, typical exemplary targets for each category have been provided. Methods for space debris capturing and removal have been, for the first time, reviewed and summarised. The advantages and drawbacks of the most relevant ADR methods have been addressed. A summary of the ADR methods has been made to clearly show their characteristics. Finally, tailored associated capturing and removal methods for each category of space debris objects have been proposed, which facilitates decision-making through these capturing and removal methods when dealing with different categories of targets. Based on the discussion, net capturing is considered as a promising method among others due to its compatibility to support capturing targets with various sizes and shapes, and less risk to generate more space debris objects.

In the second research question, the dynamic characteristics of net capturing include the deployment dynamics in the deployment phase and the contact dynamics during the capturing phase. Chapter 3 investigated the deployment dynamics of a net. Here, four critical parameters describing the deployment dynamic characteristics of the net, namely, the maximum area, the deployment time, the travelling distance and the effective period have been identified and defined. These parameters have been investigated by simulations under different initial input parameters, namely, the initial bullet velocity, the shooting angle and the bullet mass. Two modeling methods of a net, one based on the mass-spring model, the other based on the absolute nodal coordinates formulation (ANCF), were established and compared. A sensitivity analysis of the initial input parameters on the four critical parameters has been performed based on both models. Both models have been cross-verified, and validated using the results of a parabolic flight experiment. By analysing the absolute residuals and the average relative residu-

als between the simulations and the parabolic flight experiment results, it is concluded that both models are able to describe the motion of the bullets with an average relative residual error up to 15%.

Chapter 4 investigated the contact dynamics of net capturing. In this chapter, two contact modeling methods, the penalty-based and the impulse-based method have been introduced, compared and analyzed. The penalty-based method has been firstly reviewed and introduced followed by the derivation of the theoretical solutions of single and multiple contacts dynamics based on the impulse-based method. The impulse-based method is, to our knowledge, for the first time, being used in a net capturing scenario. Modeling methods of flexibility of a net have been proposed and analysed for the first time. It is found that modeling of flexibility has little influence on net deployment and contact dynamics. Furthermore, numerical simulations of basic shaped targets, a cube, a ball and a cylinder, have been performed to cross-verify the two contact models. These two models have been further validated by the parabolic flight experiment of an Envisat mockup capturing. The comparison shows that the average difference between the two models is limited to 7% when comparing with the travelling distance of the net. In addition, strengths and weaknesses of these two contact dynamic models have been identified and compared.

Chapter 5 was answering the third research question. It focused on the capturing of free-floating and tumbling space debris objects using a net. The capturing of three targets, varying in size and shape has been studied to demonstrate the net's compatibility to the targets. These targets are a 3-unit Cubesat without appendages, the second upper stage of the Zenit-2 rocket and the coarse representation of the Envisat satellite. For the free-floating targets, the net is able to capture and surround the target without pushing them away. For tumbling targets, simulation results have provided a threshold of the tumbling rate of the three targets that a free-throwing net is capable to capture: 0-1.5 rad/s for the Cubesat and 0-0.7 rad/s for the rocket upper stage. Finally, a concept of the closing mechanism has been proposed to ensure a successful capturing of the targets that with high tumbling rates. Furthermore, the effectiveness of the concept of the closing mechanism has been demonstrated by simulations.

## 6.2. CONCLUSIONS AND INNOVATIONS

The focus of this thesis is on the investigation of the deployment and contact dynamics of the net capturing method for ADR. The deployment dynamics has been studied using the mass-spring model and the ANCF model. The contact dynamics has been studied using the penalty and the impulse method. Moreover, both the deployment and the contact dynamics models have been verified and validated by a parabolic flight experiment. This section provides the conclusions and the main contributions of this thesis to the scientific body of knowledge throughout this thesis.

### 1. Evaluation of the net capturing method

To figure out the role that the net capturing method plays among existing ADR methods and to address the strengths and weaknesses of the net capturing method, ADR methods have been, for the first time, reviewed, summarised and compared. The advantages and drawbacks of the most relevant capturing and removal methods have been addressed as well. The state-of-the-art related to these methods were discussed in detail.

Space debris objects were divided into three main categories based on their properties. A tailored associated capturing and removal method for each category of space debris objects has been provided to facilitate decision-making through these ADR methods when dealing with different categories of targets. It is concluded that the net capturing is considered as a promising method among others due to its multiple advantages. For example, it allows a large distance between the chaser satellite and the target, such that close rendezvous and docking operations are not required. It is furthermore compatible to different sizes and shapes of space debris, which is compatible to almost all types of space debris objects. Additionally, the net is flexible, lightweight, cost efficient and less risky to generate more space debris.

### **2. Deployment dynamics investigation on the net capturing method**

The deployment dynamic characteristics of a net folded in a pattern proposed in this research called "inwards-folding scheme" have been investigated based on the mass-spring model and the ANCF model. Deployment dynamics of a net based on the ANCF model have been, for the first time, modeled, analysed and discussed in-depth. Besides, a sensitivity analysis of the initial input parameters with respect to the four critical parameters has been performed based on both models. It is concluded that a higher bullet mass, shooting angles and more flexible net material contribute to a larger net area. The net material has little influence on deployment time and travelling distance. Moreover, a higher initial bullet velocity and a larger shooting angle leads to a shorter effective period which in turn renders the capturing to be a higher risk of failure and of less reliability. The dependency of the output parameters on different initial input parameters has been provided quantitatively. Simulations based on the ANCF model have been performed and compared with the conventional mass-spring model. The results from both methods show a good agreement on changes of four critical parameters. The maximum differences between two methods are below 10% when comparing with the maximum difference except for the sensitive effective period. This indicates that the ANCF model is suitable to describe the deployment dynamics of a net. Furthermore, the ANCF model is more capable of describing the flexibility of the net with fewer nodes than the conventional mass-spring model. However, it is more computationally expensive. Based on the comparison of single-step computational time, the mass-spring model is almost 15 times faster than the ANCF model.

### **3. Contact dynamics investigation on the net capturing method**

Two contact modeling methods, the penalty-based and the impulse-based method have been compared and analyzed. For the first time, an analytical models of the single contact and the multiple contacts dynamics based on the impulse-based method have been derived. To our knowledge, the impulse-based method is, for the first time, being used in a net capturing scenario. Numerical simulations of targets with basic shapes, a cube, a ball and a cylinder, have been performed to cross-verify the two contact models. By comparing the simulation results based on both models, it is found that the medians of the distributed data of the bullets trajectory differences are all below 0.01 m. All the average differences are below 0.04 m. The mean value of the average differences in three scenarios are 0.01 m, 0.009 m, 0.002 m, respectively. Comparing with the travelling distance of the net, the differences between the penalty-based and the impulse-based method are 1%, 0.9%, and 0.2%, respectively, which indicates that the two contact mod-

els excellently agree with each other. By comparing the strengths and weaknesses of both contact dynamic models, it is concluded that the impulse-based method is superior to the penalty-based method with respect to the penetration avoidance and computational robustness. Furthermore, the flexibility modeling of a net has been established, analysed and discussed for the first time. To investigate the influence of the flexibility modeling on the net dynamics, simulations of capturing of a ball and a cube shaped targets using the mass-spring model and the ANCF model have been performed. It is found that the modeling of the flexibility of a net for capturing space debris object has little influence on net deployment and contact dynamics.

#### 4. Validation by the parabolic flight experiment

A parabolic flight experiment has been performed under ESA contract which allows to compare the experimental results with the simulations of the net deployment phase and the net capturing phase. In the net deployment phase, simulation results based on both net modelling methods, the mass-spring model and the ANCF model have been, for the first time, compared with the experimental results. From the analysis of the absolute residuals and the average relative residuals between the simulations and results of the parabolic flight experiment, it is concluded that both models are able to describe the motion of the bullets and the net along the traveling direction with an average relative residual error up to 15%. Moreover, the mass-spring model is superior in describing the motions of bullets along the traveling direction as compared to the ANCF model. On the contrary, the ANCF model is superior to the mass-spring model in describing the dynamics of the inner knots of the net. In the net capturing phase, both contact models, the penalty-based method and the impulse-based method, have been validated by the parabolic flight experiment of the capturing of an Envisat mockup. The comparison has shown that the average difference between the two models is limited to 7% when comparing with the travelling distance of the net. Moreover, the impulse-based method is slightly more accurate than the penalty-based method when comparing their average residuals.

**5. Net capturing of tumbling targets** As previously discussed, investigations on capturing and removing a tumbling space debris object with unknown physical properties remained untouched. With the validated net deployment model and the contact dynamic model, net capturing of free-floating targets and tumbling targets has been investigated for the first time. The net's compatibility to handle different sizes and shapes of the targets has been demonstrated by simulation results of the capturing of three types of targets varying in size and shape, namely, a 3-unit Cubesat without appendages, the simplified representation of the second upper stage of the Zenit-2 rocket and the Envisat satellite. Simulation results show that, for free-floating targets, the net is able to capture and surround the target without pushing it away. For a tumbling Cubesat, with a specific net configuration, it can be successfully captured when its tumbling rate is smaller than 1.5 rad/s. However, for the rocket upper-stage, with a specific net configuration, it can be successfully captured only when its tumbling rate is smaller than 0.7 rad/s. Simulation of the tumbling Envisat which has appendages such as a solar panel and a radar antenna indicates that the net capturing method is more robust to irregularly shaped targets than the regularly shaped targets such as upper stages of a rocket. Finally, a novel concept of a closing mechanism has been proposed and its effectiveness has been demonstrated to

ensure a successful capturing of the targets even with a higher tumbling rate.

### 6.3. RECOMMENDATIONS

In this thesis, contributions have been made to the scientific body of knowledge related to the dynamics of the net capturing for ADR. Even though the deployment and contact dynamics have been deeply investigated, some other interesting topics arose or remained untouched. Suggestions for future work research directions are addressed below.

#### 1. Influences of orbital dynamics

A simulator for a net capturing system has been developed in this thesis. However, the configuration of the net is assumed to be symmetric before shooting and the net is assumed to be deployed in a space environment without considering the perturbations by orbital dynamics. The perturbations on the net and the influences of orbital dynamics at the shooting moment and during the deployment need to be further investigated.

#### 2. Shooting influences on chaser satellite

When shooting a net from the chaser satellite, the motion of the chaser satellite will be changed based on the conservation of the momentum. The variations of shooting velocities of four bullets and/or the perturbations on the shooting angles will also affect the attitude of the chaser satellite. This influence on the chaser satellite might be significant, especially for those chaser satellites with small inertia and mass. Studies on the measurement of this influence and means to mitigate it are required.

#### 3. Post-capturing control

Following the net capturing, a composite system is formed by the chaser satellite, the target and the tether connecting them. The chaser satellite will pull the target to the disposal orbit only with this tether. This complex configuration introduces difficulties and uncertainties to the system, especially with a tumbling target, which might significantly disturb the trajectory and the attitude of the chaser satellite or even collide with the chaser satellite. Therefore, post-capture control and collision avoidance between the chaser satellite and the target needs to be performed.

#### 4. Experiment on net closing mechanism

In this thesis, an improved and novel net closing mechanism has been proposed based on the interlaced thread closing mechanism. The structural design of this new idea, including the selection of the tube material, the size and shape of the the winch inside the bullets and the knotting methods with the tube, needs to be performed. Moreover, the timing of the actuation needs to be further worked out. Finally, the manufacturing and experimental validation of the closing mechanism need to be performed.

#### 5. Contact detection between cables

In this thesis, contact detection between a net and a target is made at every step of the simulation. However, since the net cables are simplified as massless spring-damping elements, the contacts between cables are not detected. This introduces a problem of penetration between cables, thus rendering the net motion after embracing the target less trustworthy. Therefore, an efficient and effective way to detect the contacts between cables is required in the future.

## REFERENCES

- Aaron, P.  
2015. Orbital debris removal with gecko-like adhesives; technology development and mission design. In *66th International Astronautical Congress, Jerusalem, Israel*.
- Aghili, F.  
2008. Optimal control for robotic capturing and passivation of a tumbling satellite with unknown dynamics. In *AIAA Guidance, Navigation, and Control Conference and Exhibit*, volume 21, Pp. 2008–7274.
- Amend, J., E. Brown, N. Rodenberg, H. Jaeger, and H. Lipson  
2012. A positive pressure universal gripper based on the jamming of granular material. *Robotics, IEEE Transactions on*, 28(2):341–350.
- An, X., W. Lu, and Z. Ren  
2013. Compound control of attitude synchronization for autonomous docking to a tumbling satellite. *Applied Mechanics and Materials*, 394:470–476.
- Andrenucci, M., P. Pergola, and A. Ruggiero  
2011. Active removal of space debris-expanding foam application for active debris removal. *ESA Final Report*.
- Artsutanov, Y.  
1960. V kosmos na elektrovoze. *Komsomolskaya Pravda*, (contents described in *Lvov 1967 Science 158: 946*).
- Aslanov, V. and V. Yudintsev  
2013. Dynamics of large space debris removal using tethered space tug. *Acta Astronautica*, 91:149–156.
- Bender, J.  
2007. Impulse-based dynamic simulation in linear time. *Computer Animation and Virtual Worlds*, 18(4-5):225–233.
- Benvenuto, R. and R. Carta  
2013. Active debris removal system based on tethered-nets: experimental results. In *Proc. of 9th Pegasus-ALAA Student Conference, Politecnico di Milano, Italy*.
- Benvenuto, R., M. Lavagna, and S. Salvi  
2016. Multibody dynamics driving gnc and system design in tethered nets for active debris removal. *Advances in Space Research*, 58(1):45–63.

- Benvenuto, R., S. Salvi, and M. Lavagna  
2014. Dynamics analysis and gnc design of flexible systems for space debris active removal. In *Conference on Dynamics and Control of Space Systems (DYCOSS), Rome, Italy*.
- Benvenuto, R., S. Salvi, and M. Lavagna  
2015. Dynamics analysis and gnc design of flexible systems for space debris active removal. *Acta Astronautica*, 110:247–265.
- Berzeri, M. and A. A. Shabana  
2000. Development of simple models for the elastic forces in the absolute nodal coordinate formulation. *Journal of Sound and Vibration*, 235(4):539–565.
- Bess, T.  
1975. Mass distribution of orbiting man-made space debris. In *NASA Technical Note*.
- Bessonneau, J. and D. Marichal  
1998. Study of the dynamics of submerged supple nets (applications to trawls). *Ocean Engineering*, 25(7):563–583.
- Biesbroek, R.  
2012. The e. deorbit study in the concurrent design facility. In *Presentation handouts, Workshop on Active Space Debris Removal, Darmstadt, Germany*, volume 17.
- Billot, C., S. Ferraris, R. Rembala, F. Cacciatore, A. Tomassini, and R. Biesbroek  
2014. e.Deorbit: Feasibility study for an active debris removal. In *3rd European Workshop on Space Debris Modeling and Remediation, Paris, France*.
- Bischof, B., L. Kerstein, J. Starke, H. Guenther, and W. Foth  
2004. ROGER- robotic geostationary orbit restorer. *Science and Technology Series*, 109:183–193.
- Boge, T., T. Wimmer, O. Ma, and M. Zebenay  
2010. EPOS- a robotics-based hardware-in-the-loop simulator for simulating satellite RvD operations. In *Proceedings of the 10th international symposium on artificial intelligence, robotics and automation in space (iSAIRAS), Sapporo, Japan*, volume 29.
- Bombardelli, C. and J. Pelaez  
2011. Ion beam shepherd for contactless space debris removal. *Journal of Guidance, Control, and Dynamics*, 34(3):916–920.
- Bonnal, C., J. Ruault, and M. Desjean  
2013. Active debris removal: Recent progress and current trends. *Acta Astronautica*, 85:51–60.
- Borja, J. and D. Tun  
2006. Deorbit process using solar radiation force. *Journal of Spacecraft and Rockets*, 43(3):685–687.

- Botta, E., I. Sharf, and A. Misra  
2016a. Contact dynamics modeling and simulation of tether nets for space-debris capture. *Journal of Guidance, Control, and Dynamics*, Pp. 1–14.
- Botta, E., I. Sharf, A. Misra, and M. Teichmann  
2016b. On the simulation of tether-nets for space debris capture with vortex dynamics. *Acta Astronautica*, 123:91–102.
- Cai, J., P. Huang, and D. Wang  
2014. Novel dynamic template matching of visual servoing for tethered space robot. In *Information Science and Technology (ICIST), 2014 4th IEEE International Conference on, Shenzhen, China*, Pp. 389–392. IEEE.
- Cano, J. L., M. Hagenfeldt, and E. Deimos  
2014. Ion beam shepherd IOD mission (IBS-IOD). In *3rd European Workshop on Space Debris Modeling and Remediation, Paris, France*.
- Carter, J. and M. Greene  
1988. Deployment and retrieval simulation of a single tether satellite system. In *System Theory, 1988., Proceedings of the Twentieth Southeastern Symposium on, Charlotte, NC, USA*, Pp. 657–660. IEEE.
- Chang, B. and J. Colgate  
1997. Real-time impulse-based simulation of rigid body systems for haptic display. In *Proc. Symp. on Interactive 3D Graphics*, Pp. 200–209.
- Chen, Y., R. Huang, X. Ren, L. He, and Y. He  
2013. History of the tether concept and tether missions: a review. *ISRN Astronomy and Astrophysics*, 2013.
- Chiesa, A. and F. Alberto  
2014. Enabling technologies for active space debris removal : the CADET project. In *3rd European Workshop on Space Debris Modeling and Remediation, Paris, France*.
- De Jalon, J. and E. Bayo  
2012. *Kinematic and dynamic simulation of multibody systems: the real-time challenge*. Springer Science & Business Media.
- Debus, T. and S. Dougherty  
2009. Overview and performance of the front-end robotics enabling near-term demonstration (FRIEND) robotic arm. In *AIAA Aerospace Conference*, Pp. 1–12.
- Dong, X., Y. Li, Z. Zhang, L. Kong, and X. Wang  
2014. Research on the material and structure of space electrodynamic tether. In *40th COSPAR Scientific Assembly. Held 2-10 August 2014, in Moscow, Russia, Abstract G0. 3-16-14.*, volume 40, P. 3660.
- Dunn, M.  
2014. Space debris removal. US Patent 8,800,933.

- Ellery, A.  
1999. A robotics perspective on human spaceflight. *Earth, Moon, and Planets*, 87(3):173–190.
- Estes, R., E. Lorenzini, J. Sanmartin, J. Pelaez, M. Martinez-Sanchez, C. Johnson, and I. Vas  
2000. Bare tethers for electrodynamic spacecraft propulsion. *Journal of Spacecraft and Rockets*, 37(2):205–211.
- Flores, P. and H. Lankarani  
2016. *Contact force models for multibody dynamics*, volume 226. Springer.
- Flores-Abad, A., O. Ma, K. Pham, and S. Ulrich  
2014. A review of space robotics technologies for on-orbit servicing. *Progress in Aerospace Sciences*, 68:1–26.
- Forshaw, J.  
2014. Results of a system feasibility study on a heavy active debris removal mission. In *3rd European Workshop on Space Debris Modeling and Remediation, Paris, France*.
- Furuya, H., Y. Inoue, and T. Masuoka  
2005. Deployment characteristics of rotationally skew fold membrane for spinning solar sail. *AIAA*, 2045:1–10.
- Gao, S., Y. Yin, X. Sun, and Y. Sun  
2012. Dynamic simulation of fishing net based on Cubic B-Spline surface. In *AsiaSim 2012, Communications in Computer and Information Science*, Pp. 141–148. Springer Berlin Heidelberg.
- Gärdsback, M. and G. Tibert  
2009. Deployment control of spinning space webs. *Journal of Guidance, Control, and Dynamics*, 32(1):40–50.
- Gerstmayr, J. and A. A. Shabana  
2006. Analysis of thin beams and cables using the absolute nodal co-ordinate formulation. *Nonlinear Dynamics*, 45(1-2):109–130.
- Gilardi, G. and I. Sharf  
2002. Literature survey of contact dynamics modelling. *Mechanism and Machine Theory*, 37(10):1213–1239.
- Gołębiowski, W., R. Michalczyk, M. Dyrek, U. Battista, and K. Wormnes  
2016. Validated simulator for space debris removal with nets and other flexible tethers applications. *Acta Astronautica*, 129:229–240.
- Gołębiowski, W., M. Dyrek, U. Battista, and K. Wormnes  
2015a. Validation of flexible bodies dynamics simulator in parabolic flight. In *66th International Astronautical Congress, Jerusalem, Israel*.

- Gołębiowski, W., R. Michalczyk, M. Dyrek, U. Battista, and K. Wormnes  
2015b. Validated simulator for space debris removal with nets and other flexible tethers applications. In *66th International Astronautical Congress, Jerusalem, Israel*.
- Gregory, D. and J. Mergen  
2014. Space debris removal using upper atmosphere and vortex generator. US Patent 8,657,235.
- Hirzinger, G., K. Landzettel, B. Brunner, M. Fischer, C. Preusche, D. Reintsema, A. Albuschäffer, G. Schreiber, and B. Steinmetz  
2004. DLR's robotics technologies for on-orbit servicing. *Advanced Robotics*, 18(2):139–174.
- Huang, P., J. Cai, Z. Meng, Z. Hu, and D. Wang  
2013. Novel method of monocular real-time feature point tracking for tethered space robots. *Journal of Aerospace Engineering*, 27(6):1–14.
- Huang, P., Z. Hu, and Z. Meng  
2015a. Coupling dynamics modelling and optimal coordinated control of tethered space robot. *Aerospace Science and Technology*, 41:36–46.
- Huang, P., Z. Hu, and F. Zhang  
2016a. Dynamic modelling and coordinated controller designing for the manoeuvrable tether-net space robot system. *Multibody System Dynamics*, 36(2):115–141.
- Huang, P., D. Wang, Z. Meng, and Z. Liu  
2014. Post-capture attitude control for a tethered space robot–target combination system. *Robotica*, 33(4):898–919.
- Huang, P., D. Wang, Z. Meng, F. Zhang, and J. Guo  
2015b. Adaptive postcapture backstepping control for tumbling tethered space robot target combination. *Journal of Guidance, Control, and Dynamics*, 0:1–7.
- Huang, P., M. Wang, Z. Meng, F. Zhang, and Z. Liu  
2016b. Attitude takeover control for post-capture of target spacecraft using space robot. *Aerospace Science and Technology*, 51:171–180.
- Hunt, K. and F. Crossley  
1975. Coefficient of restitution interpreted as damping in vibroimpact. *Journal of applied mechanics*, 42(2):440–445.
- Jiang, H., E. Hawkes, V. Arutyunov, J. Tims, C. Fuller, J. King, C. Seubert, H. Chang, A. Parness, and M. Cutkosky  
2015. Scaling controllable adhesives to grapple floating objects in space. In *Robotics and Automation (ICRA), 2015 IEEE International Conference on*, Pp. 2828–2835. IEEE.
- Jiménez, P., F. Thomas, and C. Torras  
2001. 3D collision detection: a survey. *Computers & Graphics*, 25(2):269–285.

- Johnson, K.  
1987. *Contact mechanics*. Cambridge university press.
- Kasai, T., M. Oda, and T. Suzuki  
1999. Results of the ETS-7 mission-rendezvous docking and space robotics experiments. In *Artificial Intelligence, Robotics and Automation in Space*, volume 440, P. 299.
- Kauderer, A.  
2008. NASA—Canadarm2 and the mobile servicing system. *Internet: <http://www.nasa.gov/mission/pages/station/structure/elements/mss.html>*.
- Kaushik, G., M. Sharma, and K. Yadav  
2014. Space debris elimination techniques. *International Journal of Research*, 1(10):784–787.
- Kessler, D. and B. Cour-Palais  
1978. Collision frequency of artificial satellites: The creation of a debris belt. *Journal of Geophysical Research: Space Physics (1978–2012)*, 83(A6):2637–2646.
- Kitamura, S., Y. Hayakawa, and S. Kawamoto  
2014. A reorbiter for large geo debris objects using ion beam irradiation. *Acta Astronautica*, 94(2):725–735.
- Kofford, A.  
2011. System and method for creating an artificial atmosphere for the removal of space debris. US Patent App. 13/250,409.
- Koh, C. and Y. Rong  
2004. Dynamic analysis of large displacement cable motion with experimental verification. *Journal of Sound and Vibration*, 272(1):187–206.
- Kruijff, M.  
2011. Tethers in space: A propellantless propulsion in-orbit demonstration.
- Landzettel, K., B. Brunner, and G. Hirzinger  
1994. The telerobotic concepts for ESS. In *IARP Workshop on Space Robotics, Montreal, Canada*.
- Lavagna, M., R. Armellini, A. Bombelli, and R. Benvenuto  
2012. Debris removal mechanism based on tethered nets. In *Proceedings of the i-SAIRAS, Turin, Italy*.
- Liou, J. C.  
2011. An active debris removal parametric study for leo environment remediation. *Advances in Space Research*, 47(11):1865–1876.
- Liou, J. C. and N. Johnson  
2009. A sensitivity study of the effectiveness of active debris removal in LEO. *Acta Astronautica*, 64(2):236–243.

- Liou, J. C., N. Johnson, and N. Hill  
2010. Controlling the growth of future leo debris populations with active debris removal. *Acta Astronautica*, 66(5):648–653.
- Liu, L., J. Shan, Y. Ren, and Z. Zhou  
2014. Deployment dynamics of throw-net for active debris removal. In *65th International Astronautical Congress, Toronto, Canada*.
- Lorenzo, A., R. Stefanescu, R. Benvenuto, M. Marcon, and M. Lavagna  
2015. Validation results of satellite mock-up capturing experiment using nets. In *66th International Astronautical Congress, Jerusalem, Israel*.
- Lücking, C., C. Colombo, and C. McInnes  
2011. A passive de-orbiting strategy for high altitude cubesat missions using a deployable reflective balloon. In *8th IAA Symposium on Small Satellites, Berlin, Germany*.
- Mankala, K. and S. Agrawal  
2005. Dynamic modeling and simulation of satellite tethered systems. *Journal of Vibration and Acoustics*, 127(2):144–156.
- McMahan, W., V. Chitrakaran, M. Csencsits, D. Dawson, I. Walker, B. Jones, M. Pritts, D. Dienno, M. Grissom, and C. Rahn  
2006. Field trials and testing of the OctArm continuum manipulator. In *Robotics and Automation, ICRA. Proceedings 2006 IEEE International Conference on, Orlando, FL, USA*, Pp. 2336–2341. IEEE.
- Merino, M., E. Ahedo, C. Bombardelli, H. Urrutxua, and J. Peláez  
2013. Ion beam shepherd satellite for space debris removal. *Progress in Propulsion Physics*, 4:789–802.
- Merino, M., E. Ahedo, C. Bombardelli, H. Urrutxua, J. Pelaez, and L. Summerer  
2011. Space debris removal with an ion beam shepherd satellite: target-plasma interaction. *AIAA Paper*, (2011-6142).
- Mirtich, B.  
1996. *Impulse-based dynamic simulation of rigid body systems*. PhD thesis, University of California at Berkeley.
- Mirtich, B. and J. Canny  
1995. Impulse-based simulation of rigid bodies. In *Proceedings of the 1995 symposium on Interactive 3D graphics*, Pp. 181–188. ACM.
- Missel, J. and D. Mortari  
2011. Sling satellite for debris removal with aggie sweeper. *Advances in the Astronautical Sciences*, 140(1):60–64.
- Missel, J. and D. Mortari  
2013. Removing space debris through sequential captures and ejections. *Journal of Guidance, Control, and Dynamics*, 36(3):743–752.

- Miura, K.  
1985. Method of packaging and deployment of large membranes in space. *The Institute of Space and Astronautical Science report*, 618:1–9.
- Montenbruck, O. and E. Gill  
2012. *Satellite orbits: models, methods and applications*. Springer Science & Business Media.
- NASA  
1995. Guidelines and assessment procedures for limiting orbital debris. *NASA Safety Standard*, 1740:14.
- NASA Orbital Debris Program Office, N.  
April 2016. Orbital debris quarterly news. *National Aeronautics and Space Administration*, 20(1):1–13.
- NASA Orbital Debris Program Office, N.  
February 2017. Orbital debris quarterly news. *National Aeronautics and Space Administration*, 21(1):1–14.
- Nishida, S. and S. Kawamoto  
2011. Strategy for capturing of a tumbling space debris. *Acta Astronautica*, 68(1):113–120.
- Nishida, S., S. Kawamoto, Y. Okawa, F. Terui, and S. Kitamura  
2009. Space debris removal system using a small satellite. *Acta Astronautica*, 65(1):95–102.
- Nock, K., K. Gates, K. Aaron, and A. McRonald  
2010. Gossamer orbit lowering device (GOLD) for safe and efficient de-orbit. *AIAA Paper*, (2010-7824).
- Okada, N.  
2014. Active debris removal using carrier + multiple deorbiting kits. In *3rd European Workshop on Active Debris Removal, Paris, France*.
- Phipps, C.  
2014. A laser-optical system to re-enter or lower low earth orbit space debris. *Acta Astronautica*, 93:418–429.
- Phipps, C., G. Albrecht, H. Friedman, D. Gavel, E. George, J. Murray, C. Ho, W. Priedhorsky, M. Michaelis, and J. Reilly  
1996. ORION: Clearing near-earth space debris using a 20-kw, 530-nm, earth-based, repetitively pulsed laser. *Laser and Particle Beams*, 14(01):1–44.
- Reed, J., J. Busquets, and C. White  
2012. Grappling system for capturing heavy space debris. In *2nd European Workshop on Active Debris Removal, Paris, France*.

- Reintsema, D., J. Thaeter, A. Rathke, W. Naumann, P. Rank, and J. Sommer  
2010. DEOS—the german robotics approach to secure and de-orbit malfunctioned satellites from low earth orbits. In *Proceedings of the i-SAIRAS, Sapporo, Japan*.
- Retat, I. and B. Bischof  
2012. Net capture system: a potential orbital space debris removal system. In *2nd European Workshop on Active Debris Removal, CNES Headquarters, Paris, France*.
- Robin, B., I. Luisa, E. Stephane, and O. Michael  
2015. The e.Deorbit mission: Results of ESA's phase a studies for an active debris removal mission. In *66th International Astronautical Congress, Jerusalem, Israel*.
- Shabana, A. A.  
1997. Flexible multibody dynamics: review of past and recent developments. *Multibody system dynamics*, 1(2):189–222.
- Shan, M., J. Guo, and E. Gill  
2016. Review and comparison of active space debris capturing and removal methods. *Progress in Aerospace Sciences*, 80:18–32.
- Sharf, I., B. Thomsen, E. Botta, and A. Misra  
2017. Experiments and simulation of a net closing mechanism for tether-net capture of space debris. *Acta Astronautica*, 139:332–343.
- Sidorenko, V. and A. Celletti  
2010. A “spring–mass” model of tethered satellite systems: properties of planar periodic motions. *Celestial Mechanics and Dynamical Astronomy*, 107(1-2):209–231.
- Sorge, M.  
2015. Understanding space debris: Causes, mitigations, and issues. *Crosslink*, 16(1):46–51.
- Subbarao, K. and S. Welsh  
2008. Nonlinear control of motion synchronization for satellite proximity operations. *Journal of Guidance, Control, and Dynamics*, 31(5):1284–1294.
- Tibert, G. and M. Gardsback  
2006. Space webs final report. *ESA, Advanced Concepts Team, Rept, 5*.
- Tragesser, S. and H. San  
2003. Orbital maneuvering with electrodynamic tethers. *Journal of Guidance, Control, and Dynamics*, 26(5):805–810.
- Tsuda, Y., O. Mori, R. Funase, H. Sawada, T. Yamamoto, T. Saiki, T. Endo, and J. Kawaguchi  
2011. Flight status of IKAROS deep space solar sail demonstrator. *Acta Astronautica*, 69(9):833–840.
- Van der Pas, N., J. Lousada, C. Terhes, M. Bernabeu, and W. Bauer  
2014. Target selection and comparison of mission design for space debris removal by DLR's advanced study group. *Acta Astronautica*, 102:241–248.

- Wang, D., P. Huang, and J. Cai  
2014a. Detumbling a tethered space robot-target combination using optimal control. In *Information Science and Technology (ICIST), 2014 4th IEEE International Conference on, Shenzhen, China*, Pp. 453–456. IEEE.
- Wang, D., P. Huang, J. Cai, and Z. Meng  
2014b. Coordinated control of tethered space robot using mobile tether attachment point in approaching phase. *Advances in Space Research*, 54(6):1077–1091.
- Wang, D., P. Huang, and Z. Meng  
2015. Coordinated stabilization of tumbling targets using tethered space manipulators. *Aerospace and Electronic Systems, IEEE Transactions on*, 51(3):2420–2432.
- Wang, Y. and M. Mason  
1992. Two-dimensional rigid-body collisions with friction. *Journal of Applied Mechanics*, 59(3):635–642.
- Website  
2017a. Satcat boxscore. <http://www.celestrak.com/satcat/boxscore.asp>. Accessed: 2017-09-23.
- Website  
2017b. Space debris themes in ESA. [http://www.esa.int/Our\\_Activities/Operations/Space\\_Debris](http://www.esa.int/Our_Activities/Operations/Space_Debris). Accessed: 2017-09-23.
- Website  
2017c. Space debris. Wayana Software. Web. <http://www.geosats.com/spacedebris.html>. Accessed: 2017-09-19.
- Whelan, D., E. Adler, S. Wilson III, and G. Roesler Jr  
2000. Darpa orbital express program: effecting a revolution in space-based systems. In *International Symposium on Optical Science and Technology, San Diego, CA, USA*, Pp. 48–56.
- Wiedemann, C., M. Flegel, and M. Mockel  
2012. Active space debris removal. In *Deutscher Luft- und RaumfahrtKongress, Berlin, Germany*.
- Williams, P.  
2005. Optimal orbit transfer with electrodynamic tether. *Journal of Guidance, Control, and Dynamics*, 28(2):369–372.
- Wormnes, K., R. Le Letty, L. Summerer, R. Schonenborg, O. Dubois-Matra, E. Luraschi, A. Cropp, H. Krag, and J. Delaval  
2013. ESA technologies for space debris remediation. In *Proceedings of the 6th IAASS Conference: Safety is Not an Option, Montreal, Canada.*, Pp. 3–4.
- Wright, R.  
2013. Orbital debris mitigation system and method. US Patent 8,567,725.

- Yang, L., Q. Zhang, M. Zhen, and H. Liu  
2017. *Dynamics and Design of Space Nets for Orbital Capture*. Springer.
- Yoshida, K.  
2009. Achievements in space robotics. *Robotics & Automation Magazine, IEEE*, 16(4):20–28.
- Yoshida, K., R. Kurazume, and Y. Umetani  
1991. Dual arm coordination in space free-flying robot. In *Robotics and Automation. IEEE International Conference on, Sacramento, CA, USA*, Pp. 2516–2521. IEEE.
- Yoshida, K. and H. Nakanishi  
2001. The tako (target collaborativize) flyer: a new concept for future satellite servicing. In *i-SAIRAS: Int. Symposium on Artificial Intelligence, Robotics and Automation in Space, Montreal, Canada*, Pp. 18–22.
- Yoshida, K. and H. Nakanishi  
2003. Impedance matching in capturing a satellite by a space robot. In *Intelligent Robots and Systems(IROS 2003). Proceedings. IEEE/RSJ International Conference on, Las Vegas, NV, USA*, volume 4, Pp. 3059–3064. IEEE.
- Yoshida, K., H. Nakanishi, H. Ueno, N. Inaba, T. Nishimaki, and M. Oda  
2004. Dynamics, control and impedance matching for robotic capture of a non-cooperative satellite. *Advanced Robotics*, 18(2):175–198.
- Yu, Y., H. Baoyin, and J. Li  
2010. Modeling and simulation of projecting deployment dynamics of space webs. *Journal of Astronautics*, 5:1–8.
- Zebenay, M.  
2014. *Development of a Robotics-based Satellites Docking Simulator*. PhD thesis, TU Delft, Delft University of Technology.
- Zebenay, M., R. Lampariello, T. Boge, and D. Choukroun  
2012. A new contact dynamics model tool for hardware-in-the-loop docking simulation. In *International Symposium on Artificial Intelligence, Robotics and Automation in Space, Turin, Italy*.
- Zinner, N., A. Williamson, K. Brenner, J. Curran, A. Isaak, M. Knoch, A. Lepppek, and J. Lestishen  
2001. Junk hunter: Autonomous rendezvous, capture, and de-orbit of orbital debris. In *Proceedings of AIAA SPACE 2011 Conference & Exposition*.



# ACKNOWLEDGEMENTS

Time has wings, and it flies so fast. My four years in the Netherlands is like a dream. When I woke up and started recalling what I have dreamt, some memories already become blurred. However, the moments I shared with you are always clear and unforgettable. I would like to take this opportunity to express so many appreciations to those who have supported me.

First of all, I would love to express my greatest appreciation to my promoter, Prof. Eberhard Gill. Thank you very much for providing this opportunity to me to study in your group at TUDelft. I am so grateful to every discussion we had at our regular progress meetings, where you can always guide me, inspire me, and encourage me. Your confidence, erudition and the way of working influenced me not only in these four years, but will also in the rest of my life. My special thanks extend to my daily supervisor Dr. Jian Guo for his patience, his support and his guidance. New ideas can always come out of my mind during discussions with him which make my work more efficient.

Secondly, I wish to thank all my colleagues in the SSE group not only for helping me on my research topic, but also for bringing joy and color to my life. Many thanks are given to my office mates, Xiaoxiang, Adolfo and Johan for the “Fun office” we created. Travelling together with you guys in Madrid is the most unforgettable experience I have ever had. Thanks, Dadui and Marsil, for always backing me up in my life, telling me Brazilian jokes and inviting me to your homes for lunch, dinner, barbecue and PS games. Of course, Fernanda and Carina are also appreciated. Many thanks also go to Dennis for translating my summary and propositions in this thesis from English to Dutch.

I would also like to thank all the other PhD colleagues, Prem, Zixuan, Linyu, Fiona, Mario, Victor, Haiyang, Xinyuan, Yuxin, for all the happy moments we had during the after-lunch walking, the football match, the bowling game, the ice skating and so many other activities. Thank all the staff members at SSE group, Gang, Xianghao, Barry, Angelo, Hans, Samiksha, Chris, Alessandra, Trevor, Jasper, Vidhya, Stefano, Mehmet, Silvana, Robert, for all the laughter we shared in the space bar and many other bars at Delft city center. A huge ‘thank you’ goes to our two beautiful secretaries, Debby and Marielle, who are always patient and friendly when I ask them any administrative question.

Next, I would like to express my gratitude to my best friends in Delft, who are also my flat mates in Delft, Xu, Zheng and Cui. Travelling with you can always bring me surprise and happiness. Great moments living with you will last forever in my mind. I am also grateful to all the HITers (Previous colleagues or classmates at Harbin Institute of Technology) at TUDelft, Shuai, Hai, Fanyu, Bo, Zhenji and Fan for every party and good time we had here. Many thanks are also given to all my basketball fellows for bringing me fun on the court. To my dear friends in the Netherlands, Xiaoli, Xiaoqin, Wanrou, Yongzhe, Di, Wenli, Yanan and Yun for making my life here more lively and lovely.

Last but not least, I wish to express the love from the bottom of my heart to my parents Fuhua Zhang, and Yongcheng Shan, my two elder sisters, Mingming Shan and

Mingduo Shan, and to my girlfriend Lingling Shi. Thank you so much for your support, understanding and unconditional love. Love you for all my life!

Minghe Shan  
16-4-2018

# CURRICULUM VITÆ

## Minghe SHAN

30-11-1989 Born in Meihekou, Jilin Province, China.

### EDUCATION

2007–2011 Undergraduate in Aerospace Manufacturing Engineering  
Harbin Institute of Technology  
Harbin, China

2011–2013 Graduate in Aerospace Manufacturing Engineering  
Harbin Institute of Technology  
Harbin, China

2013–2018 Ph.D. Aerospace Engineering  
Delft University of Technology  
*Thesis:* Net Deployment and Contact Dynamics of Capturing Space Debris Objects  
*Promotor:* Prof. Dr. E. K. A. Gill  
*Copromotor:* Dr. J. Guo



# LIST OF PUBLICATIONS

## JOURNAL PAPERS

1. **Minghe Shan**, Jian Guo, Eberhard Gill. *Contact Dynamics on Net Capturing of Tumbling Space Debris*, Journal of Guidance, Control and Dynamics (2017) (Accepted).
2. **Minghe Shan**, Jian Guo, Eberhard Gill. *Contact Dynamic Models of Space Debris Capturing Using A Net*, *Acta Astronautica* (In press) (2017).
3. **Minghe Shan**, Jian Guo, Eberhard Gill, W. Golebiowski. *Validation of Space Net Deployment Modeling Methods Using Parabolic Flight Experiment*, *Journal of Guidance, Control and Dynamics* **40**, 3319-3327 (2017).
4. **Minghe Shan**, Jian Guo, Eberhard Gill. *Deployment dynamics of tethered-net for space debris removal*, *Acta Astronautica* **132**, 293-302 (2017).
5. **Minghe Shan**, Jian Guo, Eberhard Gill. *Review and Comparison of Active Space Debris Capturing and Removal Methods*, *Progress in Aerospace Sciences* **80**, 18-32 (2016).

## CONFERENCE PAPERS

1. **Minghe Shan**, Jian Guo, Eberhard Gill. *Contact Dynamics of Net Capturing of Space Debris*, the 68th International Astronautical Congress, Adelaide, Australia. IAC-15-A6.5.6, (2017).
2. **Minghe Shan**, Jian Guo, Eberhard Gill. *Contact Dynamic Models of Space Debris Capturing Using A Net*, 7th European Conference for Aeronautics and Aerospace Sciences (EUCASS), Milan, Italy. 612, (2017).
3. **Minghe Shan**, Jian Guo, Eberhard Gill. *Tumbling Space Debris Capturing Using a Net*, 7th European Conference on Space Debris, Darmstadt, Germany (2017).
4. **Minghe Shan**, Jian Guo, Eberhard Gill. *An Analysis of Critical Deployment Parameters for Tethered-net Capturing for Space Debris Removal*, the 66th International Astronautical Congress, Jerusalem, Israel. IAC-15-A6.5.7, (2015).
5. **Minghe Shan**, Jian Guo, Eberhard Gill. *Analysis of the Concept of Non-Cooperative Targets and Associated Tailored Active Debris Removal Methods*, the 65th International Astronautical Congress. Toronto, Canada. IAC-14-A6.5.10, (2014).